STRUCTURAL AND ELECTRONIC COUPLING IN NANOSCALE MATERIALS

by

Benjamin W. McDowell

A dissertation accepted and approved in partial fulfillment of the

requirements for the degree of

Doctor of Philosophy

in Chemistry

Dissertation Committee:

Christopher Hendon, Chair

George Nazin, Advisor

Mark Lonergan, Core Member

Benjamín Alemán, Institutional Representative

University of Oregon

Winter 2024

DISSERTATION ABSTRACT

Benjamin W. McDowell

Doctor of Philosophy in Chemistry

Title: STRUCTURAL AND ELECTRONIC COUPLING IN NANOSCALE MATERIALS

As modern electronic devices continue to shrink in size, the limitations of Si as a transistor material become increasingly imminent. To overcome these limitations, it is necessary to explore alternative materials that can be used in electronic devices that surpass the miniaturization limit of Si-based devices. In this effort, it is important to develop an understanding of how materials behave when they are reduced in size and scale down to ultra-thin structures. Here, we explore how ultra-thin dielectric materials behave differently than their bulk counterparts, experiencing chemical interactions at interfaces that can result in unexpected structures and electronic properties. By using a combination of scanning tunneling microsocopy/spectroscopy and density functional theory, we study several manifestations of distinct structural and electronic properties arising in ultra-thin materials. We extend this physical picture to understand how the properties of these films affect adsorbed nanostructures, analogous to interactions occurring in a transistor setting.

TABLE OF CONTENTS

Chapter **Page**

LIST OF FIGURES

Figure **Page**

LIST OF TABLES

Table **Page**

CHAPTER I

INTRODUCTION

1.1. Background

As modern electronic devices continue to shrink, the limitations of Si as a transistor material become increasingly imminent.[1-5] In order to overcome these limitations, it is necessary to explore alternative transistor materials which can be scaled down beyond the doping limit of Si. In this effort it is necessary to both identify materials that may serve as suitable replacements for Si in nanoscale electronic devices as well as building a better collective understanding of how materials behave at the nanoscale and atomically-thin limit. Here, we mostly focus on making progress to the latter objective, while allowing the former objective to motivate particular systems of interest.

In developing an understanding of the behavior of materials at the nanoscale, it is critical to distinguish behavior in nanoscale systems from those of their bulk counterparts. When materials are reduced from bulk systems to the atomically-thin limit, they often exhibit drastically different properties.[6-9] In part, this is due to an increased significance of surfaces and interfaces in nanoscale systems, which, while also present in bulk systems, comprise a statistically insignificant portion of the structure. At surfaces, the chemistry of materials is inherently different due the coordinating environment being distinct from that of the bulk material, and can result in dangling bonds[10-12] and re-hybridization.[13-16] This in turn results in the electronic structure of surfaces being distinctly different from bulk materials, making it difficult to realize certain electronic properties in nanoscale materials, such as a wide band gap,[5] which poses problems for further miniaturization of electronic devices.[17, 18] Similar effects are also

present at interfaces, which experience a similar disruption of symmetry relative to the bulk material. However a significant distinction between surfaces and interfaces lies in the complexity of interactions at each; interfaces experience the same disruption of bulk symmetry present at surfaces, but also are affected by the chemical nature of the two surfaces composing the interface.

This distinction emphasizes the important role of coupling in nanoscale systems. At interfaces, interactions depend both on the chemical identity of atomic species at the interface and also the alignment of the two phases, which can lead to a multitude of possible electronic properties. The alignment of the two phases at the interface often leads to moiré patterns, where the registry between crystal lattices at the interface can lead to spatial modulation of the atomic and electronic structure. Moiré patterns can influence local electronic properties, leading to spatial modulation of the work function,[19] 2D electronic states,[20-25] and substrate-adlayer charge transfer interactions.[26, 27] In order to characterize these systems, it is necessary to probe the local electronic structure of nanoscale systems, making scanning tunneling microscopy/spectroscopy (STM/STS) a useful tool in this effort due to its ability to image electronic structure in real-space with atomic-scale resolution.[28]

In this work, we use STM/STS and computational methods to study the interactions that occur at interfaces in nanoscale systems. We refer to the cumulative effect of these interactions as coupling, of which we explore several specific types. Broadly, the effects of these interactions can be categorized as structural and electronic. In the case of structural coupling, we show that strong substrate-adlayer interactions can result in structural coupling between the two, where the symmetry of the substrate serves as a template for crystal growth of the adlayer structure. Here, we use electronic coupling as a general term to describe modulation of electronic properties in

nanoscale structures, of which we observe several different varieties: spatial modulation of electronic properties, formation of a 2D electrostatic potential, and localization of electronic states in an adsorbate. In general, this work offers important insight on the role of interlayer interactions in determining the atomic structure and electronic properties of nanoscale materials.

1.2. Overview of Dissertation

Chapter I begins with a discussion of the motivation and background, which highlights the significance of presented results and builds the scope of academic interest within which the results fall.

Chapter II contains an overview of the methodology used and developed to conduct the experiments reported in later chapters. This includes descriptions of the instrumentation and theory of STM/STS, as well as computational methods for simulating STM/STS results.

In Chapter III, we use STM to observe a system that exhibits structural coupling between a Ag(111) substrate and a single-layer adlayer of RbI. This structural coupling is manifested by our observation of a previously unreported alkali halide structure which, rather than growing in the rock-salt-like structure expected for other alkali halides, adopts a hexagonal structure matching the symmetry of the Ag(111) surface. Using DFT, we directly compare the substrate-adlayer interactions between this unusual hexagonal RbI structure and a rock-salt-like RbI structure analogous to that observed for other alkali halides. This systems serves as a model system with which to explore the role of substrate-adlayer interactions in inducing structural coupling between ultra-thin films and the surface they are grown on. Chapter III has previously been published under the title “Structural Bistability in RbI Monolayers on Ag(111)” in the

Journal of Physical Chemistry Letters, co-authored by Benjamin W. McDowell, Jon M. Mills, Motoaki Honda, and George V. Nazin.

In Chapter IV, we move on to exploring the role of coupling in dictating the electronic properties of ultra-thin films, where we use a Ag(111) substrate and single-layer RbI as a model system. Using STM/STS in combination with numerical simulation, we show that substrate-adlayer coupling has significant implications for the electronic properties of single-layer RbI. Furthermore, this coupling is responsible for local, spatially-dependent variations in electronic properties, which we measure with STS and corroborate with DFT calculations. Chapter IV has previously been accepted for publication under the title "Probing the Electronic Structure of Bi-Stable Single-Layer RbI Structures on Ag(111)" in Physical Review B: Condensed Matter and Material Physics, co-authored by Benjamin W. McDowell, Jon M. Mills, Austin W. Green, Motoaki Honda, and George V. Nazin.

In Chapter V, we extend the discussion of electronic coupling to examine a spatially-dependent electrostatic potential localized to the substrate-adlayer interface. This potential induces spatial modulation of an interface electronic state, which we characterize with STM/STS. We model this spatial modulation using the Mathieu differential equation, which qualitatively reproduces our experimental results and offers insight on the physical origin of observed electronic features. Anisotropy in the 2D electrostatic potential has important implications for the electronic structure, resulting in an anisotropic band gap and effective electron mass. Chapter V has previously been published under the title "Spatially-Modulated Interface States in a Two-Dimensional Potential: Single-layer RbI on Ag(111)" in the Journal of Chemical Physics, co-authored by Benjamin W. McDowell, Jon M. Mills, Motoaki Honda, and George V. Nazin.

In Chapter VI, we discuss how coupling between a substrate-adlayer system extends to adsorbed SWCNTs. We show, using STM/STS, that SWCNT electronic structure is affected both by coupling to an Au(111) surface and to single-layer RbI. In both cases, the SWCNT electronic structure exhibits band-bending, which is supported by DFT and a simple electrostatic model of perturbation by an external dipole charge pair. Chapter VI has previously been published under the title "Impact of External Electronic Perturbations on Single-Walled Carbon Nanotube Electronic Structure: Scanning Tunneling Spectroscopy and Density Functional Theory" in the Journal of Physical Chemistry C, co-authored by Benjamen N. Taber, Benjamin W. McDowell, Jon M. Mills, Christian F. Gervasi, and George V. Nazin.

In Chapter VII, we build on the notion that single-layer RbI perturbs SWCNTs by examining local variations in SWCNT electronic structure. Using STM/STS, we observe that grain boundary defects (GBDs) in single-layer RbI yield electrostatic potentials at the defect, which localize electronic states in the SWCNT. Using DFT, we show that the electrostatic potential at GBDs is the result of substrate-adlayer coupling that is stronger than for the case of the pristine RbI monolayer, and is expected to be a common phenomenon for any GBD in single-layer RbI. The presented physical picture offers insight on potential mechanisms for localized SWCNT electronic structure, which could account for the underperformance of SWCNT-based devices reported elsewhere. Chapter VII has previously been published under the title "Modulation of Carbon Nanotube Electronic Structure by Grain Boundary Defects in RbI on Au(111)" in the Journal of Physical Chemistry Letters, co-authored by Benjamin W. McDowell, Benjamen N. Taber, Jon M. Mills, Christian F. Gervasi, Motoaki Honda, and George V. Nazin.

All references, grouped by the chapter in which they appear, can be found at the end of this dissertation.

CHAPTER II

METHODS

2.1. Instrumentation

To ensure quality STM/STS measurements, it is necessary to conduct experiments under cryogenic, UHV conditions. The specific details of the instrument used in this work have been described in detail elsewhere,[1] and will be summarized here. The STM operates in a custom-built vacuum chamber that is pumped on by an ion pump and a magnetically-levitating turbo pump, and has a base pressure of around 3×10^{-11} torr during experiments. During STM operation, the sample is cooled to a temperature of around 26-36 K, by use of a closed-cycle He cryostat (CCC). The CCC is mounted to a steel structure that is vibrationally isolated from the rest of the STM, which is mounted on a leveled optics table. Isolation of the STM from vibrations is critical to proper function, and is achieved through two major components: the He compressor is attached to the vacuum chamber by means of rubber bellows, which are positively pressurized with approximately 0.5-1.0 psig of He, and the STM body is suspended inside the vacuum chamber by 4 springs. The STM body is outfitted with 4 SmCo magnets which, by inducing eddy currents in the gold-plated thermal shields surrounding the STM body, adds a damping force to any vertical motion of the STM body. These steps are critical to ensuring stable, noise-free STM measurements, and the instrument used here has achieved a particularly

A popular choice for the tip metal is Ag, which can be prepared by electrochemical etching, followed by subsequent sputter cycles with Ne ions under UHV conditions.[2] To prepare tips, Ag wire (0.3 mm diameter) is cut to an appropriate length (3-6 mm). The tip is the placed in a metal socket oriented parallel to the ground, which is connected to a power supply. A metal

loop made of W is brought orthogonal to the metal tip, and a peristatic pump is used to flow an acidic solution (composed of 1 part glacial acetic and acid and 9 parts H_2O) across the metal loop, forming a meniscus. The acid solution flowing off the loop is collected in a container underneath the tip, and passed back through the tubing connected to the peristatic pump. The metal tip is also connected to a power supply. By applying a voltage difference between the tip and metal loop (around 10-15 V is typical), current flow is induced from the tip to the loop, resulting in oxidation of the Ag metal tip. The metal loop is also connected to an Arduino controlled stepper-motor, which moves the metal loop back and forth (by around 4 mm maximum oscillation distance) along the axis of the tip orientation. In doing so, the end of the tip (closest to the loop) spends longest in the meniscus, with the time spent in the meniscus decreasing somewhat linearly with distance from the end of the tip. This difference in time spent in the meniscus results in most of the Ag oxidation occurring at the end of the tip, which effectively sharpens the Ag tip. Progress of the tip-sharpening is monitored in real time using a microscope, situated above the tip/loop setup, and the power supply is turned off when the tip is sufficiently sharp.

Further preparation of the Ag tip is done under UHV conditions. The Ag tip is mounted and oriented so that the etched end is pointed towards an ion gun. The vacuum chamber is backfilled with Ne (to around 5.0×10^{-5} torr) and the ion gun is turned on to bombard the Ag tip with Ne ions for about 10 minutes. During sputtering, the Ag tip is biased to ~80 V, which enhances the electric field at the apex of the tip, resulting in a more nanoscopically-sharpened tip. This process is repeated, usually for at least 5 cycles, with the vacuum chamber filled with fresh Ne for each cycle.

Specific sample preparation methods are described independently for each chapter, but several common procedures are discussed here. Single crystal samples are mounted to custom built Mo sample holders by means of Ta springs, which clamp the sample against the surface, leaving a ~5x3 mm area within which scans can be conducted. To achieve the atomically flat surface requisite for STM measurements, the sample undergoes many cycles of sputtering with Ne ions, followed by annealing. Sputtering cleans the sample by bombarding the surface with noble gas ions, and annealing gives atoms on the surface energy to move into an energetically favorable crystal facet. The annealing temperature depends on the sample and is chosen to give the atoms enough energy to move, but not so much energy so as to instill multiple crystal domains. To deposit atomically-thin layers on the clean single-crystal substrate, a thermal evaporator is used, where a Mo crucible is filled with the salt to be deposited and placed inside a W filament, all of which is contained inside a Ta shield with a rotatable coverslip that modulates deposition. Under UHV conditions, the current is run through the filament, and after the crucible has reached thermal equilibrium, the sample is brought up close to an opening in the Ta shield and the coverslip is rotated to allow sublimated salt to reach the sample surface. Deposition times and currents depend on the chemical identity of the salt, and for RbI typical conditions would be 12.5 A and 1 min.

2.2. Scanning Tunneling Microscopy

The experimental setup for STM consists of an atomically sharp metallic tip brought within a few nanometers of a surface. A voltage bias is applied, typically to the sample, which instills a potential difference between the tip and sample. The tip is manipulated by a piezoelectric motor, which can control motion of the tip in three dimensions with nanoscale

precision. When the tip is brought close to the sample, electrons can tunnel across the vacuum barrier between the tip and sample, leading to a tunneling current, usually on the scale of pico- or nano- amps. The tunneling current is proportional to the distance between the tip and sample, and increases exponentially with smaller distances. An STM image is generated by rasterization, where the tunneling current measurement is performed as a two-dimensional function of space. There are two main ways in which this measurement is performed, which are known as constant-current and constant-height topography.

In constant-current topography, which is used for the work discussed here, a feedback loop controls the piezoelectric motor and manipulates the tip-sample distance to maintain a constant tunneling current. Here, the STM image is a measurement of the distance by which the tip moves to maintain a constant tunneling current at each spatial point. The feedback loop operates on the principle of proportional-integral-derivative feedback, by which the tip sample distance is controlled by a weighted combination of terms which correspond to the magnitude of the tunneling current and the integral of the tunneling current, the exact weighting of which can change with experimental context.

In constant-height topography, the tip sample distance is kept constant and the STM image is a measurement of the tunneling current at each spatial point, where the piezoelectric motor moves the tip only along the plane of the sample. This method is generally less used for several reasons. When the sample is not very flat, scanning in constant-height mode can result in collisions between the tip and sample, which can result in poor/incorrect image quality. Additionally, the tunneling current is inherently uncontrolled in this method, and can get very large if the tip is brought too close to the sample, possible resulting in damage to the sample or tip. Finally, the tip is not necessarily orthogonal to the surface, so it is non-trivial to expect the

tip to scan exactly along the plane of the surface, meaning that there would be some spatially-dependent error in the tip-sample distance. This effect can be corrected in the constant-current method, but is more difficult to deconvolute from STM images acquired in constant-height mode, since the dependence of the tunneling current on the tip-sample distance is not linear.

2.3. Scanning Tunneling Spectroscopy

While it is useful to image surfaces with nanoscale resolution via STM, the most powerful utility of STM/STS lies in its ability to provide insight on electronic structure via STS. STS is sensitive to the local electronic structure, because the tunneling current at a given bias voltage is proportional to the number of states that are accessible to be tunneled through. The accessible states are those which have an energy between Fermi level of the tip and Fermi level of the sample which, assuming that the tip and sample have equivalent Fermi energies in the absence of an applied bias, allows the tunneling current for a given bias voltage to be expressed as:

$$I \propto N(E_f + V_{bias}) - N(E_f)$$

By taking the derivative of the tunneling current with respect to bias, we get the following expression, which is directly proportional to the LDOS of the sample:

$$\frac{dI}{dV_{bias}} \propto \frac{N(E_f + V_{bias})}{dV_{bias}} \propto LDOS_{sample}$$

The significance of this measurement lies in the fact that it is performed over a single point in space, so that the electronic spectra acquired by STS can then be mapped in space along the sample surface. This method is commonly employed to measure how electronic structure varies along some spatial coordinate of the sample, or can be extended to map spatial variations

in electronic structure in two dimensions along the plane of the surface. Effectively, this technique allows specific electronic states to be mapped with atomic-scale spatial resolution.

In typical STS measurements, the feedback loop controlling the tip position is turned off, freezing the tip in place, although it is sometimes useful to leave the feedback loop on when measuring over large voltage ranges.[3, 4] Then, the bias voltage is ramped over a range of biases, using a predefined increment between individual voltage points. At each voltage point, a sinusoidal voltage signal is applied. The tunneling current is passed to a lock-in amplifier, which selectively tunes into the frequency of the applied voltage signal and amplifies the component of the current with a phase corresponding to the derivative of the applied bias. Effectively, this allows a direct measurement of the dI/dV signal, which offers superior precision than could be achieved by numerically differentiating the tunneling current with respect to voltage.

2.4. Simulation of Scanning Tunneling Microscopy Images

The appearance of topography in STM images can at times be difficult to understand, particularly at high bias voltages when the tip is further from the surface and the spatial resolution is reduced. In these cases, it is often constructive to simulate STM images from DFT results, which allows assignment of particular atomic configurations to the STM topography. Traditionally, this is done by examining the charge density of a system, where the STM image can be simulated by taking a two-dimensional slice of the charge density (containing the electrons within the energy range corresponding to the STM bias) in the plane of the surface. This is analogous to the 'constant-height' mode of STM topography, and has been shown to be useful when the STM topography of interest closely resembles the atomic structure. However, at high bias voltages, the STM topography can be more closely dependent on the LDOS of the

sample surface, and in these cases it is insufficient to model the STM image by simply slicing the charge density. Rather, it is important to consider that the tunneling probability through various sample states is dependent on their energy, a detail which is typically absent in the charge density files output by DFT codes.

To model the STM topography of surfaces, we consider the simple case of a square potential (see Figure), which follows the Wentzel-Kramers-Brillouin approximation.[5]

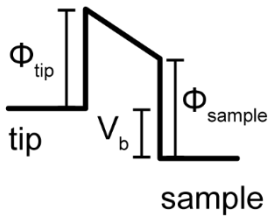

Figure 2.1: Potential energy diagram of an STM/STS measurement, where the sample is biased to lower its Fermi energy relative to that of the tip.

We begin by defining the tunneling current (I) in terms of the probability of electrons tunneling across the tip-sample junction (T), and the number of sample states accessible for tunneling (DOS_{sample}). It is common in STM/STS measurements to assume a constant DOS for the tip, which gives the following expression for the tunneling current:

$$I(E,r) \propto T(E,r) \times DOS_{sample}(E)$$

The tunneling probability can be expanded in terms of an arbitrary potential barrier ($U(r)$), the electron mass (m), and the width of the potential (r_0), as derived by Landau and Lifshitz,[6] and presented by Chen.[5]

$$I(E,r) \propto DOS_{sample}(E) \times exp\left(\frac{2}{\hbar}\int_0^{r_0}[2m(U(r)-E)]^{1/2}\,dr\right)$$

To approximate the potential barrier between the tip and sample, we can choose to represent each as a plane electrode, in which case the potential varies linearly with the electric

field resulting from a bias voltage applied to the sample. This allows us to express the potential in terms of the work function (φ, which for simplicity can be assumed to be identical between the tip and sample) and the bias voltage (V).

$$U(r) = \varphi - E - \frac{Vr}{r_0}$$

By substituting this expression for the potential, we can solve the integral which gives the following expression of the tunneling current:

$$I(E,r) \propto DOS_{sample}(E) \times exp\left(\frac{\sqrt{32m}r_i}{3\hbar V}\left[(\varphi - E - V)^{3/2} - (\varphi - E)^{3/2}\right]\right)$$

To make this expression compatible with DFT calculations, it is useful to reference the energy of tunneling electrons to the Fermi energy of the sample, as in the following:

$$I(E,r) \propto DOS_{sample}(E) \times exp\left(\frac{\sqrt{32m}r_i}{3\hbar V}\left[(\varphi - E + V)^{3/2} - (\varphi - E)^{3/2}\right]\right)$$

Then, to simulate STM images using this expression, the tunneling current is calculated over a grid of spatial points, analogous in concept to the 'constant-height' method of STM image acquisition. At each spatial point, the contributions of each atom on the sample surface are summed by using the distance between the sampling point and the atom position (r_i) to calculate the tunneling probability. The tunneling probability then weights the site projected DOS of each atom in the sample surface, which is then integrated from energies of 0 (ie the Fermi energy) to the bias voltage (V). This gives the following expression:

$$I(E,r) \propto \sum_i \sum_E^V D_i(E) \times exp\left(-\frac{\sqrt{32m}r_i}{3\hbar V}\left[(\varphi - E + V)^{3/2} - (\varphi - E)^{3/2}\right]\right)$$

This code is fully parallelizable, and is hosted on Github. It has been utilized to simulate STM images in several publications.[7-9]

2.5. Simulation of Scanning Tunneling Spectroscopy Data

The above discussion of simulating STM images can be extended to simulate STS results also. To simulate the dI/dV measurement, we can, for a given position in space, simulate the LDOS weighted by the tunneling probability as a function of energy. In this method, the voltage bias is equal to the energy of the tunneling electron, analogously to the method by which STS spectra are acquired experimentally. Using this approach, we can simulate the dI/dV measurement to acquire a single spectra at a given point in space. By simulating dI/dV measurements at many spatial points, we can build progressions of simulated dI/dV data analogously to those frequently used in experiment to map the spatial variations of the LDOS.

CHAPTER III

STRUCTURAL BISTABILITY IN RBI MONOLAYERS ON Ag(111)

From McDowell, B.W.; Mills, J.M.; Honda, M.; and Nazin, G.V.; Structural Bistability in RbI Monolayers on Ag(111). *J. Phys. Chem. Lett.* **2023**, 14, 3023-3030.

3.1. Introduction

At the atomically thin limit, surface reconstruction causes many materials to exhibit exciting electronic properties that are completely different from those found in their bulk counterparts.[1-4] Since surface reconstruction can dramatically affect a material's electronic structure, it can be challenging to realize some electronic properties in atomically thin films, like, for example, a wide band gap.[5] This challenge is consequential in the ability to achieve sufficient electronic isolation using atomically thin insulators, which is essential for further miniaturization of modern electronic circuits.[6, 7] While there are a chemically diverse range of options for atomically thin insulating layers, alkali halides have attracted attention due to their wide band gap[8, 9] and well-defined structure.[10-14] Of the alkali halides, NaCl has been the most extensively characterized as an atomically thin film, and its preference to form rock-salt-like islands has been demonstrated on a variety of substrates using scanning tunneling microscopy/spectroscopy (STM/STS).[10-15] Recently, NaCl was shown to form hexagonal atomically thin structures on the (110) diamond surface,[16] where NaCl-substrate interaction is stronger than in the previous studies where metallic substrates were used. Similarly, in the case of metal oxides, where the cation-anion interaction is weaker than in NaCl, strong adlayer-substrate interactions have been shown to result in structurally diverse atomically thin metal oxide phases.[17-23] However, to our

knowledge, no STM-based study of this kind of structural variability in alkali-halides has been reported in the literature.

3.2. Methods

Experiments were carried out in a home-built ultrahigh vacuum (UHV) cryogenic STM system, in which the bias voltage (V_b) is applied to the sample.[24] All imaging and spectroscopic measurements were carried out at 26 K using electrochemically etched silver tips, at a base pressure of approximately 3.0×10^{-11} torr. A Ag(111) single crystal was prepared in situ by sputtering with Ne followed by annealing, which was repeated for multiple cycles. A sub-monolayer of RbI (obtained from Sigma-Aldrich, 99.9% purity) was deposited onto the Ag surface (held at room temperature) via in situ sublimation under UHV conditions. After deposition of RbI, the sample was annealed for one hour at approximately 320 K. All reported errors correspond to one standard error of the experimental data summed in quadrature with the systematic error that arises from drifting of the tip during measurement.

All computations were performed using DFT[25] as implemented by the Vienna Ab Initio Simulation Package (VASP)[26-28] with a projector-augmented plane wave basis set.[29] The Ag(111) surface was constructed with data obtained from the Materials Project[30] with approximately 25 Å of vacuum added to prevent interaction of periodic unit cells perpendicular to the surface. The hexagonal RbI structure was optimized on three layers of Ag (with the bottom layer frozen to retain the bulk lattice constant) via the PBE functional for solids (PBE_{sol})[31] until all forces were less than 0.005 eV $Å^{-1}$, using a $5 \times 5 \times 1$ k-point mesh centered at the Γ point and a 500 eV planewave cutoff. Using the geometrically optimized structure, the HSE06[32] functional was used to calculate the electronic structure at the Γ point, providing a more robust treatment of

ranged interactions than PBE_{sol}. The unit cell size of the square RbI structure (300 Rb,I atoms + 558 Ag atoms per layer) was prohibitive to performing calculations at the same level of accuracy, and was optimized on a single, frozen layer of Ag via the PBE_{sol} functional at the Γ point with a 500 eV planewave cutoff until all forces were less than 0.05 eV $Å^{-1}$. To allow for direct quantitative comparisons to be made between the two phase types, electronic structure optimizations were also performed via the PBE_{sol} functional for the hexagonal RbI monolayer on a single layer of Ag, using previously discussed parameters. All electronic structure calculations were optimized until the change in energy between iterative steps was less than 10^{-8} eV. To characterize charge transfer between atoms, we used Bader analysis[33-36] with a vacuum cutoff of 10^{-3} electrons $Å^{-3}$, which kept all atomic volumes within 5% of the average for each atomic species. Visualizations of all structures were made using the VESTA package.[37] Binding energies were calculated by subtracting the energies of the isolated surface and adlayer from the energy of the surface/adlayer structure.

To calculate the spatial and energy dependence of individual atomic contributions to the tunneling current, LDOS maps were interpolated using the Wentzel-Kramers-Brillouin[38] approximation. In this approximation (which we have provided a more detailed discussion of in the Appendix), the reduction in tunneling barrier height induced by the bias voltage is used to weight the LDOS of individual atoms as in (1) below, where I is the tunneling current, E is an eigenenergy, r_i is the distance between the tip and an atom on the surface, V is the bias voltage, D_i is the a density of states for an atom on the surface, m is the mass of an electron, $\hbar$ is the reduced Planck's constant, and φ is the work function of the surface calculated by DFT.

$$I(E,r) \propto \sum_i \sum_E^V D_i(E) \times exp\left(-\frac{\sqrt{32m}r_i}{3\hbar V}\left[(\varphi - E + V)^{3/2} - (\varphi - E)^{3/2}\right]\right) \qquad (1)$$

3.3. Results and Discussion

An interesting alternative to NaCl allowing exploration of the substrate-induced structural variability is RbI, where the alkali-halide interaction is weaker than in NaCl.[39] Here, we use RbI deposited on Ag(111) as a model system for investigations of such structural variabilities using STM. Our results show that on Ag(111), RbI forms monolayers with a long-range order persisting over tens of nanometers (Figure 3.1a). We observe two distinct structural phases of RbI, which are distinguished by the coordination of topographic features within the monolayer (Figure 3.1b). In one of the two phases, STM images show features locally coordinated in a "hexagonal planar" fashion (left part of Figure 3.1b), while the other phase shows a "square planar" coordination (right part of Figure 3.1b). The coexistence of such distinct structural phase types is surprising, since only a single phase type (analogous to the "square planar" phase observed here) has been previously reported by STM for other ultra-thin alkali halide structures,[10-14] and for RbI on metallic surfaces.[40]

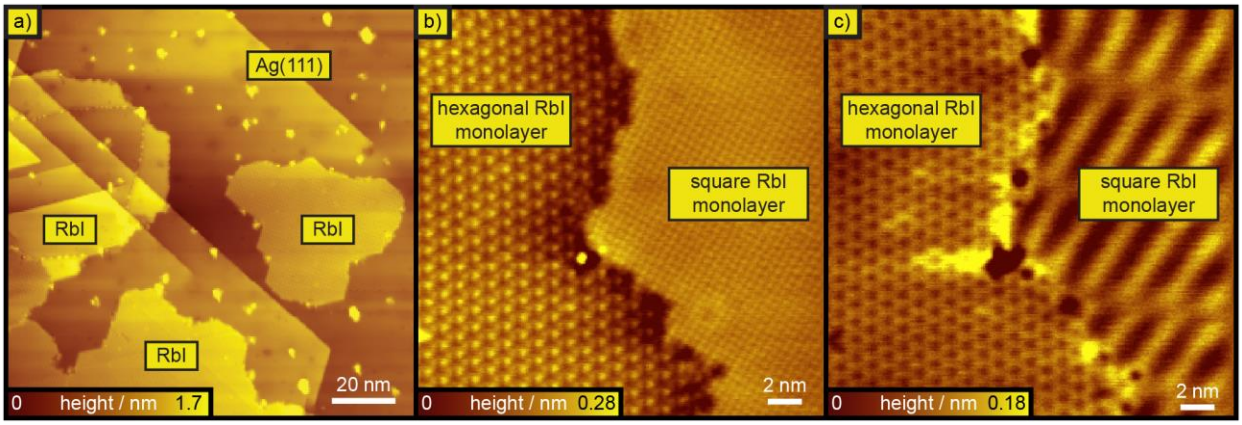

Figure 3.1. a) Large scale STM topography (V_b = 300 mV, I = 10 pA), showing several RbI islands and Ag(111) step edges. The smaller, unlabeled clusters are underdeveloped RbI islands. b,c) Topography of domain boundary between square and hexagonal RbI monolayers (b: V_b = -200 mV, I = -200 pA; c: V_b = 2 V, I = 200 pA).

To understand the origins of the observed bistability of RbI on Ag(111), we first focus on the atomic structure of the "hexagonal planar" phase (hexagonal in the following). STM imaging shows that the hexagonal phase is aligned with the Ag(111) surface. The hexagonal monolayer can be defined by the propagation of two distinct lattice vectors (Figure 3.2a) with orientations that are identical with ⟨110⟩ directions of the Ag(111) surface. Further, the lengths of these two vectors (1.20±0.03 nm and 1.15±0.05 nm, Figure 3.2a) are consistent, within experimental accuracy, with four interatomic distances of Ag, as shown in Figure 3.2b, which defines the orientational and dimensional registry of the hexagonal phase with respect to Ag(111). Thus, the hexagonal RbI structure is commensurate with a 4x4 supercell of the Ag(111) surface, within the experimental uncertainty.

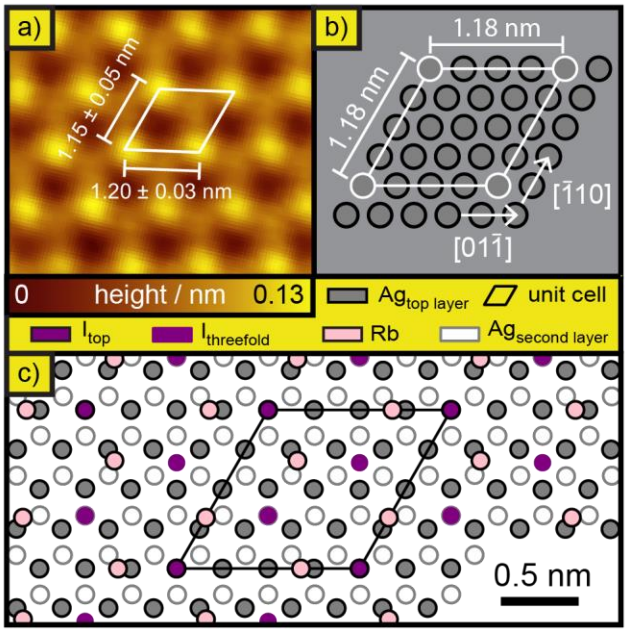

Figure 3.2. a) STM topography (V_b = 100 mV, I = 30 pA) of a hexagonal RbI monolayer. b) Atomic model of the Ag(111) surface, with the periodicity of the hexagonal RbI monolayer overlaid. c) DFT optimized structure of the pristine hexagonal RbI monolayer.

To make further progress in identifying the atomic structure of the hexagonal phase, we performed density functional theory (DFT) calculations. We have calculated a wide variety of test

RbI structures commensurate with the experimentally found supercell, with one of the most common results of these calculations being the fact that the topography maps obtained at voltages close to the Fermi level were always dominated by iodine atomic orbitals (see Appendix, Figure A.1), suggesting that the brightest protrusions in Figures 3.1b and 3.2a correspond to iodine atoms. Our results are in agreement with previous studies of alkali halides, which found that protrusions observed in STM topography at low bias voltages correspond to halide atoms.[10-15] Further, this interpretation is supported by the changes in STM topography observed at high bias voltages, where the contrast is inverted (see discussion below), in line with our DFT results which show that at these voltages the tunneling current is dominated by unoccupied Rb orbitals. However, we found that it was insufficient to only have one iodine atom (and one Rb atom) per unit cell in order to obtain regular RbI structures consistent with those observed in experiment. By addition of individual RbI molecules to the unit cell, we arrive at structures analogous to that of Figure 3.2c, where the Rb-I nearest-neighbor distances are 5.2% longer than those observed in bulk RbI and 9.8% shorter than for RbI molecules in gas phase.

Further, our DFT results (Figure 3.3) illustrate the general expectation that the registry of the RbI layers with respect to the Ag(111) surface should be defined by the interatomic interactions at the RbI-Ag interface involving local charge transfer and polarization. These surface charge redistribution effects originate from the ionic character of the adlayer, which interacts with the highly polarizable metallic surface. Charge transfer occurs not only within the adlayer, but also between the adlayer and the Ag surface, which is evidenced by a downshift of the field emission resonance on RbI relative to the bare Ag(111) surface (see Appendix, Figure A.2).[10] Due to the larger ionic radius of iodine relative to Rb, interaction of iodine with the surface is stronger than that of Rb, leading, in particular, to a greater degree of I-Ag electron rearrangement (as compared

to that of Rb-Ag). This is made clear by comparing the DFT-calculated net electron counts of the RbI/Ag structure to those of an identical RbI structure without Ag: on average, iodine atoms lose 0.236 electrons and Rb atoms gain 0.067 electrons in the presence of Ag, indicating a net transfer of 0.170 electrons (per RbI molecule) from the adlayer to the substrate. This finding can be visually illustrated by plotting the spatial electron density distribution (Figure 3a), which shows that there is more shared charge density between iodine and Ag atoms than between Rb and Ag atoms. Our DFT results indicate that this shared electron density is the result of covalent bonding between the adlayer and substrate (see Appendix, Figure A..3), which is manifested by an increased local density of states (LDOS) near the Fermi level, in line with previous results for other alkali halides.[13,14] Furthermore, the intensity of the LDOS near the Fermi level is more sensitive to the placement of iodine, rather than Rb. This indicates that interactions due to charge redistribution effects are strongest between iodine and the surface, and suggests that the coordination of iodines is most significant in determining the energetics of the RbI monolayer.

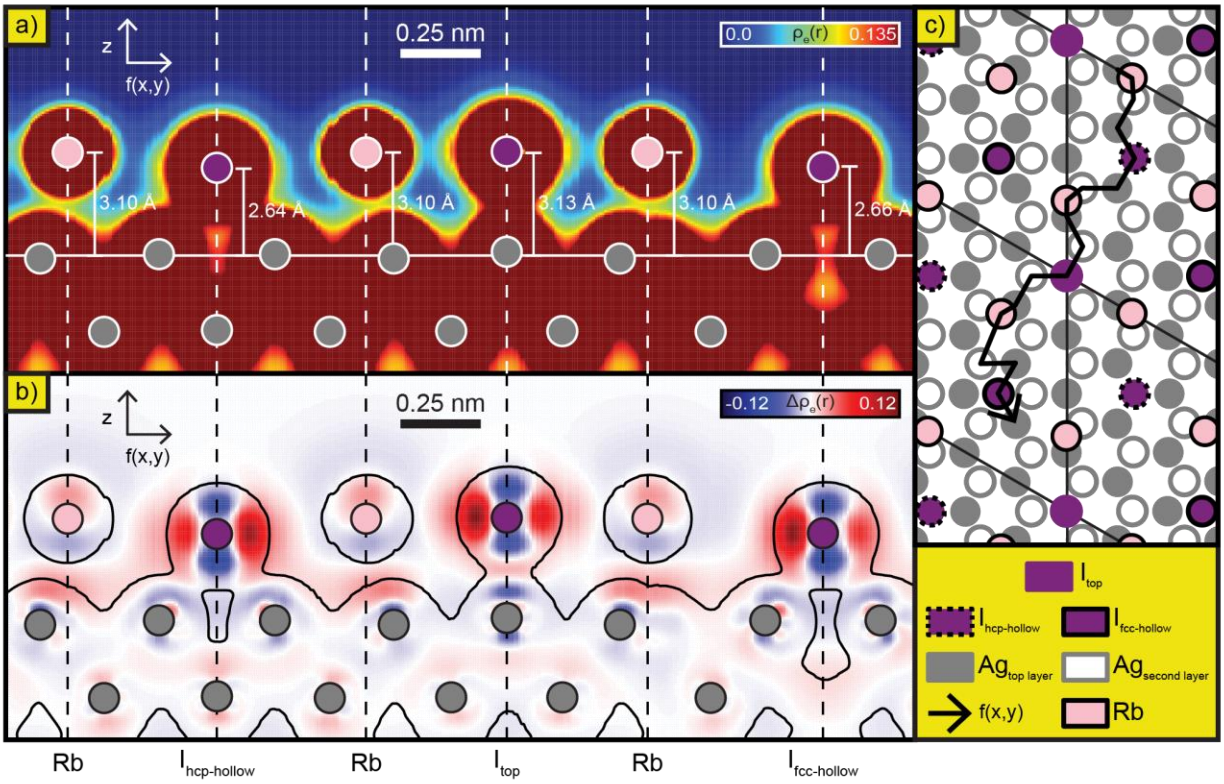

Figure 3.3. DFT calculations of the chemical interaction between a hexagonal RbI monolayer and the Ag(111) surface. a) Total electron density sliced along the path shown in (c). The horizontal white line shows the average height of the top layer of Ag, from which the individual heights of adlayer atoms are measured. b) Change in electron density due to interactions within the adlayer and between the surface and adlayer. The difference in electron density is calculated by subtracting the electron densities of isolated atoms in the adlayer and the pristine Ag(111) surface from that of the interacting RbI/Ag(111) system: $\Delta\rho_e = \rho_{RbI/Ag(111)} - \rho_{Ag(111)} - \sum\rho_{Rb} - \sum\rho_I$, where the sums are taken over each atom of the adlayer in isolation. The overlaid contour shows the total electron density at 0.135 electrons Å^{-3}. c) Atomic model of hexagonal RbI monolayer, showing the path along which the electron density is sliced in (a) and (b).

In order to qualitatively gauge the relative strengths of the RbI-Ag and Rb-I interactions, it is instructive to visualize the difference between the electron density of the RbI/Ag system and the isolated electron densities of neutral Rb and iodine atoms, as well as the bare Ag surface (Figure 3.3b). This electron density map shows that the strongest charge transfer is within the RbI layer, corresponding to the filling of the iodine p-orbitals, indicated by an increase in iodine electron density in the directions of neighboring Rb atoms (the diffuse decrease in electron density

surrounding Rb atoms indicates charge transfer out of their s-orbitals). Similarly, the decrease in electron density perpendicular to the surface at each iodine atom is mostly due to rehybridization of orbitals as a result of bonding with adjacent Rb atoms. However, the charge redistribution at the RbI-Ag interface is clearly significant, a consequence of both charge transfer and image charge formation. Image charge formation, present both at the I-Ag and Rb-Ag interfaces, leads to a more long-range interaction than that caused by charge transfer (between iodine and Ag), which implies that the energetics of RbI monolayers are more sensitive to the placement of iodine (rather than Rb) atoms on the Ag surface. To quantitatively gauge the sensitivity of RbI-Ag charge transfer to the iodine and Rb placement, we calculated the energies of individual iodine and Rb atoms on a pristine Ag(111) surface (Appendix, Figure A.4). Our results indicate that iodine atoms strongly prefer hollow sites (located in the pocket between three Ag atoms) over top sites (located directly on top of an Ag atom), with a difference in energy of 0.44 eV between the two configurations. Despite exhibiting the same binding preference, Rb atoms favor hollow sites by only 0.06 eV, which supports the view that the energetics of the RbI monolayer are more sensitive to the placement of iodine. Guided by these results, we carried out calculations of several different RbI monolayers with similar hexagonal structures, but with different registries to the Ag(111) surface (Appendix, Figure A.5). The unit cell of the lowest-energy RbI structure found in these calculations (Figure 3.2c) contains two iodine atoms at hollow Ag(111) sites, consistent with our calculations for individual adatoms.

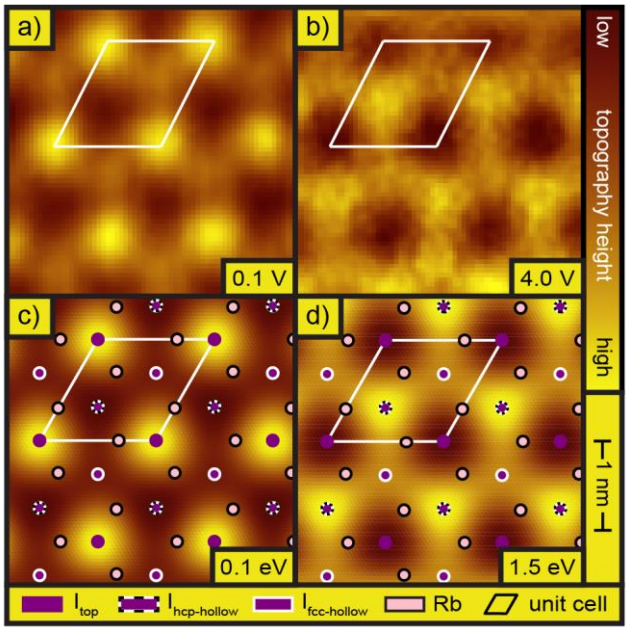

Figure 3.4. a,b) STM topographies (I = 30 pA) showing an inversion of features between bias voltages of 0.1 and 4.0 V. Overlaid white outline corresponds to the smallest periodic unit of the hexagonal monolayer. c,d) DFT calculated LDOS maps integrated from the Fermi level up to 0.1 and 1.5 eV with the optimized adlayer structure and unit cell overlaid. At higher energies, we expect the bias voltages used in experiment to be larger than the energies used to simulate the corresponding LDOS map. This is due both to the well-known tendency of DFT to underestimate the band gap and also the presence of d-states in the Ag tip which, at bias voltages above ~1.5 V, tunnel into states near the Fermi level of the sample, reducing topographic contrast between the low and high energy states. Thus, we found it necessary to increase the bias voltage to around 4 V to clearly resolve the higher-energy states via STM topography.

As a final test of the hexagonal RbI monolayer structure, we carried out simulations of the STM images associated with different RbI structures. Experimental STM topographies show an inversion of contrast as the bias voltage changes from 0.1 V to 4 V (Figures 3.4a and 3.4b). Among the different RbI structures simulated, only the one shown in Figure 2c shows the same patterns as those in Figures 3.4a and 3.4b, as shown in Figures 3.4c and 3.4d. Analysis of the LDOS composition of simulated images allows us to identify the origins of the observed contrast. At 0.1 V, iodine atoms have more unoccupied states (see Appendix, Figure A.1) and dominate the tunneling current, with the topographic contrast originating from variations in the heights of iodine

atoms above the surface, in agreement with previous results for other alkali halides where the topographic contrast near the Fermi energy originated from halide atoms.[10-15] Meanwhile at 4 V, the tip is further away from the surface, the spatial resolution is reduced, and the STM images are dominated by the RbI LDOS (rather than by the RbI structure). Variations in the heights of iodine atoms above the surface (responsible for the contrast in Figure 3.4a) follow directly from their distinctly different adsorption sites (Figure 3.3): the iodine directly on top of an Ag atom (I_{top}) has the largest height above the surface, while the two iodines at hollow sites ($I_{fcc\text{-}hollow}$ and $I_{hcp\text{-}hollow}$) sit deeper in a pocket of three Ag atoms. Further, the proposed hexagonal RbI monolayer structure contains two distinctly different hollow-site iodines in each unit cell (Figure 3.3), if one considers their second-nearest-neighbor coordination to the second layer of Ag atoms below the surface. Specifically, first-layer Ag atoms directly coordinated to one of the hollow-site iodines can either be coordinated to a total of six or seven Ag atoms in the second layer. This has observable consequences in Figure 3.4a (compare to Figure 3.4c), where the hollow-site iodines coordinated to six Ag atoms in the second layer ($I_{hcp\text{-}hollow}$) appear brighter than the ones coordinated to seven atoms ($I_{fcc\text{-}hollow}$). This behavior is reproduced in the corresponding simulated STM image (Figure 4c), and is attributable to the fact that higher second layer coordination facilitates iodine to Ag electron transfer, as well as formation of an image charge at the Ag surface. Both effects lead to a stronger attractive force, which leads to a more deeply seated $I_{hcp\text{-}hollow}$ iodine. Meanwhile, at larger biases corresponding to Figure 3.4b, Rb has the most unoccupied states, providing the most significant contribution to the tunneling current. However, all Rb atoms in the hexagonal phase have the same coordination (Figure 3.2c) and identical LDOS contributions to the tunneling current (Figure A..3), which, in combination with the diffuse nature of Rb orbitals at higher energies (and reduced spatial resolution at larger tip-sample separations associated with higher

bias), lead to a lack of contrast attributable to Rb atoms in Figure 3.4b. On the contrary, the iodine atoms do show substantial variations in their LDOS (Figure A..3), and define the contrast in Figure 3.4b: the two I_{hollow} iodines each provide similar contributions to the tunneling current, while the top-site iodine I_{top} provides the least. We attribute this observation to local differences in I-Ag charge transfer: our DFT calculations show that the I_{top} iodine has a larger net electron count (+0.710) than either $I_{fcc\text{-}hollow}$ (+0.634) or $I_{hcp\text{-}hollow}$ (+0.632), and thus has fewer unoccupied states contributing to the tunneling current, which produces a depression in STM imaging at high biases (Figure 4b).

We now move on to the structural characterization of the "square planar" ("square" in the following) phase type. At low bias voltages (Figure 3.5a), STM topographic scans of this phase consist of approximately identical protrusions, which can be described by two orthogonal lattice vectors oriented parallel ($S_{1\bar{1}0}$) and perpendicular ($S_{11\bar{2}}$) to the $[1\bar{1}0]$ direction of the Ag(111) surface. The magnitude of these lattice vectors is similar to the nearest-neighbor distance in bulk

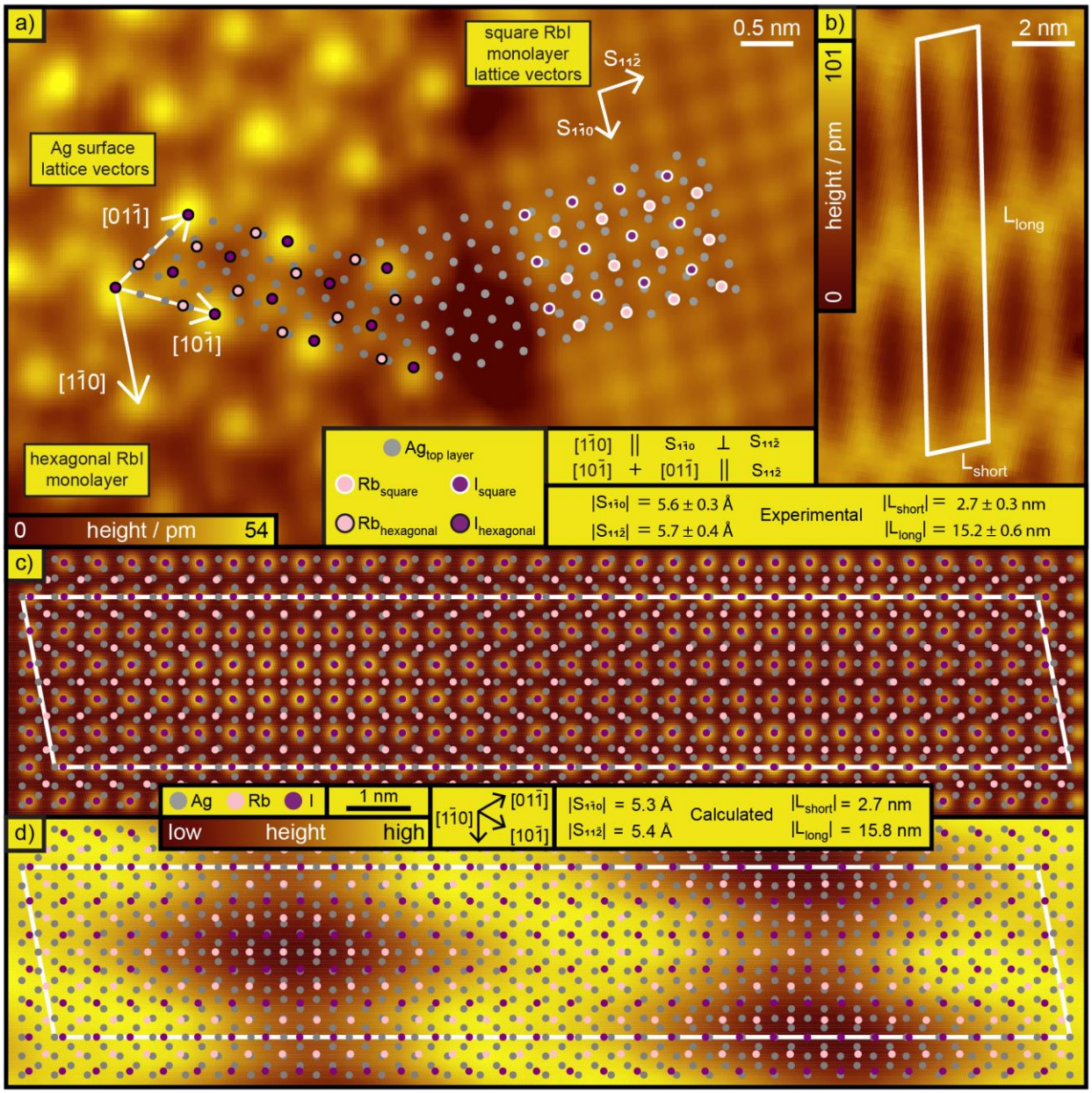

Figure 3.5. a) STM topography (V_b = -10 mV, I = -100 pA) of a domain boundary between hexagonal (left) and square (right) RbI monolayers, showing the orientation of topographic features in each domain type with respect to the Ag(111) surface. b) STM topography (V_b = 2.0 V, I = 10 pA) of a square RbI domain, with the unit cell of the moiré pattern overlaid. c,d) DFT-calculated LDOS map of the square domain integrated up to 0.1 and 1.2 eV above the Fermi level. The superstructure matrix (M) of the moiré pattern is $\begin{pmatrix} 8 & 2 \\ -31 & 62 \end{pmatrix}$ for Ag and $\begin{pmatrix} 5 & 1 \\ 0 & 30 \end{pmatrix}$ for RbI: $\begin{pmatrix} L_{short} \\ L_{long} \end{pmatrix} = M_{Ag} \begin{pmatrix} 1\bar{1}0 \\ 10\bar{1} \end{pmatrix} = M_{RbI} \begin{pmatrix} S_{1\,\bar{1}\,0} \\ S_{1\,1\,\bar{2}} \end{pmatrix}$

RbI (5.3 Å), which suggests that these protrusions are individual atoms of the same species. Since our calculations of the hexagonal phase consistently show that the tunneling current is dominated by unoccupied iodine states at low voltage (see Appendix, Figure A.1), we identify these protrusions as individual iodine atoms. This is consistent with STM results of NaCl, which show that individual Cl atoms are imaged as protrusions at low bias voltages.[11, 13, 14] Importantly, while vectors $S_{1\bar{1}0}$ and $S_{11\bar{2}}$ are parallel to $[1\bar{1}0]$ and $[11\bar{2}]$ of the Ag(111) surface, they are 80.1% and 4.0% longer than the $[1\bar{1}0]$ and $[11\bar{2}]$ lattice vectors respectively, which highlights the incommensurability of the square RbI phase and Ag(111). This incommensurability manifests itself most dramatically in STM images obtained at higher bias voltages (compare Figures 3.1b and 3.1c), where we observe a moiré pattern with a unit cell defined by two distinct lattice vectors (L_{short} and L_{long}) forming an angle of approximately 79° (Figure 3.5b).

To further characterize the structure of the moiré pattern formed by the square RbI phase, we have used DFT to optimize a variety of structures exhibiting square symmetry and the periodicity shown by L_{short} and L_{long}. The resulting structure (Figure 3.5c,d) reproduces the magnitudes of all experimental lattice parameters ($S_{1\bar{1}0}$, $S_{11\bar{2}}$, L_{short}, L_{long}) to within the error of our measurements. Using this structure, we have simulated STM images at small and large bias voltages to compare to our experimental findings (Figure 3.5c,d). At low bias (Figure 3.5c), the topography consists of protrusion features corresponding to individual iodine atoms, which is consistent with our experimental findings. When the bias is larger (Figure 3.5d), our simulated topography yields elongated depression features similar to those observed in experiment. This provides a useful visualization of how the adlayer LDOS varies with registry to the Ag(111) surface, because the simulated topography cannot be attributed to the morphology of the RbI structure (see Appendix, Figure A.6). The elongated "dark" regions of the topography consist of

iodine atoms that are coordinated mostly to just one Ag atom, while the surrounding "bright" regions consist of iodine atoms coordinated to two or three Ag atoms. Similarly to our findings for the hexagonal phase, our DFT calculations show that for iodine in the square phase, the extent of surface/adlayer coordination is inversely related to the net electron count (most coordinated iodine: +0.688 electrons; least coordinated iodine: +0.706 electrons). In comparison, the range of net electron counts for Rb is much narrower (between -0.819 and -0.811 electrons) and is less closely related to the surface/adlayer coordination (see Appendix, Figure A.7). These results show that iodine is more significantly involved in charge transfer between the substrate and adlayer. Additionally, since more (less) electron transfer from the adlayer to the substrate results in more (fewer) unoccupied states, these findings suggest that the coordination of iodine is responsible for the contrast observed in STM topography (Figure 3.5d). This conclusion is consistent with our results for the hexagonal phase, which highlights the important role that substrate/adlayer coordination plays in determining charge transfer and the LDOS in both phase types of the RbI monolayer.

Finally, we discuss the origin of the structural bistability observed in the RbI monolayer. We have calculated the binding energy of the square phase to be 0.24 eV per RbI molecule larger than for the hexagonal phase, indicating that the hexagonal phase is strongly energetically preferable (see Appendix, Table A.1). However, despite being less energetically favorable, the square phase boasts a more efficient packing of RbI atoms, with calculated densities $\rho_{square} = 7.18$ atoms nm^{-2} vs $\rho_{hexagonal} = 5.01$ atoms nm^{-2}. When the density of RbI atoms on the surface is greater than the maximum planar density of the hexagonal structure ($\rho_{hexagonal}$), one could expect RbI to either: 1) form a second layer on top of the hexagonal monolayer; or 2) adopt a denser configuration of the monolayer and reconstruct to the square phase. To test the likelihood of these

possibilities, we utilized DFT to optimize a double-layer form of the hexagonal structure (see Appendix, Figure A..8), which resulted in a planar density of 10.02 atoms nm^{-2} and a binding energy that is 0.32 eV per RbI molecule larger than for the single-layer hexagonal structure. This indicates that it is energetically favorable (by 0.08 eV per RbI molecule) for the monolayer to reconstruct to the square phase rather than to grow a second hexagonal layer (Appendix, Figure A.9). We emphasize that this discussion of energetic favorability should not be conflated with a characterization of thermodynamic or kinetic stability, as this is beyond the scope of our present work. Rather, we present this density-dependent picture to understand how the energetic preference for monolayer growth contributes to the structural coexistence observed by STM.

However, the described density-dependent picture of RbI monolayer growth on Ag(111) does not take into consideration the effect of Ag step edges, which serve as nucleation sites for preferential growth of square phase RbI islands (see Appendix, Figure A.10). This behavior (also reported for other alkali halides[15]) can be explained by considering the local electrostatics of the different RbI phases and Ag step edges. Indeed, due to the Smoluchowski effect,[41-43] the top (bottom) side of a Ag step edge is positively (negatively) charged and favors binding of the anions (cations). Due to this electrostatic environment, one thus expects RbI to nucleate along a Ag step in an orientation that would result in a single atom type along the $[1\bar{1}0]$ direction (step edge orientation) of Ag. Only the square phase satisfies this requirement (Figure 3.5c,d), while the hexagonal phase has equal numbers of Rb and iodine atoms along the $[1\bar{1}0]$ direction of Ag (Figure 3.2b,c) resulting in a less favorable electrostatic Ag-RbI interaction. We thus predominantly observe square phase RbI islands in the vicinity of Ag step edges, even though we have also observed counter examples of this behavior, with hexagonal RbI existing across Ag step edges in

situations where several Ag step edges present competing nucleation sites with incompatible orientations (Appendix, Figure A.11).

3.4 Conclusions

To summarize, we have identified and characterized two distinct single-layer structures of RbI, which are structurally different from that of the bulk crystal. We show that the prevalence of a particular phase is determined by the local structure of the Ag surface: the square RbI structure is better matched to the Ag step edges, whereas the hexagonal RbI structure is commensurate with the Ag(111) atomic structure. The Ag-RbI interface is energetically more favorable than an interface between RbI layers, which results in the dominance of the (denser) square phase at higher RbI surface coverages. Both phases exhibit non-trivial contrast in STM images, with apparent heights of individual atoms determined by their local coordination to the Ag surface. We hope that the simplicity of the presented physical picture may lend itself to qualitative understanding of other heterostructures involving ionic and metallic layers.

3.5 Bridge to Chapter IV

Thus far we have shown that substrate-adlayer interactions can result in structural coupling, where the substrate serves as a template for the growth of the adlayer. Our experimental and computational results suggest that this coupling is accompanied by corresponding changes in electronic structure, where the strength of substrate-adlayer interactions for the two distinct single-layer RbI structures impacts the electronic structure differently. In the following section, we explore the differences in electronic structure between

the two bi-stable, co-existing single-layer RbI structures, and discuss how these differences are induced by coupling between the substrate and adlayer.

CHAPTER IV

PROBING THE ELECTRONIC STRUCTURE OF BI-STABLE SINGLE-LAYER RBI STRUCTURES ON Ag(111)

From McDowell, B.W.; Mills, J.M.; Green, A.W.; Honda, M.; and Nazin, G.V.; Probing the Electronic Structure of Bi-Stable Single-Layer RbI Structures on Ag(111). (accepted – Phys. Rev. B, 2024)

4.1. Introduction

As materials are reduced in scale to ultra-thin layers, they can exhibit unusual electronic properties that are distinct from those found in the bulk material.[1-4] One particular example is the loss of a well-defined band gap in many ultra-thin dielectrics, which poses problems in the continued effort to miniaturize electronic devices where insulating materials are a fundamental component.[5] The loss of a well-defined band gap can result, in part, from interactions with metal substrates. These interactions have been shown to impact ultra-thin dielectric layers through changes in structure[6-10] and electronic properties, such as spatial modulation of both the work function[11, 12] and interface electronic states.[13-16] An understanding of the relationship between ultra-thin dielectrics and the substrates on which they are grown necessitates direct visualization of the atomic and electronic structure, making scanning tunneling microscopy/spectroscopy (STM/STS) a leading tool for its ability to probe these features with nanoscale resolution.[17]

While there are a diverse range of choices for ultra-thin dielectrics, alkali halides are a common choice for their wide band gap[18, 19] and well defined atomic structure.[12, 20-23] Of the alkali halides, NaCl has been the most extensively studied and has been demonstrated to be

influenced by substrate interactions, which lead to formation of spatially-modulated electronic states at the metal-insulator interface[13, 14] and a work function that varies spatially with the substrate/adlayer registry.[12] A promising alternative to NaCl with which to study the effect of substrate-adlayer interactions in ultra-thin dielectrics is RbI, which has been shown to have stronger interactions with metal substrates due to weaker alkali-halide bonds.[6, 15] These stronger interactions are evidenced by structural coupling to the metal substrate on Ag(111), where RbI was shown to form unexpected structures with hexagonal symmetry (matching that of the face-centered-cubic surface), in contrast to the square symmetry expected for typical alkali halides forming rock-salt-like structures.[6] However, it is not well understood how the strong substrate-adlayer interactions present for ultra-thin RbI layers affects the electronic properties of the dielectric. It is important to understand the role of substrate-adlayer interactions in determining electronic properties of ultra-thin dielectrics, as these effects have direct implications in the behavior of nanoscale electronic devices. In considering this, it is informative to consider how substrate-adlayer interactions might vary locally, for example at structural defects like those previously shown to impact local electronic structure in alkali halide thin films.[13, 24-26] Here, we use RbI to study, with STM/STS, how interactions with the substrate affect the electronic properties of ultra-thin RbI on Ag(111).

4.2. Methods

Experiments were carried out in a home-built ultrahigh vacuum (UHV) cryogenic STM system, in which the bias voltage (V_b) is applied to the sample.[27] All imaging and spectroscopic measurements were carried out at 26 K using electrochemically etched silver tips,[28] at a base pressure of approximately 3.0×10^{-11} torr. A Ag(111) single crystal was prepared in situ by

sputtering with Ne followed by annealing, which was repeated for multiple cycles. A sub-monolayer of RbI (obtained from Sigma-Aldrich, 99.9% purity) was deposited onto the Ag surface (held at room temperature) via in situ sublimation under UHV conditions. After deposition of RbI, the sample was annealed for one hour at approximately 320 K. All STS spectra were recorded with the feedback left on on during STS acquisition, in line with previous studies of IPS.[29]

Computations were performed using DFT[30] as implemented by the Vienna Ab Initio Simulation Package (VASP)[31-33] with a projector-augmented plane wave basis set.[34] The Ag(111) surface was constructed with data obtained from the Materials Project[35] with approximately 25 Å of vacuum added to prevent interaction of periodic unit cells perpendicular to the surface. The hexagonal RbI structure was optimized on three layers of Ag (with the bottom layer frozen to retain the bulk lattice constant) via the PBE functional for solids (PBE_{sol})[36] until all forces were less than 0.005 eV $Å^{-1}$, using a 5 × 5 × 1 k-point mesh centered at the Γ point and a 500 eV planewave cutoff. The unit cell size of the square RbI structure (300 Rb,I atoms + 558 Ag atoms per layer) was prohibitive to performing calculations at the same level of accuracy, and was optimized on a single, frozen layer of Ag via the PBE_{sol} functional at the Γ point with a 500 eV planewave cutoff until all forces were less than 0.05 eV $Å^{-1}$. All electronic structure calculations were optimized until the change in energy between iterative steps was less than 10^{-8} eV. To characterize charge transfer between atoms, we used Bader analysis[37-40] with a vacuum cutoff of 10^{-3} electrons $Å^{-3}$, which kept all atomic volumes within 5% of the average for each atomic species. The change in potential due to RbI-Ag interaction was calculated by subtracting the total potential (composed of ionic and Hartree components) of the isolated RbI/Ag structures

from the composite system: $\Delta E(r) = E(r)_{Ag/RbI} - E(r)_{Ag} - E(r)_{RbI}$. Visualizations of all structures were made using the VESTA package.[41]

Simulations of IPS were performed using a Numerov-Cooley algorithm for integrating wavefunctions in a one-dimensional potential described elsewhere,[29] where we used a spherical-tip approximation to calculate the electric field between the tip and sample.[42] The lattice component of the potential was determined by the nearly free electron model which reproduced the Ag(111) band gap[43] with values of Vg=2.1 V, V0=4.634, and a lattice spacing of 237.0 pm.[35] The thickness of the RbI monolayer was determined from experimental STM data recorded at the bias voltage of the STS setpoint: w_{square} = 0.24 nm, $w_{hexagonal}$ = 0.25 nm.

4.3. Results and Discussion

After depositing sub-monolayer RbI on Ag(111), we observe the co-existence of two distinct RbI structures (Figure 4.1a), in line with previous results.[6] The structural distinctions between these RbI phases has been reported elsewhere,[6] and we describe them briefly here. One RbI structure exhibits square-like symmetry (square in the following) and is analogous to the (100) plane of bulk RbI. The other RbI structure has hexagonal-like symmetry (hexagonal in the following), adopting the symmetry of the Ag(111) surface. To explore the electronic structure of each RbI structure we record STS measurements on each RbI phase, focusing on the energy range in which we expect to find image potential states (IPS), which have been useful previously in characterizing the electronic properties of insulating thin films.[12, 29] Our STS spectra show that the energies of IPS are distinct between hexagonal and square RbI, both of which are significantly different from the spectra recorded on bare Ag(111) (Figure 4.1b). Importantly, the distinct IPS spectra for each RbI phase suggests a difference in electronic properties.

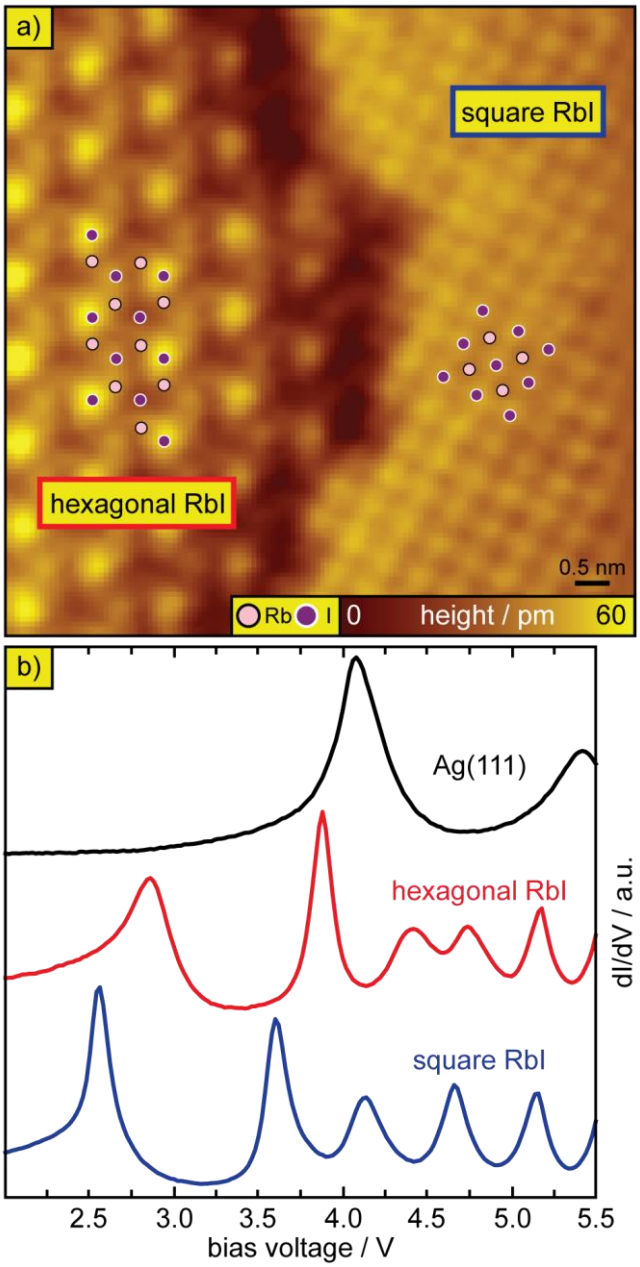

Figure 4.1: Representative STS of IPS on RbI/Ag(111). a) STM topography (V_b = -50 mV, I = -200 pA) of a region of RbI showing co-existence of hexagonal (left side) and square (right side) RbI structures. b) Representative STS spectra (I = 10 pA , V_{pp} = 40 mV) recorded on each RbI structure type, where the feedback was left on during STS acquisition, in line with previous studies of IPS.[29]

To understand how differences in electronic properties could result in distinct IPS spectra for each RbI structure, we have modeled our STS results using methods previously employed to simulate IPS spectra of alkali halides.[29] Here, we use a one-dimensional potential to simulate the

IPS of bare Ag(111) (see Appendix, Figure B.1 for representative simulated wavefunctions), which, by fitting to our experimental results (Figure 4.1b), allows us to calculate the work function of the tip (ϕ_{tip}), the tip radius (R), and the tip-sample separation (z_0) at the low-voltage boundary of the spectra shown in Figure 4.1b (the tip-sample separation increases in these spectra with voltage while the tunneling current is maintained constant). The values calculated for bare Ag(111) serve as input parameters for the simulation of IPS spectra on RbI, which we optimize to fit our experimental results by varying the work function of the sample (ϕ_{sample}), the dielectric constant of single-layer RbI (ε), and the conduction band energy of RbI (V_{cbm}). Our simulated IPS energies agree well with our experimental results, with all simulated energies falling within one standard error of experiment (Figure 4.2), and the calculated parameters showing consistency between data sets obtained with different STM tips (Table 4.1).

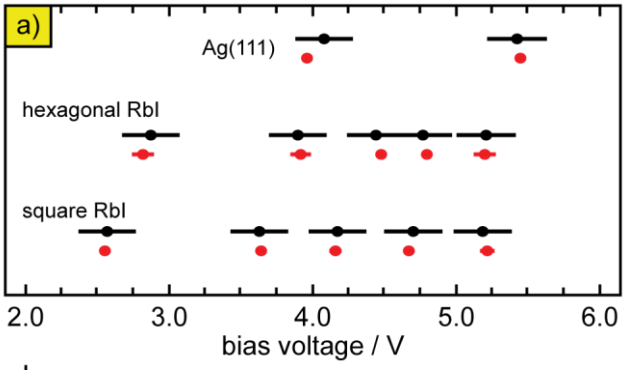

Figure 4.2: Experimental and simulated IPS energies. Comparison of simulated (red) to experimental (black) IPS energies. The horizontal bars are the standard error of experimental STS data obtained with five different tips summed in quadrature with the measurement's uncertainty resulting from the amplitude of bias oscillation in the STS measurement (40 mV peak-to-peak).

	Ag		Hexagonal RbI	Square RbI
z_0 (nm)	1.55 ± 0.09	ϕ_{sample} (eV)	2.42 ± 0.14	3.11 ± 0.07
ϕ_{tip} (eV)	3.70 ± 0.04	ε	2.98 ± 0.01	1.98 ± 0.10
R (nm)	4.33 ± 0.03	V_{cbm} (eV)	2.94 ± 0.01	3.04 ± 0.01

Table 4.1: Optimized parameters used to simulate IPS spectra. The initial tip-sample separation (z_0), work function of the tip (ϕ_{tip}), and tip radius (R) were calculated by fitting simulated results to experimental STS measurements obtained with five different tips. Using the optimized parameters for each tip, results were then simulated for each RbI structure type, where the optimized parameters were the work function of the sample (φ_{sample}), the dielectric constant of the RbI structure (ε), and the conduction band energy (V_{cbm}). The reported values are the average and standard deviation of results using experimental STS data from five different tips.

Examination of the simulated parameters in Table 1 shows clear distinctions in electronic properties between the two RbI structure types. Of the three parameters simulated for RbI, there are significant differences in ϕ_{sample} and ε between the two RbI structure types, while V_{cbm} shows similar values for each. Our results show that ϕ_{sample} is smaller (by 0.69 eV) on hexagonal RbI than on square RbI, and both numbers show a reduction in work function from literature values for bare Ag(111) (4.59 eV),[44, 45] in agreement with previous results for NaCl, which also showed reduced values for ϕ_{sample}.[29] The difference in ϕ_{sample} between square and hexagonal RbI is consistent with previous DFT calculations, which showed that hexagonal RbI transfers more electrons to the surface, resulting in a more significant reduction of ϕ_{sample}.[6] There is also a significant difference between the dielectric constants of hexagonal and square RbI, with the value for square RbI being greater by 1.00. Each of these values shows a significant decrease in dielectric constant relative to the bulk value (4.83)[46] which is in line with previous results for ultra-thin NaCl layers.[29] The observed difference in dielectric constant between hexagonal and square RbI can be explained by the bonding at the metal/dielectric interface: iodine atoms in hexagonal RbI interact more strongly with Ag(111) than in the square RbI structure, resulting in formation of Ag-I covalent bonds near the Fermi level,[6] in line with similar results for NaCl.[12, 22, 23] Consequently, the more significant presence of interfacial covalent bonding in the hexagonal

RbI structure leads to a greater polarizability than for the square RbI structure. Finally, our simulated results show similar values for the conduction band energies of square and hexagonal RbI. This is in agreement with our DFT calculations, which show that this value is affected by conflicting factors: the reduced (increased) adlayer coordination and longer (shorter) average Rb-I bond length of hexagonal (square) RbI suggests a smaller (wider) band gap (see Appendix, Figure B.2), but the stronger (weaker) interaction of hexagonal (square) RbI with Ag suggests a more (less) significant widening of the band gap due to substrate-adlayer interaction (see Appendix, Figure B.3). Overall, we find that our calculation of electronic properties from the IPS spectra of RbI is in agreement with our DFT calculations and previous work.[6]

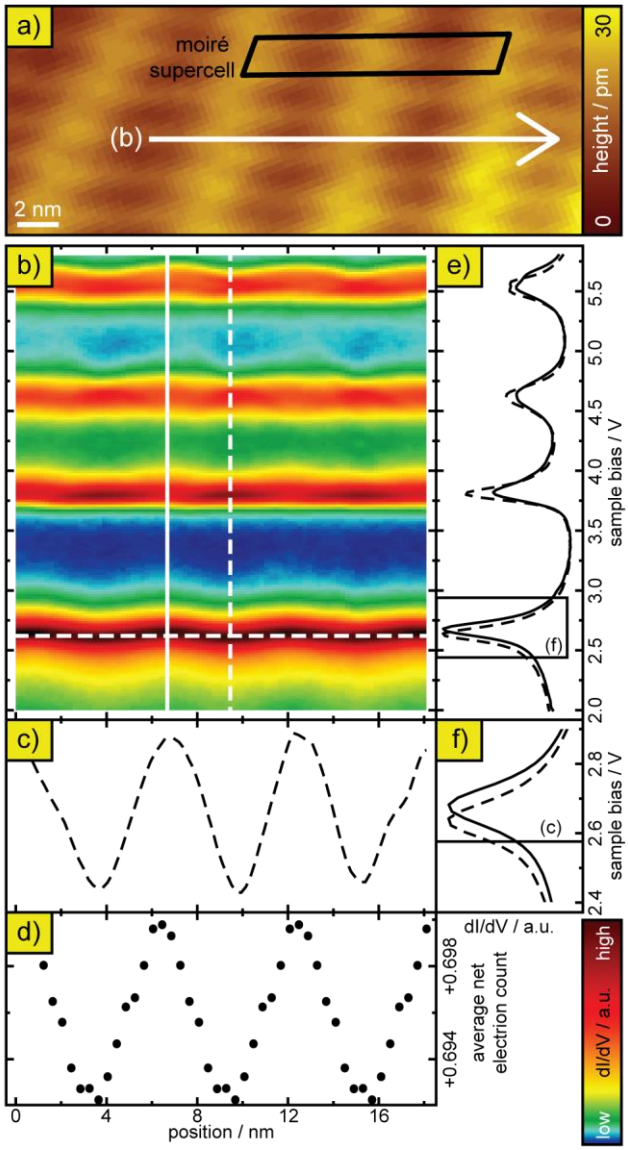

Figure 4.3: STS measurements of spatial modulation of IPS energy in square RbI. a) STM topography (V_b = 2 V, I = 10 pA) of a square RbI monolayer, indicating the path along which a progression of STS measurements were taken in (b). b) Progression of STS measurements taken along the spatial path shown in (a). c) Spatial variation in downshifted first IPS, showing STS data from the horizontal dashed line in (b). d) Spatial variation in DFT-calculated net electron counts, averaged along the <100> RbI direction orthogonal to the STS path. e) Individual STS spectra showing distinctions in energy of the lowest-energy IPS for different regions of the moiré supercell. The spectra correspond to the position of the vertical lines in (b). f) Portion of the STS spectra from (e), zoomed-in to highlight difference in the first IPS energy.

Thus far, we have discussed the average behavior of the square and hexagonal RbI structures. However, we also observe local deviations from the described average behavior for

both types of structures, both across the pristine square structure and at defects in the hexagonal structure. For the square RbI structure, we observe spatial variations in the IPS spectra that match the periodicity of the moiré structure formed between square RbI and Ag(111). This moiré pattern is characterized in detail elsewhere,[6] and we briefly describe it here: the square RbI structure is incommensurate with the hexagonal symmetry of the Ag(111) surface, resulting in a moiré supercell defined by lattice vectors with magnitudes of 2.7 and 15.8 nm, which are oriented along the $[11\bar{2}]$ and $[1\bar{1}0]$ directions of the Ag(111) surface (Figure 4.3a). By recording a progression of STS spectra along the long axis of the moiré supercell, we observe that the energy of the first IPS varies with position (Figure 4.3b), while the energy of all other IPS remains constant. (We note that there is no spatially-dependent changes in IPS energy along the short moiré axis, see Appendix Figure B.4) The spatial modulation of the first IPS energy is periodic with the long axis of the moiré supercell, and it is downshifted by 0.06 V in the regions which appear taller in STM topography (dashed curve in Figure 4.3e,f) relative to the regions which appear darker and striped (solid curve in Figure 4.3e,f). We find that these distinct IPS energies arise from the moiré structure and can be explained by electrostatics, as detailed in the following. The spatial variations in the downshifted IPS (Figure 4.3c) align with DFT-calculated spatial variations in the net electron counts of iodine atoms (Figure 4.3d), which have previously been shown to participate more significantly than Rb atoms in transferring charge to Ag.[6] Thus, in regions where iodine transfers more electrons to the substrate, the adlayer has a more positive charge, resulting in a stabilizing effect on the IPS. Since the stabilizing electrostatic environment is localized to the adlayer, it follows that the downshifting of the IPS is only clearly observable for the first IPS, since higher order IPS states are further delocalized from the surface. We note that the observed spatial variation in the first IPS is also in agreement with previous studies of

interface electronic states in the RbI/Ag(111) system, which were spatially-modulated by an electrostatic potential commensurate with the moiré supercell.[15]

In addition to local variations in the IPS spectra for the pristine square RbI structure, we also observe local variations at one-dimensional grain boundary defects (GBDs) in the hexagonal RbI structure (Figure 4.4a). To understand how these defects impact the electronic properties of hexagonal RbI, we have recorded STS spectra on many different GBDs, with representative curves shown in Figure 4b. A consistent result of these STS measurements is that the first IPS is downshifted at the defect relative to the pristine hexagonal structure (Figure 4.4b). Further, by mapping individual STS data for specific energies in two dimensions, we are able to characterize the spatial variations in the energy of the first IPS. At a bias voltage of 2.9 V, we observe high LDOS along the GBD (Figure 4.4c), while at higher bias voltages of 3.1 V we observe high LDOS in the pristine RbI region away from the GBD (Figure 4.4d), suggesting that the downshifted IPS is relatively delocalized along the entirety of the GBD. This finding is in agreement with previous results for RbI on Au(111)[24] and for NaCl on Ir(111),[47] which found that the LDOS was, in general, downshifted at GBDs.

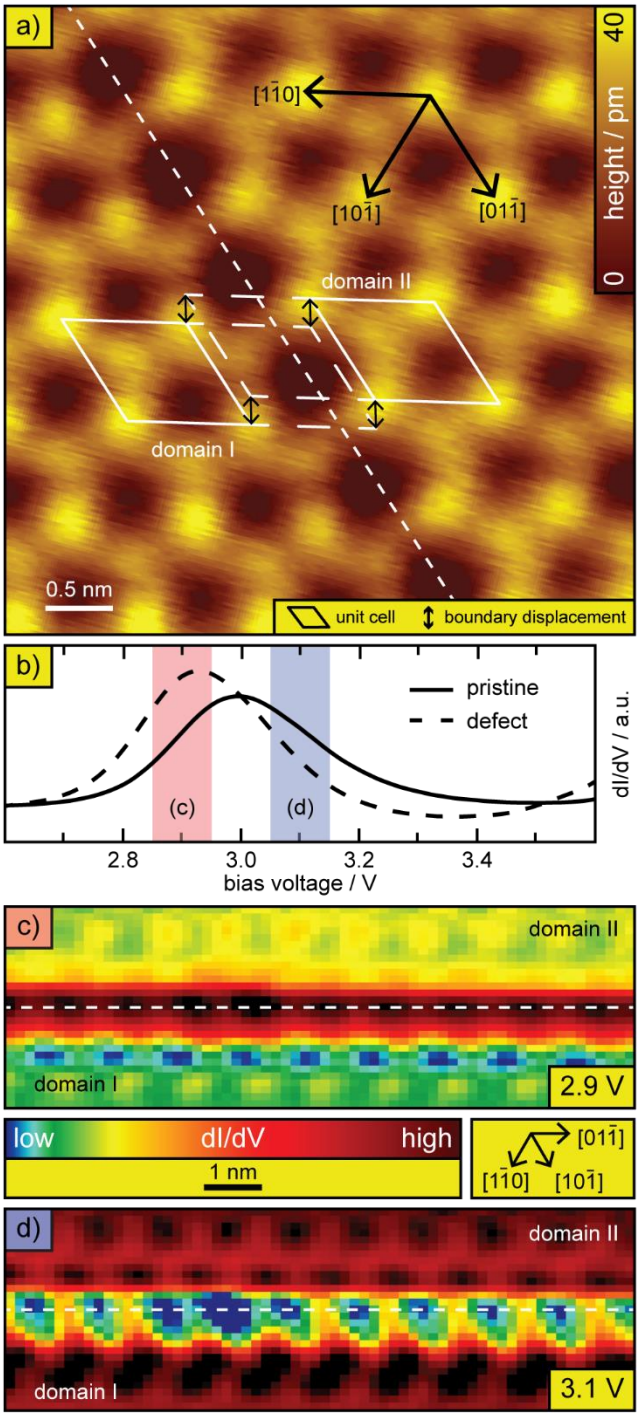

Figure 4.4: STS results for localized IPS at GBD in hexagonal RbI. a) STM topography (V_b = 50 mV, I = 10 pA) of GBD formed between two discontinuous domains of hexagonal RbI, where the pristine unit cell is shown in white and the discontinuity is highlighted by the double-sided arrows. b) Representative STS measurements taken on (dashed curve) and away from (solid curve) the GBD shown in (a). The energy ranges used for two-dimensional STS mapping are overlaid in red (c) and blue (d). c,d) Two-dimensional STS mapping of the GBD shown in (a), where the mapped energies are chosen to show the spatial behavior of the downshifted IPS at

the GBD (c) and the IPS of the pristine hexagonal monolayer (d). The horizontal dashed line shows the orientation of the GBD as in (a).

To understand why the first IPS is downshifted at GBDs in the hexagonal RbI structure, we turn to DFT and, in doing so, must first characterize the atomic structure of the GBD. While our STM images do not resolve the atomic structure of the GBD, we are able to identify the discontinuity between the two pristine RbI domains, which is one Ag lattice spacing (see Figure 5a) for the GBD shown in Figure 4.4. Our DFT calculations indicate that it is energetically unfavorable to leave the polar edges of each RbI domain uncompensated, suggesting that the GBD region is not bare Ag(111). Instead, the two adjacent RbI domains can be bridged by the addition of individual RbI molecules, which our DFT calculations show is best accomplished by a specific atomic structure (shown in Figure 4.5a), in line with previous structural results for GBDs in RbI on Au(111)[24] and NaCl on Ir(111).[47]

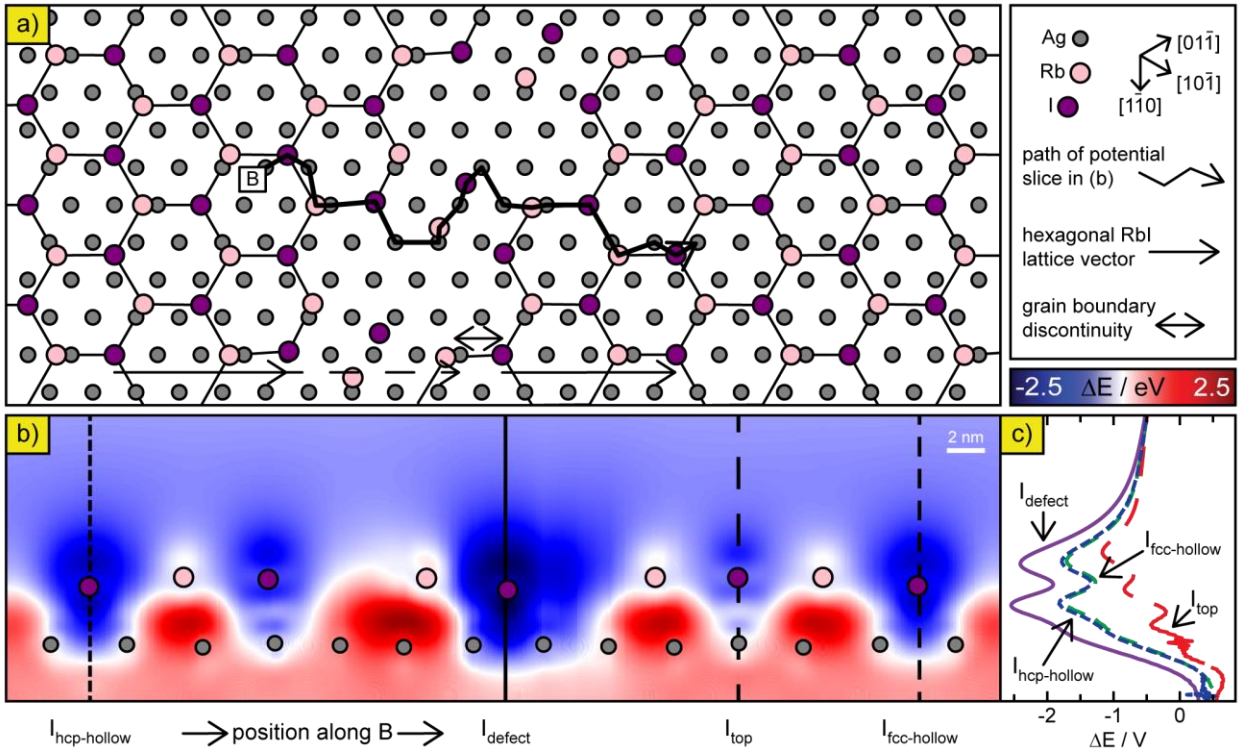

Figure 4.5: DFT-calculated potential for GBD in hexagonal RbI. a) DFT-optimized structure of the GBD shown in Figure 4. The solid horizontal arrows show the lattice vector of the pristine

hexagonal RbI structure, the dashed arrow shows how the pristine lattice vector propagates across the GBD, and the double-sided arrow shows the discontinuity between the structures on either side of the GBD. The segmented solid arrow shows the path along which the change in potential is sliced in (b). b) Change in potential energy of electrons due to adsorption of RbI ($\Delta E(r) = E(r)_{Ag/RbI} - E(r)_{Ag} - E(r)_{RbI}$), is shown in the direction orthogonal to the surface. c) Vertical slices of the potential from (b) are shown for several iodine atoms with distinct adsorption geometry, as indicated by the vertical lines shown in (b).

In order to understand how the GBD might affect the IPS locally, it is instructive to visualize the DFT-calculated change in potential energy of electrons due to adsorption of RbI, as shown in Figure 4.5b. From this, we observe that, in general, iodine (Rb) atoms induce a local decrease (increase) in potential energy, which is a result of the metal surface screening the polar adlayer atoms. Screening of the adlayer atoms by the Ag surface leads to electron depletion (accumulation) near the negatively (positively) charged iodine (Rb) atoms, resulting in local decreases (increases) in potential energy. However, the effect of adsorption on the potential energy is not consistent for each adlayer atom, as is most clearly evidenced by iodine atoms, which have previously been shown to be more sensitive to adsorption site placement than Rb atoms.[6] The effect of distinct adsorption sites can be seen by comparing the change in potential energy for the three distinct adsorption sites in the pristine hexagonal RbI structure: iodine atoms coordinated to a single Ag atom (I_{top}) have a less stabilizing effect than those coordinated to three Ag atoms ($I_{hcp\text{-}hollow}$ and $I_{fcc\text{-}hollow}$) (Figure 4.5c). Our DFT results suggest that this difference in electrostatic behavior between distinct adsorption sites is the result of differences in I-Ag charge transfer, where iodine atoms coordinated to three Ag atoms have lower net electron counts (+0.60 electrons) than those coordinated to a single Ag atom (+0.67 electrons) on average, in agreement with previous studies of hexagonal RbI on Ag(111) which showed that higher coordination of iodine to Ag leads to increased electron transfer to the substrate.[6] The

distinct changes in potential for each adsorption site are thus a result of electrostatics, where the less (more) negatively charged iodine atoms yield a more (less) stabilizing potential.

Importantly, our results show that the effect of reduced coordination within the adlayer is consequential at the GBD, where the electrostatic environment is more stabilizing than in the pristine RbI structure (compare I_{defect} to $I_{hcp/fcc\text{-}hollow}$ in Figure 4.5c). At the GBD, there is significantly less coordination within the adlayer, as highlighted by a longer than average Rb-I bond length (4.50 Å at the defect vs 3.97 ± 0.12 Å in the pristine hexagonal structure). This distinction in adsorption site is accompanied by a significant increase in I-Ag electron transfer, resulting in a smaller net electron count for iodine atoms at the GBD (+0.50 electrons) relative to those in the pristine hexagonal RbI structure (+0.62 electrons, on average). In contrast, despite a similarly increased Rb-I bond length, Rb atoms at the defect show similar net electron counts when compared to the pristine hexagonal RbI structure (-0.83 vs -0.84 electrons), in agreement with previous studies of RbI on Ag(111), which found that Rb atoms are less sensitive to adsorption site placement than iodine atoms. Thus, the smaller net electron counts for iodine atoms at the GBD leads to a stabilizing potential, which lowers the energy of the first IPS. This effect is only observed for the first IPS, since higher-order IPS are less confined to the surface and less sensitive to changes in the potential at the adlayer. Furthermore, while we have presented data on only a single GBD structure here, our STS results show that other RbI GBDs behave similarly on Ag(111), which our interpretation suggests is due to local stabilizing electrostatic potentials arising from increased substrate-adlayer interaction at the defect. The physical picture offered here may be similar for GBDs in other ultra-thin dielectrics where substrate adlayer interactions are locally stronger at the defect.

4.4 Conclusions

To summarize, we have used STM/STS to study image potential states associated with two structurally different phases of single-layer RbI on Ag(111). By comparing experimental STS data to simulations, we have quantitatively evaluated the electronic properties of these two RbI structures, revealing notable disparities in the electrostatic behavior of the two distinct structural phases. In line with these results, we find that variations in the local electrostatic environment are, to a large extent, responsible for local variations in the image potential state behavior, arising from the moiré pattern of the square RbI structure and defects in the hexagonal RbI structure. The comparison of electrostatic behavior between the two RbI structure types and characterization of local variations in each structure type offers insight on how substrate-adlayer interactions can impact the adlayer electronic properties.

4.5 Bridge to Chapter V

In this chapter we have shown that distinct strengths of coupling between the substrate and adlayer leads to different electronic properties. Furthermore, local electrostatic environments, which form due to coupling between the adlayer and substrate, result in local electronic structure features, namely spatial variations in the behavior of image potential states. In the following chapter, we expand this discussion of local electrostatic environments to two-dimensional electronic states confined to the substrate-adlayer interface. We discuss how this electrostatic environment arises from coupling between the substrate and adlayer, and the effect this environment has on the electronic structure of the substrate-adlayer interface.

CHAPTER V

SPATIALLY-MODULATED INTERFACE STATES IN A TWO-DIMENSIONAL POTENTIAL: SINGLE-LAYER RBI ON Ag(111)

From McDowell, B.W.; Mills, J.M.; Honda, M.; and Nazin, G.V.; Spatially-Modulated Interface States in a Two-Dimensional Potential: Single-layer RbI on Ag(111). *J. Chem. Phys.* **2023**, 159 (22). 224705.

5.1. Introduction

Surfaces and interfaces play an essential role in the electronic properties of nanomaterials. In particular, metal-insulator interfaces are fundamental components of nanoscale devices, and the ability to tune their electronic properties remains an exciting prospect.[1, 2] At the nanoscale, metal-insulator interfaces can exhibit interface electronic states (IES), which are distinct from the surface states (SS) of the metal-vacuum interface, as reported for a variety of metal-insulator interfaces including organic thin films,[3-5] noble gas thin films,[6-9] and alkali halide thin films.[10-16] IES show behavior that is different from that of the bulk metal including doping effects from adsorbates,[17-19] spatial modulation by moiré superlattices,[1, 10, 20-23] and unique electronic structures, such as Dirac cones[22-24] or topological states,[25, 26] emphasizing the importance of understanding the electronic structure of metal-insulator interfaces.

While a wide range of metal-insulator interfaces have been studied, alkali halides have attracted attention due to their wide band gap[27, 28] and well-defined atomic structure.[29-33] Of the alkali-halides, NaCl has been the most well-studied, and has been shown to result in an IES on a variety of metallic substrates, such as Ag(111),[10-12] Cu(111),[13, 14] and Au(111).[15, 16] These IES

exhibit electronic structures that are distinctly different from the SS present at metal-vacuum interfaces, and it has been shown that their electronic structure can be tuned by modifying the interface by, for example, varying the size of adlayer domains[11, 15] or changing the adlayer thickness.[16] While it is possible that these states might be modified further by using an alkali-halide with stronger substrate-adlayer interactions, it is not well-known how strong substrate-adlayer interactions impact the IES at metal/alkali-halide interfaces, although it has been shown that metal oxides, which have a stronger substrate-adlayer interaction than NaCl, result in IES that exhibit increased onset energy, a larger band gap, and flatter bands.[34]

An interesting alternative to NaCl is RbI, where the alkali-halide interaction is weaker and there is a stronger interaction between the adlayer and substrate, as indicated by the adsorption energies reported for RbI (0.30-0.54 eV per alkali-halide pair)[35] being, in general, larger than those for NaCl (0.25-0.41 eV per alkali-halide pair).[32, 33] This strong interaction between RbI and metal surfaces has been shown to result in spatially inhomogeneous charge redistribution effects (transfer, polarization, etc.) that are significantly larger in magnitude than for NaCl monolayers[32, 33, 35] leading to a more profound effect on the IES in this system.[10, 13] An important tool for studying the spatially-dependent electronic structure of IES is scanning tunneling microscopy/spectroscopy (STM/STS), which can directly probe electronic structure with atomic-scale precision.[1] However, to our knowledge, no STM/STS-based study of IES in RbI systems, where the IES modulation is expected to be more pronounced, has been reported in the literature.

5.2. Methods

Experiments were carried out in a home-built ultrahigh vacuum (UHV) cryogenic STM system, in which the bias voltage (V_b) is applied to the sample.[36] All imaging and spectroscopic measurements were carried out at 26 K using electrochemically etched silver tips, at a base pressure of approximately 3.0×10^{-11} torr. A Ag(111) single crystal was prepared in situ by sputtering with Ne followed by annealing, which was repeated for multiple cycles. A sub-monolayer of RbI (obtained from Sigma-Aldrich, 99.9% purity) was deposited onto the Ag surface (held at room temperature) via in situ sublimation under UHV conditions. After deposition of RbI, the sample was annealed for one hour at approximately 320 K. The STM feedback is turned off during all STS measurements, and where multiple spectra are shown the feedback is turned on for ~100 ms between spectra.

All computations were performed using density functional theory (DFT)[37] as implemented by the Vienna Ab Initio Simulation Package (VASP)[38-40] with a projector-augmented plane wave basis set.[41] The Ag(111) surface was constructed with data obtained from the Materials Project[42] with approximately 25 Å of vacuum added to prevent interaction of periodic unit cells perpendicular to the surface. The square RbI structure was optimized on one layer of Ag (frozen to retain the bulk lattice constant) via the PBE functional for solids (PBE_{sol})[43] at the Γ point and with a 500 eV planewave cutoff until all forces were less than 0.05 eV $Å^{-1}$. All electronic structure calculations were optimized until the change in energy between iterative steps was less than 10^{-6} eV. For the atomic vacancy structures, a 'ribbon' of the square RbI structure was used, which was composed of 5 atomic spacings (Rb-Rb/I-I) along the M_{short} axis and 4 atomic spacings along the M_{long} axis, which resulted in a structure that was continuous along the M_{short} axis and discontinuous along the M_{long} axis with adjacent periodic unit cells

separated by ~1 nm of bare Ag. We found this 'ribbon' structure to be large enough to approximate complete monolayer coverage at the vacancy defect (placed in the middle of the ribbon), while keeping the computational cost low enough so that two additional layers of Ag could be added underneath to accurately model charge transfer interactions at the defect. The change in potential due to RbI-Ag interaction was calculated by subtracting the total potential (composed of ionic and Hartree components) of the isolated RbI/Ag structures from the composite system. Visualizations of all structures were made using the VESTA package.[44]

Simulated STM images were computed using methods described elsewhere.[35] In these simulations, the work function is used to calculate the energy-dependent probability of an electron tunneling between the tip and sample, and is computed as the difference between the average electrostatic potential far from the surface and the Fermi level of the sample. We find that in order to model vacancy-type defects in the RbI monolayer, it is important to consider the local changes in work function due to the presence of the defect, and so the work function of the pristine RbI structure is corrected by the difference in electrostatic potential between the pristine and defect structures such that: $\phi(x,y)_{sample} = E_{vacuum\ level} - E_{Fermi} + E(x,y)_{defect\ structure} - E(x,y)_{pristine\ structure}$.

5.3. Results and Discussion

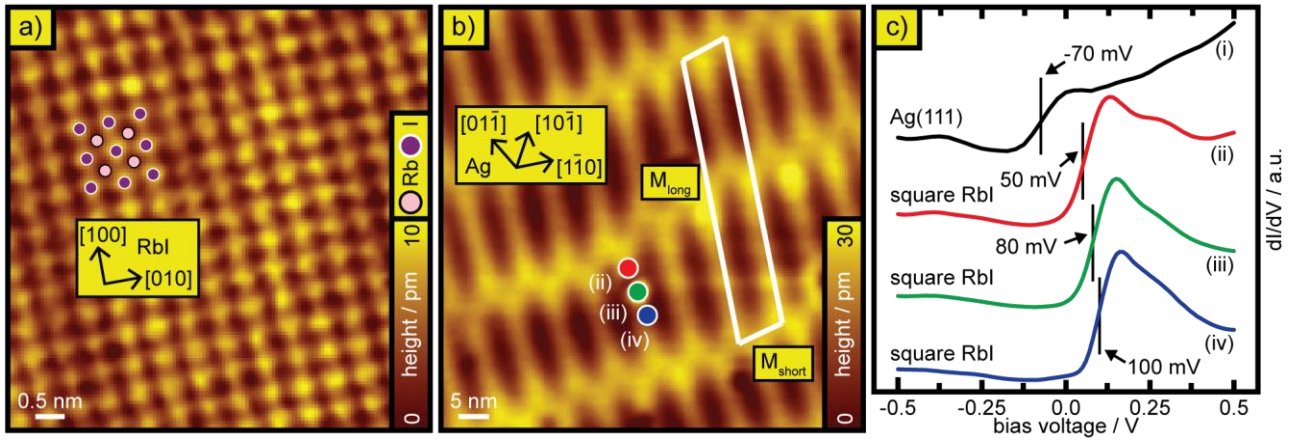

Figure 5.1: STM/STS of square RbI monolayer. a) STM topography (V_b = -200 mV, I = -100 pA) showing atomic resolution on a square RbI monolayer. b) STM topography (V_b = 2 V, I = 10 pA) showing the moiré supercell formed by square RbI/Ag(111). The colored circles indicate the position of representative STS spectra shown in (c). c) STS measurements (V_b = 500 mV, I = 50 pA, V_{pp} = 40 mV) recorded on bare Ag (i) and square RbI (ii – iv), with the vertical lines indicating the band onset energy of the SS/IES.

Here, we use STM/STS to explore the impact of strong metal-insulator interactions on the IES of the RbI/Ag(111) system. STM imaging shows that RbI forms a single-layer structure at sub-monolayer surface coverage (Figure 5.1a,b). This structure has been characterized in detail elsewhere,[35] and we describe it briefly here. In STM topography recorded at low bias voltage (Figure 5.1a) we observe, with atomic resolution, a RbI structure analogous to the (100) plane of the bulk RbI structure. Here, the protrusions in STM topography, which correspond to individual iodine atoms,[35] are coordinated in a 'square – planar' manner ('square' in the following). The square symmetry of this structure is in contrast with the hexagonal symmetry of the Ag(111) surface, and this incommensurability is evident in STM topography recorded at high bias voltage (Figure 5.1b), which shows a moiré pattern with lattice vectors M_{long} and M_{short}. By recording STS spectra on both bare Ag(111) and a square RbI monolayer, we observe that the local density of electronic states (LDOS) near the Fermi level is distinct for different regions in the moiré

supercell (Figure 5.1c). On bare Ag(111), STS spectra are consistent with the expected appearance of the Shockley SS showing a step-like feature with a band onset at approximately -70 mV (curve i in Figure 5.1c). Meanwhile, STS spectra recorded on a square RbI monolayer show an up-shifted band onset (curves ii-iv in Figure 5.1c). The upshift of the LDOS onset energy (relative to the SS) is consistent with previous results for other alkali halides and adsorbate layers, where the upshifted band was associated with IES.[10-16] [Also note that in contrast with previous studies of other alkali halides, the IES band onset energy in the present system varies across the moiré supercell (compare curves ii-iv in Figure 5.1c).]

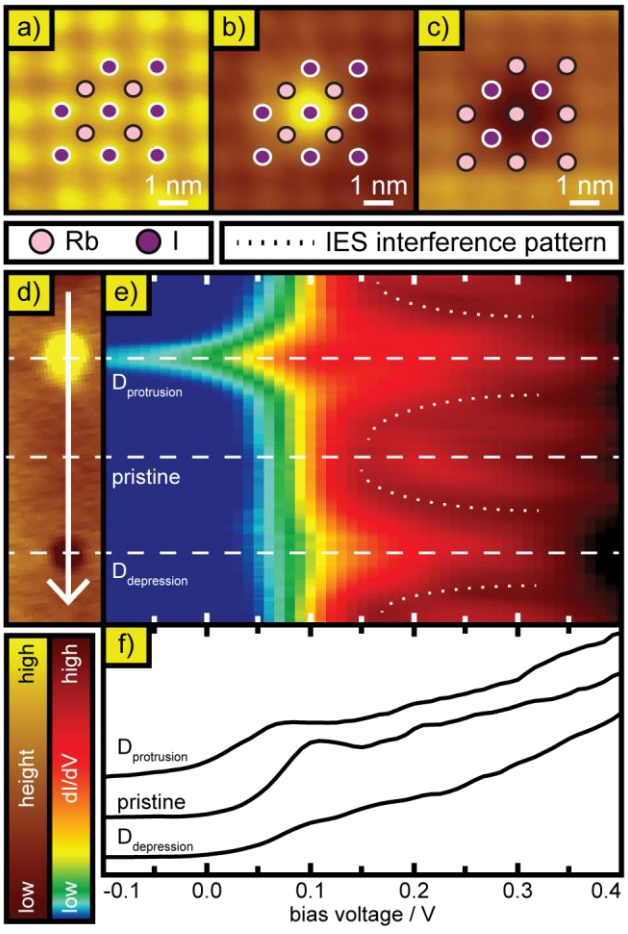

Figure 5.2: Interaction of IES with point defects in RbI monolayer. a-c) STM topography (a: V_b = -10 mV, I = -100 pA; b-c: V_b = -200 mV, I = -100 pA) of pristine RbI monolayer (a) and two common point defects (b,c). The registry of the atomic lattice is overlaid, showing that the protrusion-type defect (b) is centered on an iodine atom and the depression-type defect (c) is

centered on a Rb atom. d,e) STS measurements (e) recorded along a line (shown in (d)) between a protrusion-type defect ($D_{protrusion}$) and a depression-type defect ($D_{depression}$). The curved dotted lines serves as guides to the eye to highlight the interference pattern formed by scattering of the IES. STS parameters are: V_b = 0.5 V, I = 100 pA, V_{pp} = 40 mV. f) Individual STS spectra from (e), to highlight the difference in electronic structure at each defect relative to the pristine structure.

To determine whether the observed upshifted band is indeed an IES, we examine its behavior near point defects, which can be expected to scatter IES, and lead to formation of interference patterns in LDOS. Our STM results show two common kinds of point defects visible as either depressions or protrusions in topographies recorded at low bias voltage. These defects show distinct registry with respect to the atomic lattice (Figures 5.2a-c): the protrusion-type defect ($D_{protrusion}$) is centered on an iodine atom (Figure 5.2b) while the depression-type defect ($D_{depression}$) is centered on an Rb atom (Figure 5.2c). To characterize the spatial behavior of the LDOS at these defects, we have recorded progressions of STS spectra across each defect, with a representative pair of defects shown in Figure 5.2d, for which spectra were measured along a path connecting these two defects. The resulting spectra show interference patterns (Figure 2e), which are the result of constructive/destructive interference of an incident and scattered IES. This finding is in line with previous observations of similar effects for vacancy-type defects in other alkali halides,[10, 12, 14] suggesting that the observed state is indeed an IES and is delocalized in the plane of the surface.

To make further progress in understanding our STS results, we must first identify the two defect types observed here, which we expect to be atomic-vacancy defects due to the distinct alignment of topographic features to the atomic lattice (Figure 5.2b,c) and the presence of similar such defects in previous studies of both monolayer[45] and bilayer[14] NaCl. We begin by simulating STM topographies for several vacancy defects, and find that we can only reproduce the presence of both depression- and protrusion-type defects when the effect of the atomic vacancy on the

local work function is considered (see Appendix, Figures C.1 and C.2 for STM images simulated with/without a spatially-dependent work function). Indeed, in STM topography recorded at low bias voltage, our results suggest that the Rb vacancy appears as a depression due to the absence of an Rb atom and a local increase in work function at the defect, while the iodine vacancy appears as a protrusion due to a local reduction in work function (resulting in increased tunneling current), in agreement with our DFT calculations (see Appendix, Figure C.3). This result is in contrast to previous STM results of halide vacancies, where Cl atomic vacancies resulted in depression-type topographic features in both monolayer[45] and bilayer[14] NaCl, which we interpret as follows: substrate/adlayer interactions are stronger for RbI than for NaCl,[35] resulting in a more significant impact on the local potential for atomic vacancies and necessitating consideration of the local work function in simulation of STM topography. Additionally, Figure 5.2e shows that the IES onset is downshifted at the $D_{protrusion}$ defect, and slightly upshifted at the $D_{depression}$ defect (Figure 5.2f). To understand the origin of these changes in the IES onset energy, we have used DFT to calculate several vacancy structures, which consistently show that the potential associated with these defects is repulsive (attractive) for Rb (iodine) vacancies (Figure 5.3), irrespective of the substrate/adlayer registry (see Appendix, Figure C.3). The resulting potential can be explained by electrostatics: the absence of a positively (negatively) charged Rb (iodine) atom yields a net negatively (positively) charged local electrostatic environment, in line with previous results for both monolayer[45] and bilayer[14] NaCl that found that Cl vacancies resulted in attractive electron potentials. An important insight offered by Figure 5.2 is the apparent sensitivity of the IES to the local electrostatic modulation associated with the RbI layer,[35] which suggests that the moiré pattern in Figure 5.1b may potentially, at least in part, be a consequence of such electrostatic modulation.

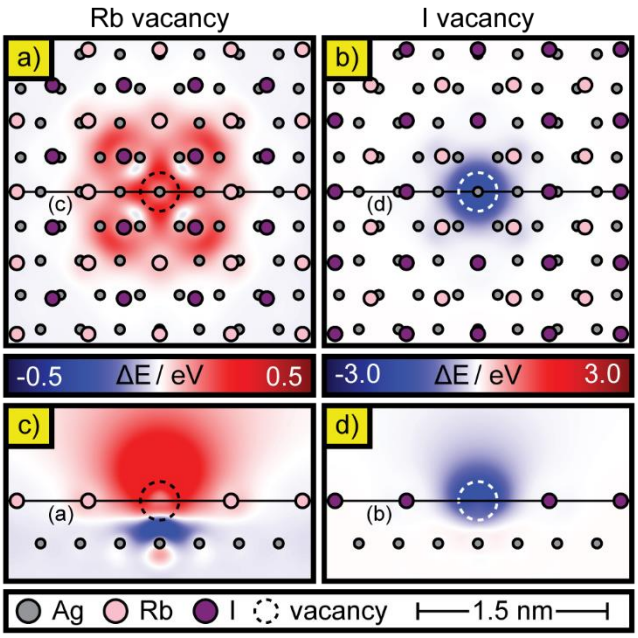

Figure 5.3: DFT-calculated differential electron potentials of vacancy defects in the RbI monolayer. The difference in potential for the defect structure relative to the pristine structure is shown for Rb (a,c) and iodine (b,d) vacancy defects: $\Delta E(r) = E(r)_{defect\ structure} - E(r)_{pristine\ structure}$. a,b) The difference in potential is shown in the plane of the adlayer, where the effect of the vacancy is most significant, as indicated by the difference in potential in the plane orthogonal to the surface (c,d).

To understand the origin of the moiré pattern in the present system, we recorded STS spectra characterizing the overall distribution of IES across the surface (Figure 5.4). Our STS results show that the onset of the IES varies differently along M_{short} and M_{long} axes (compare Figure 5.4b and 5.4d). Specifically, the IES onsets along the M_{short} axis do not vary significantly across the moiré supercell (see, for example, Figure 5.4b where the LDOS onset is at ~100 mV). In contrast, the IES onsets along M_{long}, when measured at a specific location along M_{short}, vary between 50 and 100 mV (Figure 5.4d). In addition to spatial variations in the IES onset, we also observe sets of peaks above the IES onset energy, which are periodic with the moiré lattice vectors. Along the M_{short} axis, we observe sets of peaks at bias voltages of ~300 and ~700 mV. These peaks show contrasting spatial behavior (see difference between i and ii in Figure 5.4c),

and are separated by half of the M_{short} period. Along the M_{long} axis, we observe a set of peaks at biases of ~150 mV that align spatially with the maxima of the IES onset (see cross section iii in Figure 5.4e). Importantly, all LDOS features observed by STS are periodic with the moiré supercell.

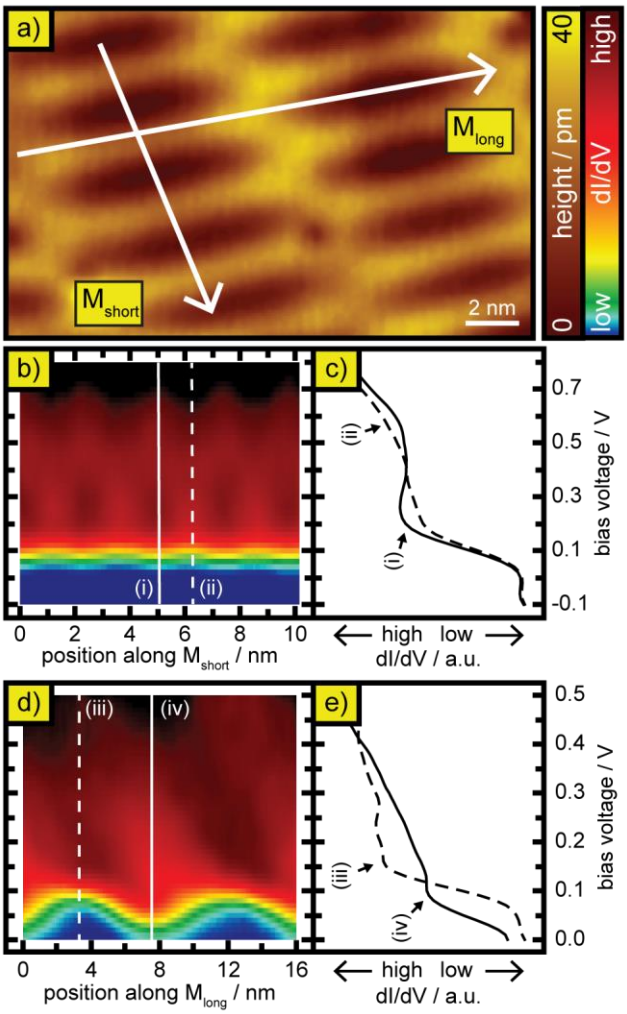

Figure 5.4: Spatial behavior of the Ag(111)/RbI interface state. a) STM topography (V_b = 2 V, I = 10 pA) of a square RbI monolayer, showing the paths along which STS spectra were taken in b,d. b,d) STS spectra taken along the M_{short} (b) and M_{long} (d) axes, corresponding to the paths shown in a. STS parameters are, in b: V_b = 0.8 V, I = 150 pA, V_{pp} = 80 mV, and in d: V_b = 0.5 V, I = 200 pA, V_{pp} = 20 mV. c,e) Comparison of individual STS spectra from b (i,ii) and d (iii,iv)

To understand why the IES varies spatially across the moiré supercell, we first consider the structure of the RbI/Ag(111) interface, which has been described in detail elsewhere.[35] The

⟨100⟩ directions of the square RbI lattice are oriented along the $[1\bar{1}0]$ and $[11\bar{2}]$ directions of the Ag(111) surface. However there is a mismatch in the lattice spacings for RbI and Ag(111), which results in a moiré supercell defined by the lattice vectors M_{long} and M_{short}, having lengths of 2.7 and 15.8 nm, respectively. Due to this incommensurability between square RbI and Ag(111), the coordination of Rb/I atoms to Ag varies across each of the moiré lattice vectors. Previous DFT calculations have shown that the strength of RbI-Ag interaction is determined by the substrate-adlayer registry, which in turn, affects the extent of electron transfer from the adlayer to the substrate.[35] Here, due to the large size of the moire supercell (558 Ag atoms per layer + 300 adlayer atoms), our DFT model is limited to a single layer of Ag, which prevents us from being able to model this system quantitatively. However, on the qualitative level, our calculations for this model suggest that spatial variations in the extent of substrate-adlayer charge transfer lead to the emergence of an effective periodic potential (see Appendix, Figure C.4). Because the parameters of this potential cannot be accurately determined by DFT, we turn to a simpler single-electron model used previously for the NaCl system.[10, 13] In this model, we retain only the long range harmonics of the periodic potential matching the periodicity of the moire pattern, which enables us to construct the IES wavefunctions from the well-known, analytical solutions to the Mathieu equation, where the two-dimensional potential is represented by a sum of two cosine functions (see Appendix).[46, 47]

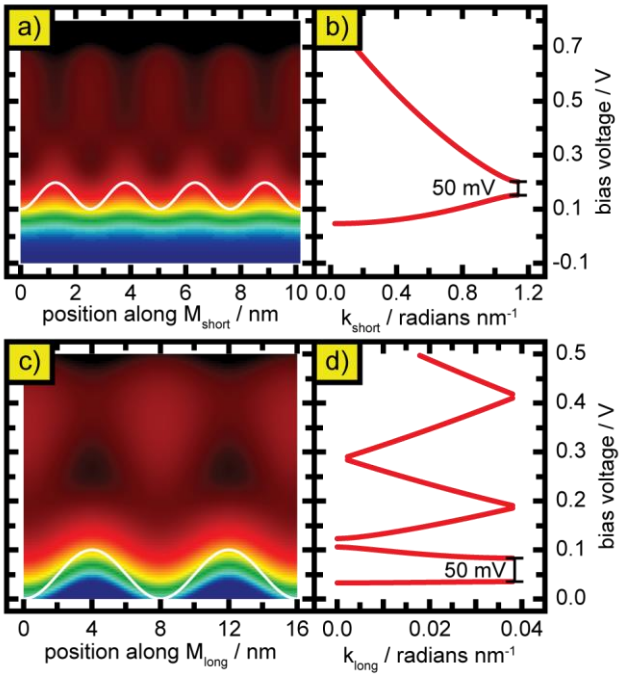

Figure 5.5: LDOS and band structure calculated from Mathieu equation. a,c) LDOS of 2D Mathieu eigenstates along the M_{short} (a) and M_{long} (c) axes, with the cosine potential (100 mV peak-to-peak along each axis) used to calculate the LDOS overlaid. At each position, the LDOS is normalized to the sum of the LDOS, analogous to the constant-current method by which our STS measurements were acquired. Gaussian smearing is applied to model the effect of a finitely sized tip (horizontal axis) and energy broadening (vertical axis). b,d) Band structure for the M_{short} (b) and M_{long} (d) moiré axis, with the band gap between the first two bands indicated.

To qualitatively model the IES wavefunctions, we solve the Mathieu equation for each moiré axis independently, with the spatial periodicity of the potential determined from the moiré lattice vectors, and the potential amplitude determined by fitting to the LDOS found in experiment (Figure 5.4). We find that the calculated LDOS distributions (Figure 5.5) give the best fit to the experimental data when the potential amplitude along each axis is ~50 mV. (One notable discrepancy is that in our calculations, the peaks along M_{long} appear symmetric with respect to a mirror plane orthogonal to M_{long}, whereas in experiment the moiré pattern is asymmetric due to the underlying structural asymmetry of the RbI/Ag(111) interface.) The results shown in Figure 5.5 allow us to identify the origin of STS features in Figure 5.4.

Specifically, for the M_{short} axis, the set of peaks at ~300 mV are located within potential wells, whereas peaks at ~700 mV are centered above maxima in the potential (Figure 5.5a), between which lies a band gap of 50 mV (Figure 5.5b). This suggests that the 300 mV and 700 mV LDOS peaks observed along the M_{short} axis are of different origin: states with energy less than the potential maxima are confined within the potential well, whereas states with energies above the potential maxima are delocalized states that 'slow down' (in the quasi-classical sense) and have a high probability density near the potential maxima. A similar picture is observed along the M_{long} axis (Figure 5.5d), where the energy scale is compressed in the vertical direction due to the smaller quantization energy resulting from a longer localization length of the wavefunction. Our results agree with previous interpretations of similar STS measurements for bilayer NaCl moiré patterns, where the LDOS of bands below (above) the first band gap were found to be out-of-phase (in-phase) with the periodic potential.[10, 13] Furthermore, the formation of an anisotropic band gap is consistent with previous work on bilayer NaCl/Cu(111), which showed the IES band gap was related to the spatial periodicity of the moiré pattern.[13] An interesting distinction between this work and that reported previously for NaCl lies in the dimensionality of the potential. Work on the NaCl/Ag(111) system has shown that the spatial behavior of the LDOS can be explained by considering a 2D electron gas in a 1D potential, where limited spatial phase coherence leads to the observed LDOS contrast for bands above/below the first band gap, and a constant band onset is observed.[10] Here, we show that LDOS contrast arises in a 2D potential, which can be modeled via its linearly independent components, and results in significantly stronger spatial modulation of the LDOS onset, as well as LDOS well above the band gap. Another notable distinction between the two systems is that the potential amplitude for RbI/Ag(111) is larger than that for bilayer NaCl/Ag(111) [50 mV vs 30 mV] resulting in an

increased band gap.[10] This finding is consistent with our expectation [based on DFT results for adsorption of RbI and NaCl molecules on Ag(111)[35]] that the substrate-adlayer interaction in RbI/Ag(111) is stronger than that in NaCl/Ag(111), although we also expect that the presence of additional overlayers in the bilayer NaCl study[10] would reduce the impact of substrate-adlayer interactions relative to the single-layer case observed here. Further support for this view is provided by the fact that NaCl islands adopted several different substrate/adlayer registries in previous work,[10, 13] whereas the strong interactions of RbI favor only a single registry in our experiment.

An interesting consequence of the anisotropy in the found model potential is the pronounced anisotropy in the 2D band structure of the IES (Figures 5.5b and 5.5d). This anisotropy can be quantified by focusing on the effective electron mass along the M_{long} and M_{short} axes, which, for the lowest energy states in Figure 5.5b and 5.5d (see Appendix, Figure C.5) are 1.06 and 0.41 m_e respectively, larger than that of the SS for bare Ag(111) [0.4 m_e].[48] Since the amplitudes of the potential along each moiré axis are the same in our model (100 mV peak-to-peak), this anisotropy of the effective electron mass arises from the relative magnitudes of the lattice vectors, where the longer (shorter) length of M_{long} (M_{short}) leads to a smaller (larger) zero-point energy and, consequently, a larger (smaller) effective potential barrier between individual wells, leading, in turn, to a flatter (steeper) band structure (compare Figures 5.5b and 5.5d). The significance of this result is apparent in the context of previous results for NaCl on Ag(111), where a single, isotropic effective electron mass was reported.[10, 11] While the effective electron mass reported for a bilayer of NaCl on Ag(111) is heavier than that for the SS of bare Ag(111),[10, 11] in line with our results, the average increase in effective mass for RbI is more pronounced, a consequence of the larger strength of interaction between the adlayer and substrate leading to a

more strongly corrugated potential.[10] We find that this more corrugated potential for RbI makes it difficult to calculate the effective electron mass from experimental data, possibly due to more rapid dephasing of the scattered IES, in contrast to previous work on NaCl where the IES momentum could be calculated from two-dimensional fast Fourier transforms of STS images.

5.4 Conclusions

To summarize, we have identified and characterized two distinct single-layer structures of RbI, which are structurally different from that of the bulk crystal. We show that the prevalence of a particular phase is determined by the local structure of the Ag surface: the square RbI structure is better matched to the Ag step edges, whereas the hexagonal RbI structure is commensurate with the Ag(111) atomic structure. The Ag-RbI interface is energetically more favorable than an interface between RbI layers, which results in the dominance of the (denser) square phase at higher RbI surface coverages. Both phases exhibit non-trivial contrast in STM images, with apparent heights of individual atoms determined by their local coordination to the Ag surface. We hope that the simplicity of the presented physical picture may lend itself to qualitative understanding of other heterostructures involving ionic and metallic layers.

5.5 Bridge to Chapter VI

We have thus far shown that coupling between a substrate and dielectric layer can impact the electronic structure of the adlayer. In the following chapter, we extend this discussion to include the effect of coupling on carbon nanotube adsorbates. We explore how carbon nanotubes interact with the electrostatic environment that arises due to substrate-adlayer coupling. As a

promising alternative to Si as a transistor channel material, this study offers insight on the coupling between carbon nanotubes and the electrostatic environments within which they reside.

CHAPTER VI

IMPACT OF EXTERNAL ELECTRONIC PERTURBATIONS ON SINGLE-WALLED CARBON NANOTUBE ELECTRONIC STRUCTURE: SCANNING TUNNELING SPECTROSCOPY AND DENSITY FUNCTIONAL THEORY

From Taber, B. N.; McDowell, B. W.; Mills, J. M.; Gervasi, C. F.; Nazin, G. V. Impact of External Electronic Perturbations on Single-Walled Carbon Nanotube Electronic Structure: Scanning Tunneling Spectroscopy and Density Functional Theory. *J. Phys. Chem. C* **2023**, *127* (9), 4651– 4659,

6.1. Introduction

Single-walled carbon nanotubes (CNTs) exhibit many remarkable properties[1-4] and can be used in a myriad of applications.[5] CNTs have demonstrated a high degree of tensile strength,[6] high thermal conductivity,[7] and ballistic charge carrier transport.[8] CNTs can be used as gas,[9, 10] biological,[11] and chemical[12] sensors. CNTs can also be used in microelectronics[13-15] and optoelectronics,[16] are a promising post-Si transistor channel material,[17, 18] and have applications in energy storage and release.[5, 19-22] The local electronic structure of CNTs and therefore device performance, however, is highly sensitive to environmental inhomogeneities.[4, 10, 23] While this sensitivity can be advantageous, as the electronic structure of CNTs can be readily altered by electrostatic doping,[24, 25] many devices incorporating defect-free CNTs perform over an order-of-magnitude worse than their theoretical capability due to interactions between the CNTs and defects in both the gate dielectrics and metal contacts.[26-28] Charged defects in the gate oxide of a CNT-channel transistor can cause random-telegraph-signal noise,[26, 27] and contact with a metal surface

can generate localized states.[29, 30] In this study we hope to gain a better understanding of the role of environmental factors in device performance by investigating the effect of a disordered electrostatic environment on the electronic structure of CNTs.

While charged defects or dipoles in the dielectric of a CNT-based transistor can significantly reduce device performance,[26, 27] the nanoscale impact of these defects on CNT local density of states (LDOS) is poorly understood, however, understanding modifications of CNT LDOS by electrostatic perturbations is essential for future applications. Though bulk experimental techniques are unable to spatially resolve these nanoscale interactions, scanning tunneling microscopy (STM) can measure both the physical structure and LDOS of nanomaterials with atomic resolution.[31] Here, we use STM and scanning tunneling spectroscopy (STS) to investigate the local electronic structure of CNTs subject to a range of electrostatic interactions arising from charged defects or dipoles adjacent to the CNT. In these STS studies, modulation in the Au(111) reconstructed surface serves as a model for strong electrostatic interactions, and monolayer RbI serves as a model for weaker electrostatic interactions, due to the higher polarizability of the dielectric.

6.2. Methods

Experiments were carried out in a home-built ultrahigh vacuum (UHV) cryogenic STM system.[32] All imaging and spectroscopic measurements were carried out at ~26 K using electrochemically etched silver tips. A 200 nm of Au(111) on mica substrate was prepared in situ by using multiple neon sputter/anneal cycles. A ~half-monolayer of RbI was deposited on to the Au surface (held at room temperature) via in situ sublimation in UHV conditions. CNTs (obtained

from Sigma-Aldrich, >95% carbon as CNTs) were deposited onto the RbI/Au(111) substrate using the in-vacuum dry contact transfer method.[33]

Approximately 10 nm-long, hydrogen-terminated, (6,5) and (7,6) CNTs were constructed using Avogadro,[34] then geometry-optimized with B3LYP[35] or CAM-B3LYP[36] and STO-3G[37] in Gaussian (g09E01).[38] A charge pair (dipole) was then added (inter-charge distance of 3.67 Å, chosen to be representative of the RbI interatomic distance), and the electronic structure was assessed with the same functional and basis set as was used for the geometry optimization. Unconstrained optimization in the presence of a dipole offered poor convergence and was successfully mitigated by fully constraining all atoms within 1 Å of the plane perpendicular to the dipole charge pair. LDOS results were then analyzed with MultiWfn.[39] For LDOS plots, a FWHM of 100 meV in energy and 3 Å in space was applied to the DFT results, the same FWHM that replicated experimental STS mapping of oligothiophenes in one[40] and two[41] spatial dimensions.

6.3. Results and Discussion

CNT LDOS modulation by Au(111) 22√3 surface reconstruction

The Au(111) surface serves as a model for strong electrostatic interactions, as well as a model (such as the source/drain for a CNT channel transistor) electrode for CNT-based devices. We prepared an atomically clean Au(111) substrate in ultra-high vacuum, and deposited CNTs using the in-vacuum dry contact transfer method.[33] We then used a home-built STM[32] [See Methods for further details] to image CNTs on the Au(111) reconstructed surface. In vacuum, the Au(111) surface adopts the $22\sqrt{3}$ surface reconstruction,[42-44] generating a corrugated surface with "ridges" parallel to the <112> direction that separate face-centered-cubic (fcc) and hexagonal-

close-packed (hcp) structures. The CNTs adsorbed along several Au(111) lattice directions, and STS of CNTs adsorbed along the <110> direction (perpendicular to the surface reconstruction ridges) revealed periodic modulation of the LDOS, as previously observed by Kawai and coworkers.[28]

Figure 1a shows a representative example of a CNT adsorbed roughly perpendicular to the Au(111) surface reconstruction ridges. The ridges along the <112> direction in Figure 6.1a continue under the CNT, suggesting that the CNT is adsorbed across multiple fcc and hcp regions of the Au(111) surface, and therefore experiences periodic changes in CNT-surface separation.[28] Indeed, one (spatial) dimensional LDOS mapping along the CNT (Figure 6.1b) showed modulations in both the occupied (valence) and unoccupied (conduction) LDOS of the CNT correlated with the underlying Au(111) surface reconstruction ridges, indicated by the white dashed lines in Figure 6.1b. We assign regions of the CNT that adsorbed on fcc and hcp regions in Figure 6.1b based on the observed Au(111) surface reconstruction below the CNT in Figure 6.1a. Figure 6.1b also reveals a pair of spatially co-localized mid-gap states, likely caused by a Stone-Wales-like carbon coordination defect[3, 45, 46] (indicated by an x in Figure 6.1a). Though carbon coordination defects are not the focus of this work, states D_H and D_E in Figure 6.1b are asymmetrically located about the Fermi level at ~-200 mV and ~400 mV, respectively, as Shigekawa and coworkers previously observed on Stone-Wales-like defects in CNTs adsorbed on Au(111).[47]

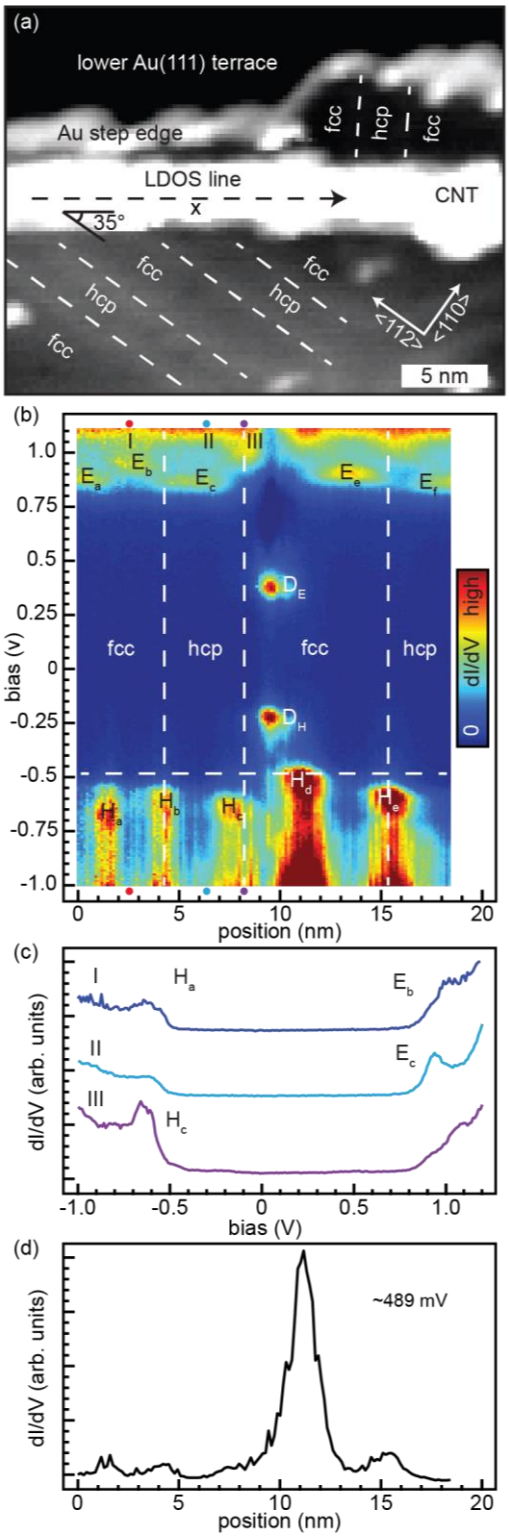

Figure 6.1. Modulation of CNT LDOS correlated with the Au(111) $22\sqrt{3}$ surface reconstruction. (a) STM image of a semiconducting CNT on Au(111), with surface reconstruction ridges highlighted by dashed lines and the location of a Stone-Wales-like defect indicated by an "x". Note that there is carbon detritus decorating the Au(111) step edge. (b)

dI/dV line scan of the CNT along the black dashed line in (a) with dashed white lines separating fcc and hcp regions of the surface reconstruction. (c) Vertical slices of positions along the CNT indicated by corresponding colored dots (the endpoints of the LDOS cross-section) and labels (I,II,III). (d) Cross-section of constant STM bias (0.489 V) indicated by the horizontal dashed line in 2b showing spatial extent of state H_d. Set points (a) 1 V, 5 pA and (b,c,d) 1.2 V, 25 pA, 10 mV oscillation amplitude.

While the lowest unoccupied molecular orbital (LUMO) states are further from the Fermi level (assumed to be 0 V) than the highest occupied molecular orbital (HOMO) states, as previously observed with STM in CNTs on Au(111),[48] there are some slight energetic differences among the localized states, such as E_e, adsorbed on the fcc region, which is ~50 meV higher than E_f, adsorbed on the hcp region. This difference could be due to the differing surface reactivity of the fcc versus hcp regions,[49] which leads to the fcc region being the preferred adsorption site for small molecules.[50-52] Differing surface reactivities are unlikely to be the main source of energetic differences between LUMO states, however, as while E_a and E_b are both in the fcc region, their LUMOs are separated by ~100 mV, suggesting that slight energetic differences may be due to modulations in charge transfer between the CNT and Au(111), as Kawai and colleagues found in the case of a CNT adsorbed along a Au(111) step edge.[28]

High-intensity regions in the CNT LDOS alternate in spatial extent between the occupied (H_a, H_b, H_c, and H_e) and unoccupied sides (E_a, E_b, E_c, E_e, and E_f). Maxima in H_b, H_c, and H_e dI/dV intensity are localized on the Au(111) surface reconstruction ridges separating the fcc and hcp regions, and H_a and H_d are located in the center of the fcc regions. The high-intensity areas of E_c and E_f, however, are localized between the ridges in the center of the hcp Au(111) surfaces, and E_a, E_b, and E_e are localized within fcc regions. Localization of E_b and E_c in the fcc and hcp regions respectively are shown in Figure 6.1c. That the highest HOMO states and lowest LUMO states are not co-localized is indicative of band bending by periodic doping, as was observed by STM in

CNTs on Ag(100),[53] and a previous STM investigation suggested that CNT occupied state localization on the Au(111) surface reconstruction ridges is a result of modified charge transfer at this interface, likely due to closer proximity of the Au surface to the CNT in these locations.[28]

The band bending observed in Figure 6.1b can be attributed to charge transfer between the Au(111) surface and the CNT, which is due to the mismatch in the effective work-functions (WFs) between the two.[48] The WF of CNTs, as measured by photoemission, is $WF_{CNT} = 4.8$ eV.[54] This is smaller than that of a pristine Au(111) surface ($WF_{Au} = 5.33$ eV),[55] though the effective WF of the Au(111) surface is likely reduced by the nearby Au step edge and its associated WF-lowering charge redistribution caused by the Smoluchowski effect.[56] The adsorption-induced charge transfer between the CNT and Au(111) due to WF mismatch rearranges the electron distribution, resulting in an interface dipole layer that shifts the vacuum level and causes localized band bending.[57]

The raised surface reconstruction ridges reduce the CNT-substrate distance, leading to higher electron injection from the CNT to the Au. This lowers the interface dipoles[58] at the ridge/CNT interface, inducing the observed periodic LDOS oscillations.[28] In addition to charge-transfer, the interface dipole can also include short-range interactions resulting from the overlap of the wave functions of the CNT and metal.[58, 59] Strong electrostatic interactions arising from variations in charge transfer between a CNT and metal surface lead to the localized states, as observed in Figure 6.1b, which can act as charge trap sites. The CNT local electronic structure, however, is not only impacted by electrostatic interactions resulting from varied charge-transfer with metal surfaces.

CNT density of states modulation by dielectric defects

Environmental electrostatic defects, including dipoles, can also exist within insulators, such as the gate dielectric of a CNT-channel transistor, thereby degrading CNT-based device performance.[26, 60] To study the impact of electrostatic interactions arising from dielectrics on the CNT LDOS, we deposited CNTs on Au(111) covered by approximately a half-monolayer of RbI, which has previously been used as a dielectric in STM studies on Cu(111).[61] On the Au(111) surface, the RbI formed crystal islands of varied sizes (from a few nm to tens of nm) with an apparent band gap of ~6.2 eV, slightly larger than that of bulk RbI.[62] The apparent bandgap measured with STS is typically greater than actual due to coulombic effects, suggesting that there may be a possible band gap decrease due to the monolayer nature of the RbI, resulting in an apparent band gap similar to the bulk. We investigated several CNTs adsorbed on both RbI and Au(111) (such as in Figure 6.1), but here we focus on a CNT adsorbed across both the middle and edge of a monolayer RbI crystal (Figure 6.2).

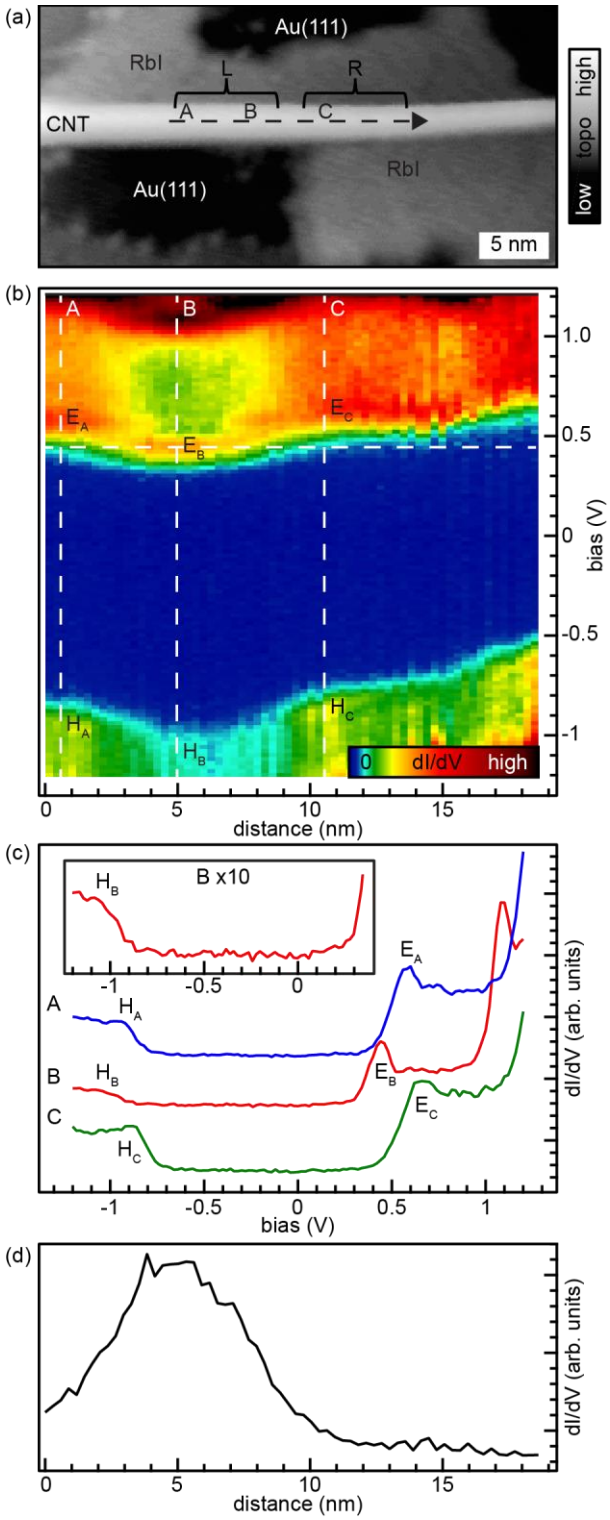

Figure 6.2. STS of a CNT on monolayer RbI. (a) STM topography of a CNT adsorbed on a RbI monoalyer on a Au(111) substrate (1 V, 2 pA set point), with region "L" corresponding to where the CNT is at the edge of the RbI island, and region "R" corresponding to where the CNT is adsorbed in the middle of a RbI island. (b) STS line scan along the dashed line in Figure 2a. (c) STS single-point spectra at the points indicated by the letters in 2a and vertical dashed lines in

2b. Curve B's occupied states are magnified for clarity in the inset. Labled peaks correspond to those labled in 2b. STS spectra 1.2 V, 10 pA set point, 20 mV oscillation amplitude. (d) Cross-section of constant STM bias (0.44 V) indicated by the horizontal dashed line in 2b showing spatial extent of state E_B.

The left side of Figure 2a shows a CNT adsorbed along a boundary between bare Au(111) and a monolayer of RbI, while the right side of Figure 6.2a reveals that the CNT is adsorbed on top of the RbI layer. Because there are no significant changes in height of the CNT in Figure 6.2a throughout the STM image, the CNT is likely adsorbed on top of the same RbI monolayer on both sides of Figure 6.2a, thereby allowing comparison of the CNT when adsorbed near a RbI crystal edge (labeled "L" in Figure 6.2a) and on a larger part of the RbI crystal (labeled "R" in Figure 6.2a).

As in Figure 6.1b, in Figure 6.2b we used a one (spatial) dimensional STS line scan along the CNT to probe the CNT LDOS along the dashed line in Figure 6.2a. The CNT band gap appears fairly consistent throughout the line scan, though there is some band-bending. There is a downshift of greater than 100 mV in the conduction band in part of section "L", labeled E_B in Figure 6.2b, as compared to E_A and E_C, with a similar downshift in H_B in the valence band, as compared to H_A and H_C. To further elucidate this localized band-bending, we examine single-point STS spectra in the middle and on either side of this feature (Figure 6.2c).

In Figure 6.2c, spectra A corresponds to a point in section "L" of the CNT and has a HOMO at -.96 V and a LUMO at 0.56 V, for an apparent band gap of 1.52 V. Spectra C, located in section "R" of the CNT, has similar frontier orbital energies as A and a slightly smaller apparent band gap (1.46 V), likely due to the higher polarizability of the underlying RbI in section "R" resulting from the greater amount of dielectric material as opposed to section "L."

The energetic differences of ~60 mV between spectra A and C likely result from a difference in the bias voltage drops,[30] suggesting similar (defect-free) CNT adsorption environments.

Interestingly, Figure 6.2b reveals a new state, E_B, that is localized over ~5 nm in section "L" of the CNT (Figure 6.2d). While the apparent band gap measured in location B matched that in location A, likely because E_B is localized entirely on part "L" of the CNT, both the HOMO (-1.08 V) and LUMO (0.44 V) were 120 mV lower in spectra B than in A, corresponding to being more than 150 mV lower than in spectra C. There are also no mid-gap states in Figure 6.2b, nor are there protuberances in the CNT topography in Figure 6.2a, suggesting that the spectrum observed in location B is not due to carbon coordination defects, as was the case for the mid-gap states in Figure 6.1b.

In Figure 6.1a and in Figure 6.2b, changing electrostatic potentials along the CNTs are likely bending both the conduction and valence bands and creating new, localized states. Previous STM studies of CNTs on metal surfaces found band bending due to electrostatic interactions,[28-30, 48] and electrostatic interactions from neighboring dielectrics are also expected to impact CNT electronic structure.[18, 24, 27, 63] In order to qualitatively compare our STS results to a range of electrostatic interactions, we use density functional theory (DFT) to investigate a model system of a CNT in the presence of an external dipole.

It is noteworthy here that the electronic band gap in Figure 6.2b is nearly constant along the nanotube even though one could expect a bandgap modulation due to the dissimilar screening (Au vs RbI) of the electron-electron interaction effects that have the potential to modulate CNT band gaps. [63] We attribute the observed lack of band gap variation to the relatively high polarizability and small thickness of RbI in this experiment, which results in screening that is relatively similar to that of the Au substrate. In the following, we thus assume a homogenous

dielectric environment for simulated CNTs, and focus on the impact of external electrostatic potential on the CNT band structure.

Density functional theory of CNTs

For our DFT calculations, we chose semiconducting CNTs with chiralities of (6,5) and (7,6), which have chiral angles of 27.0° and 27.5° and diameters of 0.76 and 0.90 nm, respectively.[66] These chiralities have relatively large unit cells of ~4 nm in the axial direction, and while there are edge effects in calculations of finite-length CNTs, our CNTs have sufficiently large aspect ratios (> 11) to be representative of longer CNTs.[67-70] Prior calculations of CNT band gaps found better agreement with experiment using B3LYP than LDA and PBE,[71] and B3LYP and its derivatives are common functionals used in calculations of organic systems.[72-75] B3LYP,[35] however, excessively delocalizes wavefunctions due to its small fraction of orbital exchange,[76] though this is corrected by CAM-B3LYP,[36] which at short range behaves like B3LYP (20% of orbital exchange), while at long range has more orbital exchange (65%). Though STO-3G is a minimal basis set,[77] CNT calculations with STO-3G can be in good agreement with experiment[78, 79] and save computational cost in large DFT calculations such as the ones in this paper (~1000 atoms).

Therefore, we optimized the CNT geometry using both B3LYP/STO-3G and CAM-B3LYP/STO-3G (hereafter "B3LYP" and "CAM", respectively) for both (6,5) and (7,6). The calculated (6,5) CNT HOMO energy at the CAM (B3LYP) level of theory with was -3.473 eV (-2.855 eV), with a LUMO of -0.513 eV (-1.180 eV), and the calculated (7,6) CNT HOMO energy at the CAM (B3LYP) level of theory with was -3.322 eV (-2.774 eV), with a LUMO of -0.730 eV (-1.318 eV). This results in larger band gaps than the ~1.3 eV expected from optical measurements

on longer semiconducting CNTs[80] due to the optical transition band gap being reduced by the value of the exciton binding energy,[64,81] but matches previous DFT calculations of the same CNT chiralities and lengths at the same level of theory.[69] In all cases present in the main text, geometry optimization was performed in the absence of a dipole as optimization in the presence of a dipole yielded minor changes to the frontier molecular orbitals (MOs) and LDOS. The most significant changes were in the calculated LDOS of localized states, which predicted less localization for structures optimized in the presence of a dipole. A comparison of electronic structure results for CNT structures optimized with and without the presence of a dipole is in the Appendix (Figures D.1-D.2).

CNT frontier molecular orbitals in the presences of an external charge pair

After optimizing the CNT geometry, we added a pair of charges localized at points (either +/- or -/+, maintaining global charge neutrality) perpendicular to the CNT along the y-axis as shown in Figure 6.3a and b, generating a dipole. We varied the distance from the CNT edge to the nearest charge from 1 to 10 Å, while maintaining a constant inter-charge distance of 3.67 Å (the bulk RbI interatomic distance[82]), covering a range of electric potentials. This allows us to compare the spatial extent and energies of the localized states in our experimental results of CNTs adsorbed in strongly (on Au(111), Figure 6.1) and weakly (on RbI, Figure 6.2) interacting environments to the simplified case of a CNT subject to an electric potential due to an external dipole.

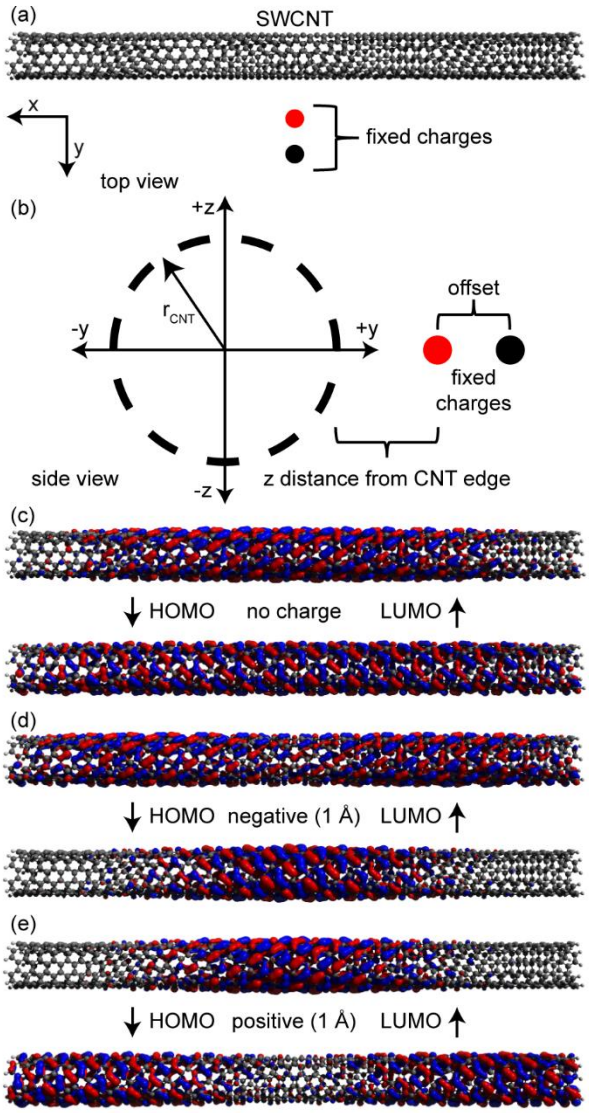

Figure 6.3. Schematics of CNTs with charge pairs reflective of the arrangements explored in this work. Red and black circles refer to either positive or negative charges (one of each per pair) 3.67 Å apart. (a) Top view of a 10 nm-long (6,5) CNT with a single charge pair located in line with the middle of the CNT. (b) Side view of a CNT with a single charge pair located in line with the middle of the CNT. Frontier molecular orbitals of a (6,5) CNT with (c) no external charges, (d) an external charge pair as shown in 1b with the negative charge 1 Å from the CNT edge, and (e) an external charge pair as shown in 1b with the positive charge 1 Å from the CNT edge. DFT geometries optimized with CAM-B3LYP/STO-3G.

With no external dipole (Figure 6.3c), the LUMO was localized near the center of the CNT, while the HOMO was delocalized across the nanotube. The LUMO+1 and HOMO-1 are nearly degenerate (within 10 meV) with the LUMO and HOMO, respectively, and show the same

localization (see Appendix, Figure D.3), and the frontier molecular orbitals (MOs) in the center of the CNT have a similar structure to that calculated for graphene.[83] In the presence of an external charge pair, the localization of the frontier MOs changes. In the case of the negative charge being closest to the CNT (Figure 6.3d), the LUMO delocalizes across the entire CNT, while the HOMO localizes in the central part of the nanotube. This stands in contrast to the case when the positive charge is closest to the CNT (Figure 6.3e), where the LUMO localized in the center of the CNT with more localization than in the case with no external charges (Figure 6.3c). This is similar to the HOMO in Figure 6.3e, where the MO is more localized on either end of the CNT than in Figure 6.3c. This modification of frontier MO localization holds true across both CNT chiralities and DFT functionals investigated in this article (see Appendix, Figures D.4-D.6).

Dependence of CNT LDOS on dipole distance

In order to further compare the impact of the charge pairs on the CNT electronic structure to our STS studies, we examine the LDOS along the central axis of a (6,5) CNT (see Figure 6.4a) for both dipole orientations as a function of dipole-CNT distance. In the absence of external charges (Figures 6.4b and S10), the conduction and valence bands are both delocalized across the central ~6 nm of the CNT. When the negative (positive) charge of the external dipole is 4 Å from the CNT edge (Figure 6.4c,e), the LDOS corresponding to the conduction and valence bands both locally bend upwards (downwards) near 0 nm (the axial coordinate of CNT). When the positive (negative) charge pair is 1 Å from the CNT edge (Figure 6.4d,f) there is a significant upshift (downshift) in both the valence and conduction bands near 0 nm as well as the appearance of new, localized HOMO (LUMO) states. We observed a similar pattern of localized band bending in the LDOS calculated using the B3LYP functional (Appendix, Figure D.12), as well as in the (7,6)

CNT (Appendix, Figures D.13 and D.14), and is similar to LDOS modification due to localized charge transfer in semiconducting CNTs observed with scanning tunneling spectropy.[30]

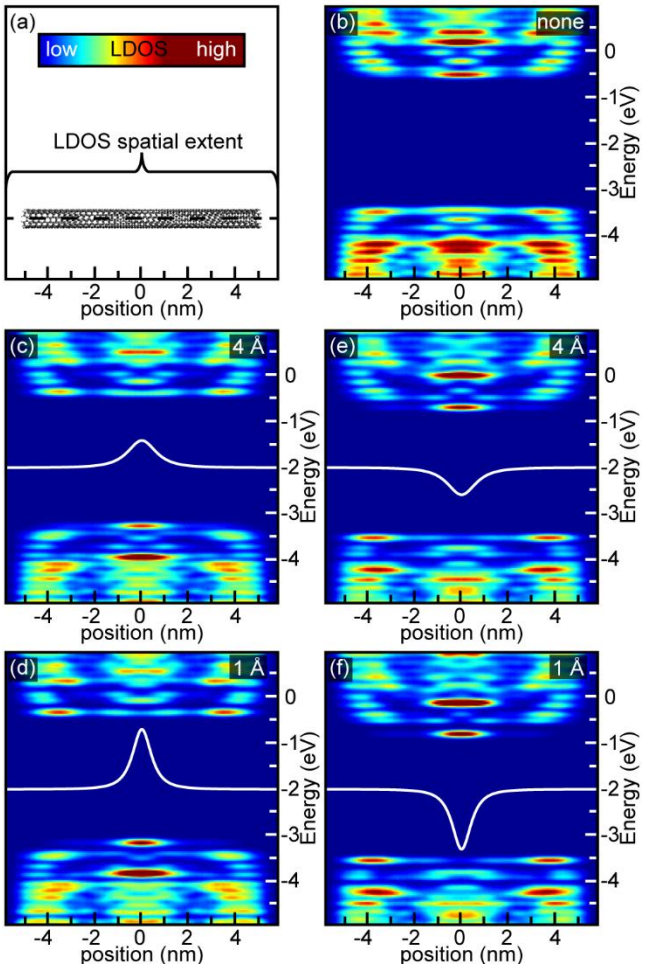

Figure 6.4. LDOS along the center of a 10 nm-long (6,5) CNT with external dipoles of varying distances, as described in Figure 1. The band gap is in the middle of each plot around -2 eV. (a) LDOS of states through the central axis of the CNT as indicated by the dashed line. (b) LDOS of CNT with no external charges. (c,d) LDOS maps with the negative charge pair nearest to the CNT, at the distance (indicated on plots) of (c) 4 Å, and (e) 1 Å from the CNT edge, along with the electric potential energy (white line, offset by -2 eV) of an electron along the central axis of the CNT due to the external dipole. (e-f) same as (c-d) but with the positive charge nearest the CNT. LDOS calculated using CAM-B3LYP/STO-3G, with FWHM of 100 meV and 3 Å.

The LDOS localization is spatially correlated with the electric potential due to the dipole, indicated by the white overlaid curves in Figures 6.4c-f and D.11-14. The potential of an electric dipole is the superposition of the point charge potentials of the negative and positive charges,

$V_{dip} = kq[\frac{1}{r_+} - \frac{1}{r_-}]$, where k is Coulomb's constant and q is the elementary charge, and thus decreases with approximately the inverse of the distance from the dipole, leading to the observed localization. As expected for a semiconductor in the presence of a varying potential, an increase (decrease) of the potential corresponds to local downwards (upwards) band-bending.

The localized band-bending observed in Figure 6.4f is very similar to the case of a CNT in Figure 6.2. As in Figure 6.2b, Figure 4f shows a local decrease in the conduction and valence bands of more than 100 meV. In addition, Figure 6.2b shows local decrease in intensity of the valence band, as evidenced by the lower peak height of H_B in Figure 6.2c. This local decrease in the valence band is also captured in Figure 6.4f, suggesting that the origin of this LDOS feature in Figure 6.2b is due to an electrostatic field, as generated by the external dipole in our DFT calculations.

Perturbation of frontier orbital energies by a dipole

Figure 6.5 displays the impact of dipole distance on the molecular orbital energy, where having the negative charge closest to the CNT increases the HOMO energy and a positive charge decreases the HOMO—with the effects diminishing as the charges move away from the CNT—as expected based for a semiconductor in the presence of a static electric potential. Interestingly, for both (6,5) and (7,6) CNTs (Figures 6.5 and S7), when the dipole is close to the CNT the negative charge has a greater impact on HOMO energy than the positive charge, a result that was repeated when using the B3LYP functional for both chiralities (Appendix, Figures D.8 and D.9). The LUMO energy (Figures 6.5 and D.7-D.9), however, is affected more when the positive charge is closer than the case of the negative charge, though as with the HOMO the negative (positive) charge increases (decreases) the LUMO energy. The frontier orbital changes are not symmetric

between the two dipole orientations, as CNTs with the negative charge nearest had higher band gaps (Figure 6.5) than the corresponding positive charge's, a result consistent across both CNT chiralities and DFT functionals explored here.

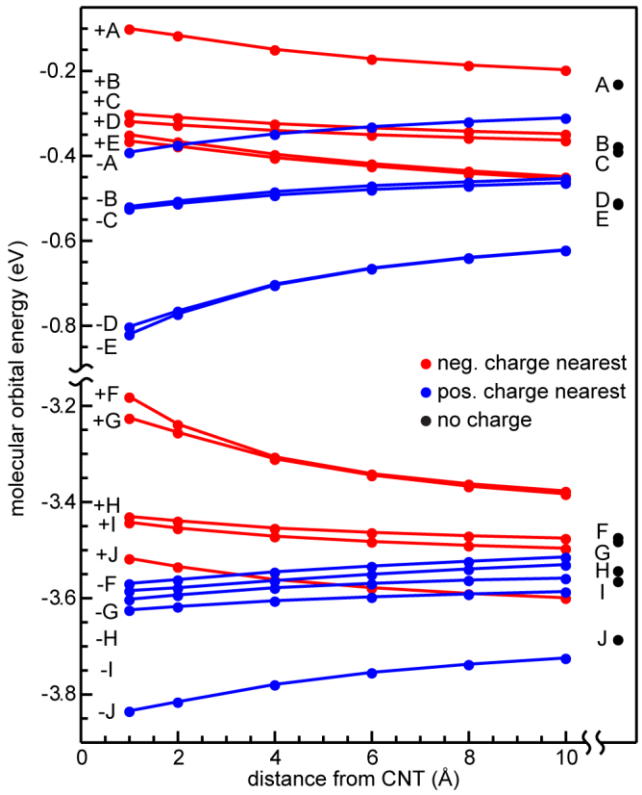

Figure 6.5. Calculated molecular orbital energies for the five highest occupied and five lowest unoccupied MOs of a 10 nm-long (6,5) CNT in the presence and absence of an external dipole. DFT electronic structure calculated using CAM-B3LYP/STO-3G. Letter pairs couple corresponding molecular orbitals, while the preceding signs indicate the sign of the charge closest to the CNT surface.

The interface dipoles discussed above for the case of the CNT adsorbed on Au(111) (Figure 6.1) exist at the CNT/Au interface, comparable to the close (1 Å) dipole/CNT distance in Figure 6.4d,f. On the Au(111) reconstruction ridges, the CNT HOMO states are upshifted by ~0.5 V (Figure 6.1b), similar in magnitude to the calculated upshifting for the negative charge nearest in Figure 6.5. This significant upshift of the HOMO states suggests that the charge-transfer-induced interface dipole at the Au(111) reconstruction ridge/CNT interface is similar to the effect of an

adjacent dipole with the negative charge closest to the CNT, consistent with the enhanced electron transfer from the CNT to the Au on the surface reconstruction ridges relative to the troughs (fcc or hcp regions).

Frontier orbital localization due to a dipole

To estimate the localization of the lowest excited state in our 10 nm-long CNTs, we can use a simple particle-in-a-box model, $L = \sqrt{\frac{h^2}{8mE}}$, where h is Plank's constant, E is the "quantization energy", and m is an approximate effective mass (for a (6,5) CNT) of $m = \frac{E_G}{7.3\ eV} m_e$ (E_G is the optical band gap and m_e is the electron mass).[84, 85] To visualize the degree of CNT LDOS localization due to external charges, in Figure 6.6 we compare cross-sections of the (6,5) CNT LDOS corresponding to the LUMO and HOMO for various dipole distances from the CNT. The CNT LUMO delocalizes when the negative charge is closest to the CNT (Figure 6.6a), while the HOMO localizes in the CNT center (Figure 6.6c). We have the opposite situation when the positive charge is closer to the CNT, where the LUMO becomes more localized in the center (Figure 6.6b), while the HOMO becomes more localized on the edges of the CNT (Figure 6.6d). The same pattern was observed in the both CNT chiralities and DFT functionals explored in this paper.

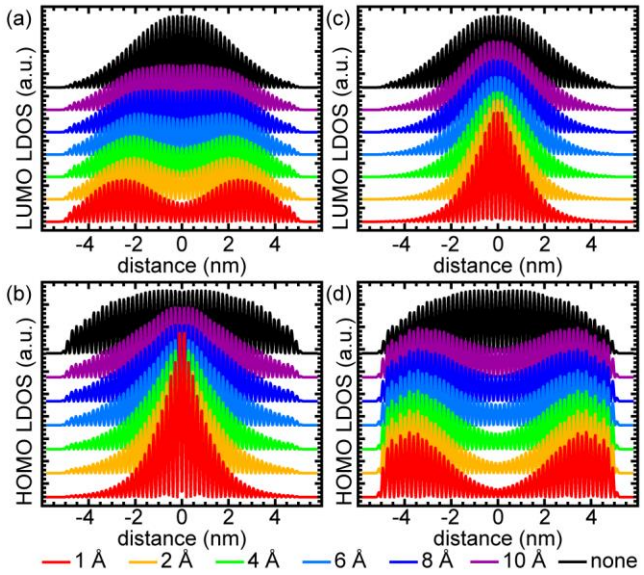

Figure 6.6. LDOS cross-sections of frontier orbitals of a 10-nm long (6,5) CNT with distances as indicated on the bottom. (a) LUMO and (b) HOMO in the case of the negative charge being nearest the CNT. (c) LUMO and (d) HOMO in the case of the positive charge being nearest the CNT. Edge effects begin to dominate outside of the central ~4-6 nm. LDOS calculated with CAM-B3LYP/STO-3G, with a FWHM of 1 meV. Curves shifted for clarity.

Comparing spectra A and B in Figure 6.2c, we find a difference in LUMO energies of 120 meV (multiplying the STM bias by the electron charge. Here we choose to focus on the LUMO due to the greater intensity of E_B versus H_B in Figure 6.2b). According to our equation for localization, 120 meV results in a length of 4.2 nm, a value consistent with the observed localization of state E_B in Figure 6.2d. We expect that the interaction between the CNT and RbI leading to the observed LDOS Figure 6.2b is electrostatic in nature, as both the presented experimental and theoretical results are consistent with electrostatic theory, and there is good correspondence between the apparent LDOS localizations.

6.4 Conclusions

In this paper, we used STM/STS and DFT to explore the impact of external electronic perturbations on the electronic structure of CNTs, in the case of both strong and weak electrostatic

interactions. STS one-dimensional mapping of CNTs adsorbed on both Au(111) and RbI revealed that modulations in the CNT LDOS can be attributed to modulations in the corresponding substrate. Our results show that Au(111) $22\sqrt{3}$ surface reconstruction ridges correspond to regions of lower hole injection from the Au to the CNT, generating local higher-energy occupied states in the CNT LDOS. We used DFT to examine the creation of localized electronic states induced by an external dipole near CNTs with selected chiralities, finding that close CNT/dipole distances resulted in significant, localized effects on the LDOS, similar to the case of CNT adsorbed on the Au(111) reconstructed surface in Figure 6.1. The DFT LDOS results also qualitatively agree with the local downward band-bending in the LDOS of a CNT on RbI, suggesting that in Figure 6.2 there is a localized, external electric field similar to a positively-charged part of a dipole influencing the CNT LDOS. These results provide qualitative insights on the localized CNT electronic states induced by electrostatic interactions with nearby charged defects. The adsorption environment of CNTs in devices are complex systems that can significantly influence the CNT electronic structure. Thus, the local impact of external dipoles on CNT LDOS merits further investigation.

6.5 Bridge to Chapter VII

We have thus far shown that coupling between a substrate and dielectric layer can impact the electronic structure of the adlayer. In the following chapter, we extend this discussion to include the effect of coupling on carbon nanotube adsorbates. We explore how carbon nanotubes interact with the electrostatic environment that arises due to substrate-adlayer coupling. As a promising alternative to Si as a transistor channel material, this study offers insight on the coupling between carbon nanotubes and the electrostatic environments within which they reside.

CHAPTER VII

MODULATION OF CARBON NANOTUBE ELECTRONIC STRUCTURE BY GRAIN BOUNDARY DEFECTS IN RBI ON Au(111)

From McDowell, B.W.; Taber, B.N.; Mills, J.M.; Gervasi, C.F.; Honda, M.; and Nazin, G.V.; Modulation of Carbon Nanotube Electronic Structure by Grain Boundary Defects in RbI on Au(111). *J. Phys. Chem. Lett.* **2024**, 15. 439.

7.1. Introduction

As electronic devices continue to shrink, silicon's limitations as a transistor channel material become increasingly difficult to overcome. Due to their one-dimensional nature, small size, well-defined structure, and ballistic charge transport properties, single-walled carbon nanotubes (SWCNTs) have myriad applications and are a leading replacement channel material.[1-7] However, many SWCNT-based devices currently underperform by more than an order of magnitude compared to their theoretical capabilities. This underperformance can be attributed to the presence of charge trapping defects in the gate dielectric in the vicinity of SWCNTs,[8, 9] resulting in deteriorated charge transport properties due to scattering and charge trapping, as investigated previously by scanning gate spectroscopy.[10-13] Advancing our understanding of these effects is challenging without direct knowledge of the changes induced in the SWCNT local electronic structure by the surrounding environment, which makes scanning tunneling microscopy/spectroscopy (STM/STS) a technique of choice in this endeavor due to its ability to probe electronic structure at the nanoscale.[14] However, previous STM/STS work has primarily focused on SWCNTs on metal substrates,[15-18] while STM/STS studies of interactions

between SWCNTs and dielectrics have been less common, and focused mainly on SWCNT band bending at the metal/dielectric interface.[19, 20] This, in part, is a consequence of the difficulty in preparing SWCNT/dielectric structures with dielectric defects whose location and properties could be independently ascertained simultaneously with STM/STS measurements of SWCNT properties. One possible approach that addresses this challenge is based on employing dielectric thin films (grown on metal substrates for compatibility with STM) with spatially extended linear defects with well-defined structures that could be investigated with STM/STS.

While a number of thin film dielectrics grown on metal surfaces could serve this purpose, alkali halide films[19, 20] are particularly appealing primarily due to the relatively well-defined nature[21-25] and wide band gaps[26, 27] of such films. Among alkali halides, NaCl has been the most extensively studied, and has been used as a dielectric to investigate adsorbates such as isolated organic molecules,[28-32] molecular assemblies,[33-36] carbon nanotubes,[19] and individual atoms.[29] An interesting alternative to NaCl is RbI, which has been shown to induce less energy broadening in STS measurements, allowing observation of finer electronic structure details in naphthalocyanine[37] and oligothiophene[38] molecules. More importantly, unlike NaCl, which grows in a rock-salt like structure with a low density of defects on a variety of metal surfaces, RbI exhibits a higher density of defects and significantly more variability in its structure on Au(111) and Ag(111), a consequence of a stronger RbI-metal interaction enabled by a weaker Rb-I bond strength.[39, 40]

Here, we use STM/STS to investigate the electronic properties of SWCNTs deposited on RbI monolayer films grown on Au(111). We find that grain boundary defects (GBDs) in RbI monolayers cause appearance of SWCNT states localized at different GBDs. We use density functional theory (DFT) calculations to investigate the GBD structures, and show that grain

boundary defects in RbI/Au(111) produce a stabilizing electrostatic potential caused by reduced coordination of iodine atoms at the RbI grain boundary. We thus develop a picture where localized SWCNT states are produced by external electrostatic disorder associated with the presence of GBDs in the SWCNT vicinity.

7.2. Methods

Experiments were carried out in a home-built ultrahigh vacuum (UHV) cryogenic STM system, where the bias voltage (V_b) is applied to the sample.[41] All imaging and spectroscopic measurements were carried out at 26 K using electrochemically etched silver tips.[42] A Au(111)/mica substrate was prepared in situ by using multiple neon sputter/anneal cycles. A sub-monolayer of RbI (obtained from Sigma-Aldrich, 99.9% purity) was deposited on to the Au surface (held at room temperature) via in situ sublimation under UHV conditions. SWCNTs (obtained from Sigma-Aldrich, >95% (carbon as (6,5) SWCNTs)) were deposited onto the RbI/Au(111)/mica substrate using the in-vacuum dry contact transfer method.[43]

All computations were performed using DFT[44] as implemented by the Vienna Ab Initio Simulation Package (VASP)[45-47] with a projector-augmented plane wave basis set.[48] The Au(111) surface was constructed with data obtained from the Materials Project[49] with approximately 25 Å of vacuum added to prevent interaction of periodic unit cells perpendicular to the surface. The hexagonal RbI structure was optimized on three layers of fcc Au (with the bottom layer frozen to retain the bulk lattice constant) via the PBE functional for solids (PBE_{sol})[50] until all forces were less than 0.005 eV $Å^{-1}$, using a 5 × 5 × 1 k-point mesh centered at the Γ point and a 500 eV planewave cutoff. The grain boundary defect structures were constructed from the DFT-optimized structure of pristine RbI on Au(111) and, using a 2 × 1 × 1

gamma-centered k-point mesh (where the non-unity direction of the k-point mesh extends along the defect), were subsequently optimized until all forces were less than 0.05 eV $Å^{-1}$. All electronic structure calculations were optimized until the change in energy between iterative steps was less than 10^{-8} eV. To evaluate whether RbI should be modeled on fcc or reconstructred Au(111), we compared the binding energy on each substrate by building commensurate supercells of each substrate type, equivalent in periodicity to 4 × 44 interatomic Au distances, where the substrate was comprised of two Au layers. The total energy of each substrate type was compared by summing the DFT-calculated binding energy ($\Delta E_{binding} = E_{RbI/Au} - E_{RbI} - E_{Au}$) with the energy gained from reconstruction of the top layer of Au,[51] indicating that adsorption of RbI to Au(111) favors (by 0.15 eV nm^{-2}) the purely fcc substrate structure rather than the reconstructed Au surface (see Appendix Table E.1), in agreement with our STM results where we do not observe reconstruction features under RbI. The change in potential due to RbI-Au interaction was calculated by subtracting the total potential (composed of ionic and Hartree components) of the isolated RbI/Au structures from the composite system: $\Delta E(r)_{interaction} = E(r)_{RbI/Au} - E(r)_{RbI} - E(r)_{Au}$. To characterize charge transfer between atoms, we used Bader analysis[52-55] with a vacuum cutoff of 10^{-3} electrons $Å^{-3}$, which kept all atomic volumes within 5% of the average for each atomic species. Visualizations of all structures were made using the VESTA package.[56] Simulations of STS were performed using the Wentzel-Kramers-Brillouin[57] approximation, using methods described elsewhere.[39]

7.3. Results and Discussion

After deposition of SWCNT's on a single-crystal Au(111) surface with sub-monolayer RbI coverage, STM imaging shows SWCNTs adsorbed across RbI monolayer islands (Figure

7.1a). To explore the electronic behavior of adsorbed SWCNTs, we have recorded a progression of STS measurements along each SWCNT (Figure 7.1c). Our STS results show the presence of a band gap and peaks similar to van-Hove singularities at the band edge, which is consistent with the LDOS observed for semiconducting SWCNTs on a variety of single-crystal surfaces.[58-60] The band gap observed here is ~1.45 V, which is in agreement with reported optical measurements of 1.27 V for (6,5) SWCNTs,[61, 62] where we expect STS to overestimate the band gap by ~14% due to the presence of a double-barrier potential at the tip-sample interface.[63] However, in contrast to these previous findings, Figure 7.1c shows significant variations of the band edge voltages along the axis of the SWCNT. The most striking observation is the appearance of localized electronic states C_1-C_5 in Figure 7.1c. These localized states are, in general, downshifted in energy and exhibit distinct STS spectra (see Appendix, Figure E.1 for more detailed spectra). These LDOS variations are different from those expected for SWCNT point defects, which we also observe (Figure E.2).

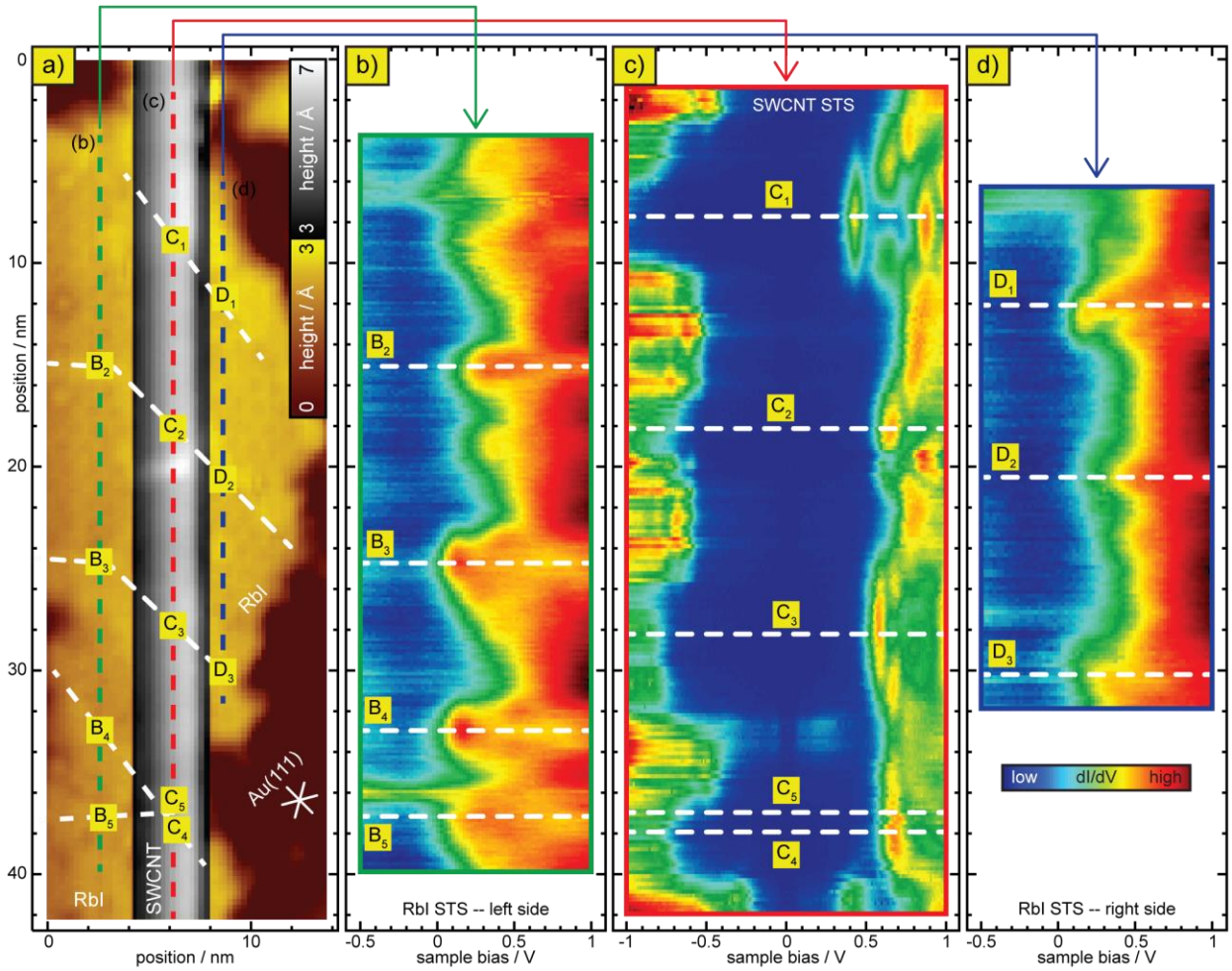

Figure 7.1: STS measurements of LDOS variation along SWCNT. a) STM topography (V_b = 1 V, I = 2 pA) of a SWCNT on RbI/Au(111). The white dashed lines indicate the position of linear defects in the RbI monolayer. The vertical dashed lines show the path of STS measurements. b-d) STS measurements along SWCNT, recorded to the left of (b), on top of (c), and to the right of (d) the SWCNT. The horizontal white dashed lines show the position of linear defects in each STS measurement.

By examining one of the SWCNT regions with localized electronic states, we observe a progression of states exhibiting particle-in-a-box-like behavior (Figure 7.2). By mapping our STS measurement in two dimensions at specific energies, we can directly visualize zero- (Figure 7.2d) and single-node localized states (Figure 7.2e). Importantly, we also observe a localized RbI state (Figure 7.2c) which runs underneath the SWCNT at approximately a 45° angle, and is directly aligned with the position of the SWCNT localized states in Figures 7.2d,e. To

investigate whether other localized states in the SWCNT exhibit similar spatial alignment to RbI LDOS features, we have recorded progressions of STS measurements across RbI on either side of the SWCNT, in the direction along the axis of the SWCNT (Figures 7.1b,d). Figures 7.1b,d show that RbI contains several linear defects crossing beneath the SWCNT, which can be identified by raised, linear regions in the STM topography (Figure 7.1a, with a high contrast version shown in Appendix, Figure E.3) and local LDOS features (Figure 7.1b,d). In these linear defect regions, the RbI LDOS is downshifted in energy, similarly to the downshifted LDOS of the SWCNT.

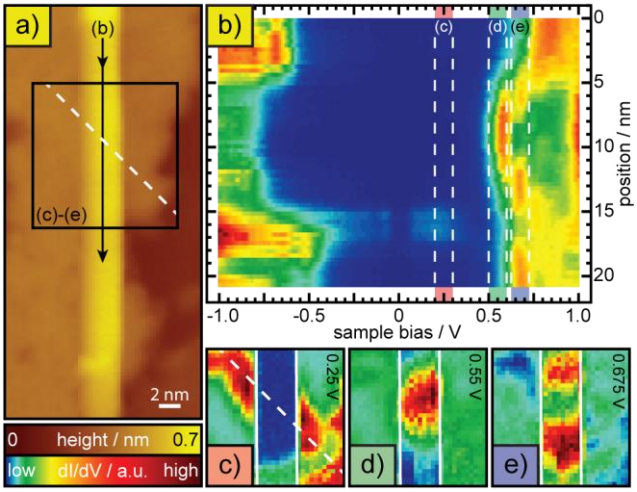

Figure 7.2: STS measurements of a localized particle-in-a-box-like SWCNT state. a) STM topography (V_b = 1 V, I = 2 pA) of a SWCNT adsorbed across a monolayer of RbI. b) STS measurements performed along the axis of the SWCNT, along the path shown in (a), showing localized states with particle-in-a-box-like behavior. c-e) 2D maps of STS intensity at energies corresponding to a state localized to the linear RbI defect (c: 0.25 V), and the zero (d: 0.55 V) and one (e: 0.675 V) node quantum confined SWCNT states. These 2D maps correspond to the energies of the color-coded vertical slices shown in (b) and the spatial range shown in (a). The vertical white lines show the approximate edge of the SWCNT and the diagonal white dashed line shows the position of an RbI defect, corresponding to the one intersecting B_3-D_3 in Figure 1.

While both the RbI and SWCNT LDOS show similar downshifts in energy in the defect vicinity, we also observe the same downshift in RbI defect areas that are spatially removed from the SWCNT, which suggests that states C_1-C_5 originate from some interaction with the RbI. To

better understand the nature of this interaction, we focus on the RbI defect areas in the following. Our STM topography suggests that the linear defect regions correspond to GBDs in the RbI monolayer, which arise from discontinuous growth between adjacent RbI islands (Figure 7.3a,h). While we observe many different examples of these GBDs, they consistently grow along the <100> directions of the Au(111) surface and exist at the boundary formed between two monolayer islands of RbI. In addition to the linear defects of the type observed in Figure 7.1a, we also observe wider defects that have an additional unit cell of space between the RbI monolayer islands (Figure 7.3h). Because both types of defects are related, we will discuss them both, and refer to them as 'narrow' and 'wide' in the following. To understand the structure of these defects, we employ STS, and extend the energy range of our STS measurements to image-potential states (found at high voltages), which has been useful in understanding alkali halides on metals in previous studies.[21, 64]

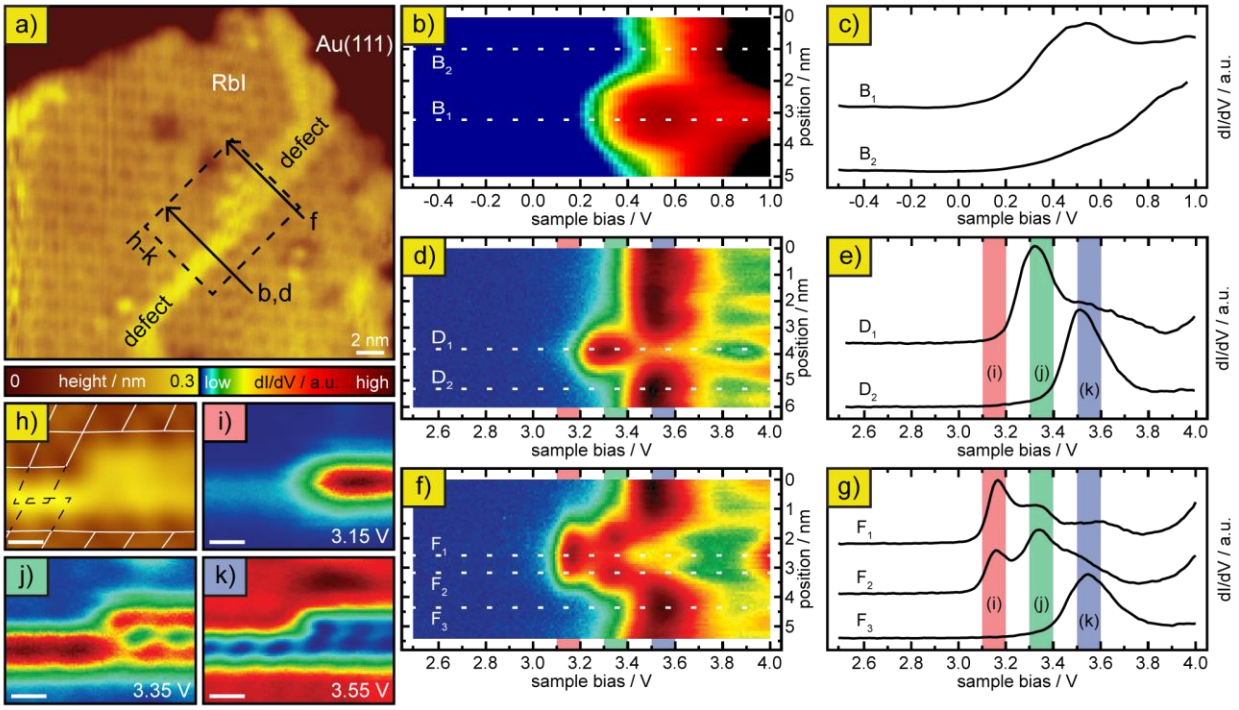

Figure 7.3: STS measurements of GBD in RbI. a) STM topography (V_b = 1 V, I = 10 pA) of an RbI island containing a GBD, which has both 'narrow' and 'wide' regions. b,d,f) Progression of STS measurements recorded at low (b) and at high bias voltage across 'narrow' (d) and 'wide'

(f) portions of the defect. These measurements show states that are localized to the GBD, with the positions showing the clearest localization represented by the individual STS measurements (B_1-B_2, D_1-D_2, F_1-F_3) shown in (c,e,g). h) STM topography showing a discontinuity in the lattices of adjacent RbI monolayers. The white outline shows the pristine lattice of each RbI domain, and the dashed outlines show the discontinuity. i-k) STS measurements recorded over the same spatial range as (h) at specific energies to show the 2D localization of states at the defect.

By recording many STS measurements across a linear RbI defect (as shown in Figure 7.3a) we observe that the LDOS is downshifted at defect locations at both low (Figure 7.3b) and high (image potential state) (Figure 7.3d,f) voltage ranges (intermediate voltage range does not show discernible peaks). At low bias voltages, like those shown in Figure 7.1b,d, we observe spatially localized peaks at the linear defect near bias voltages of 0.5 V (B_1 in Figure 7.3c); there is no peak in the pristine RbI LDOS (B_2 in Figure 7.3c). Meanwhile, at larger bias voltages, we observe LDOS peaks attributable to image potential states,[21, 64] which at the linear defects (D_1 in Figure 7.3e and F_1,F_2 in Figure 7.3g) are lower in energy than the peaks in the pristine RbI structure (D_2,F_3 in Figures 7.3e,g). The fact that RbI states at both low and high voltage as well as the SWCNT states are similarly downshifted suggests that the GBDs may have a stabilizing electrostatic potential.

Figure 7.3 allows us to make another set of observations that will be important for our analysis. While the 'narrow' GBD shows a single localized state (D_1 in Figures 7.3d,e) that is downshifted from the first image potential state of pristine RbI (D_2 in Figures 7.3d,e), the 'wide' GBD shows a two different types of downshifted states: F_2 in Figures 7.3f,g (localized at the edges of the defect) and another further downshifted state F_1 in Figures 7.3f,g (localized at the center of the defect). Two-dimensional spatial STS mapping shows that LDOS at 3.35 V (middle peak in Figure 7.3g) is found throughout the entirety of the 'narrow' GBD region and at the edges of the 'wide' GBD region (Figure 7.3j). In contrast, the lowest downshifted state at 3.15 V

(Figure 7.3i) is only found in the middle of the 'wide' GBD region. In the following, we use the electronic landscape of RbI defects portrayed by Figure 7.3 as a reference for density functional theory (DFT) simulations of this system, which are necessary to obtain an atomic-level understanding of RbI defects in the present case due to the lack of full atomic resolution in experimentally obtained STM topographies.

While the GBD atomic structure is not clear from STM topography, the latter does allow us to constrain the types of possible GBD structures. Specifically, STM topography shows that RbI monolayers have a hexagonal structure rather than the typical square alkali-halide structure observed for NaCl, a consequence of the weaker alkali-halide interaction, analogous to previous findings for RbI on Ag(111).[39] Further, analysis of STM topography of the GBD from Figure 7.3 shows that the GBD arises at the interface of two RbI monolayers displaced with respect to each other by one Au atomic spacing along the <100> direction parallel to the GBD (see Figure 7.4a and Appendix, Figure E.4, S5a). As a result of this displacement, adlayer atoms at the discontinuity are undercoordinated as compared to the atoms in the pristine RbI monolayer. However, our DFT calculations show that the geometries shown in Figures 7.4a and S5a would not be energetically favorable, due to the polar nature of RbI edges, which suggests that the GBD structure is more complex. To optimize the GBD structure, we added individual RbI molecules to the region between the pristine RbI phases. This approach follows that of previous calculations for GBDs in NaCl on Ir(111), where NaCl molecules bridge the region between discontinuous pristine domains.[65] In the case of the 'narrow' defect region, addition of a single RbI molecule ensures that each Rb (iodine) atom is adjacent to three iodine (Rb) atoms (Figure 7.4b). For the case of the 'wide' defect region, addition of three RbI molecules with alternating orientation accomplishes the same result (Figure S5b). Importantly, while this results in a

structure where each Rb (iodine) atom is coordinated to three iodine (Rb) atoms, the atoms in the defect area have significantly longer Rb-I bond lengths, on average, than atoms in the pristine RbI structure.

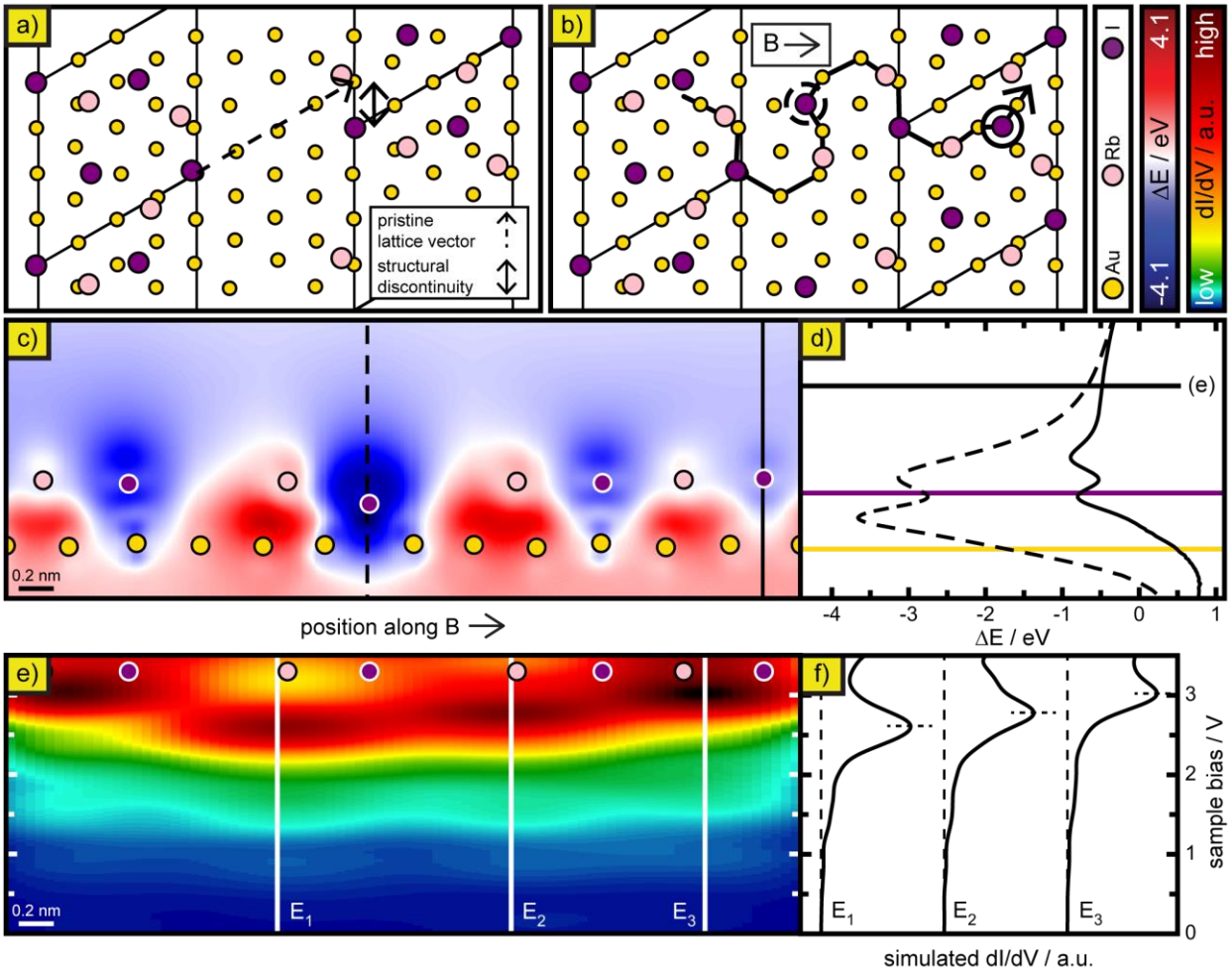

Figure 7.4: DFT-calculated electronic potential changes at 'narrow' RbI GBD. a,b) DFT-optimized atomic models of 'narrow' GBD in an RbI monolayer. The structural discontinuity between two adjacent RbI phases is highlighted in (a), with the dashed arrow showing the propagation of the pristine lattice vector from the left-side domain and the discontinuity shown as the vertical double-arrow. In (b), one RbI molecule per unit cell is added to bridge the empty region between discontinuous phases. The path along which potential energy (c) and simulated STS (e) are taken is indicated by the arrow. c) DFT-calculated change in electronic potential due to RbI-Au interaction is shown in the direction orthogonal to the surface, and is sliced along the path shown in b. d) Change in electronic potential due to RbI-Au interaction sliced at the position of specific iodine atoms, indicated by the circles in b and the vertical lines in c. The horizontal lines show the average position of Au (gold), iodine (purple), and the height at which the STS measurement is simulated (e). e) Simulated STS measurement at a height of 0.5 nm above the surface, taken along the path shown in (b). f) Individual simulated STS spectra, taken from the position of the vertical lines shown in (e).

As a result, in the defect area, adlayer atoms have less interaction with other adlayer atoms due to a less dense packing (vs the pristine structure), leading to a more significant interaction with the Au(111) substrate. The strength of this interaction can be gauged by the net electron count of adatoms, which, for example, for iodine atoms in the pristine RbI structure ranges from +0.20 (for the most Au-coordinated) to +0.61 (for the least Au-coordinated iodine atoms). This suggests that the high Au-I coordination facilitates electron transfer from the adlayer to the substrate, in line with previous results for RbI on Ag(111).[39] The net electron counts of iodine atoms in the GBD, which fall in the range of +0.20 to +0.14 electrons, are lower than for iodine atoms in the pristine RbI structure, on average (+0.45 electrons). In contrast, while Rb atoms at the GBD show a similar trend, the effect of coordination on electron transfer is less pronounced, with net electron counts for Rb atoms at the GBD falling in the range of -0.84 to -0.85 electrons, which is larger than for Rb atoms in the pristine structure (-0.83 electrons).

The net electron counts of iodine atoms in the GBD have a profound impact on the local electrostatic potential. This can be most conveniently visualized as the change in potential energy of electrons due to RbI adsorption, as shown in Figures 7.4c and S5c, which demonstrate that adsorption of Rb (iodine) atoms increase (decrease) the potential energy of electrons at and above the top layer of the Au surface. This difference in behavior between atom types can be explained by charge screening in the metal surface, where adsorption of the positively charged Rb (negatively charged iodine) atoms results in electron accumulation (depletion).

For the 'narrow' GBD, the lower net electron count of iodine atoms in the defect area (+0.16 electrons) relative to iodine atoms in the pristine structure (+0.45 electron) leads to a deeper, more stable potential (compare dashed to solid lines in Figure 7.4d). Similarly, for the 'wide' defect, iodine atoms at the middle of the GBD have lower net electrons counts (+0.14

electrons) than for iodine atoms at the edge of the GBD (+0.20 electrons) and in the pristine structure. This leads to a potential that is more stable in the middle of the defect than at the edges or in the pristine structure (compare dashed to solid lines in Figure S5d). In summary, iodine atoms at the GBD experience substantial electron transfer to Au, resulting in a less negative electrostatic environment at the defect where lower (higher) net electron counts result in a more (less) stabilizing potential.

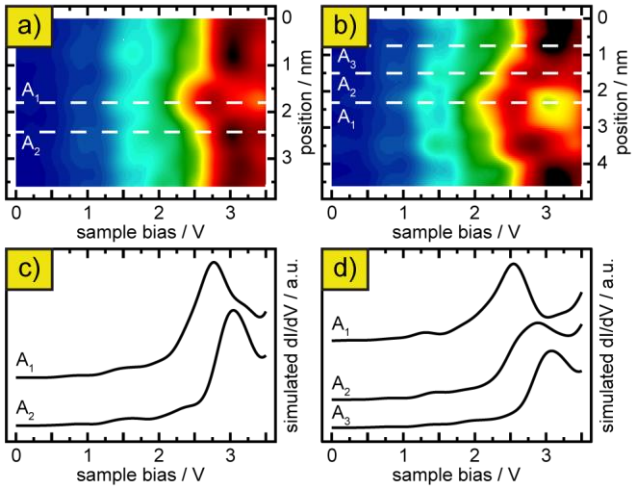

Figure 7.5: Simulated STS measurements for 'narrow' and 'wide' RbI GBD's. Progression of simulated STS spectra recorded across 'narrow' (a) and 'wide' (b) GBD's, taken along paths analogous to those recorded in experiment (see Figure 3). Localized states are highlighted by individual STS spectra, as shown in c,d for 'narrow' and 'wide' GBD's respectively.

To understand how the stabilizing electrostatic environment at the GBD could result in the localized states observed by STS, we have simulated STS spectra along paths that spatially intersect various symmetrically distinct adlayer atoms in the GBD structure (Figures 7.4e and S5e). Our results show localized states analogous to the image potential states observed in experiment, where the energies are slightly lower due to the well-known tendency of DFT to underestimate band gaps. These states are mostly centered on Rb atoms, which is in-line with previous results on the atomic contributions for states in this energy range for RbI.[39] Despite being mostly centered on Rb atoms, the effect of the stabilizing potential at iodine atoms is

clearly important, with the Rb atoms nearest to (furthest from) the most (least) stabilizing potentials showing the lowest (highest) energy peaks. To allow direct comparison to experiment, following a similar approach, we have simulated progressions of STS spectra along the spatial coordinate orthogonal to both 'narrow' (Figure 7.5a) and 'wide' (Figure 7.5b) GBD's, which show spatial behaviors similar to those found in experimental data shown in Figures 3d and 3f respectively. For the 'narrow' GBD, these results show a single localized state at the defect (A_1 in Figure 7.5c) that is downshifted by 0.3 V relative to the pristine state (A_2 in Figure 7.5c), in agreement with our experimental STS results where we observe a 0.2 V energy difference. For the 'wide' GBD, our results show a pair of states (localized at the edges of the defect, A_2 in Figure 5d) that are 0.4 V lower in energy than for the pristine state (in agreement with the energy difference of 0.2 V in experimental STS), and a state localized to the center of the defect (A_1 in Figure 7.5d) which is 0.6 V lower in energy than for the pristine state (in agreement with the energy difference of 0.4 V in experimental STS). Overall, the theoretically calculated LDOS at the GBD is in agreement with previous results for similar defects in NaCl on Ir(111), where atoms at the defect were shown to have, in general, downshifted LDOS.[65] The quantitative agreement of results shown in Figure 5 with experimental data (Figure 7.3) thus suggest that the electronic states observed in experiment are downshifted due to the stabilizing electrostatic potential of the GBD.

Finally, we return to the impact of these GBDs on the electronic structure of the adsorbed SWCNT. While we have presented one specific example of a GBD, our explanation may be applied to other RbI GBDs, which may be expected to incorporate less densely packed Rb and iodine atoms in the defect area leading to increased Rb-I bond lengths and, consequently, the type of stabilizing electrostatic potential discussed above. Since the stabilizing electrostatic

potential present at the GBD extends well above the surface, it also affects the SWCNTs, which should result in a LDOS that is perturbed and downshifted near each of the GBDs (Figure 7.1c). Indeed, the downshifting observed in the SWCNT LDOS near GBDs is similar in magnitude to the shifts calculated for image potential states in Figure 7.5. The localization we observe (approximately 10 nm for unoccupied states in Figure 7.1c) is larger than the GBD width (1 nm for 'narrow' and 2 nm for 'wide' structure in Figure 7.4,S5), in agreement with previous studies of SWCNT LDOS confinement by external electrostatic interactions, where localization on the order of 4-8 nm was observed for a dipole-like external potential.[20] The exact SWCNTs LDOS pattern at each GBD appears slightly different, which agrees with the expectation that distinct structures of different GBDs may lead to somewhat different electrostatic potentials. While there are other various LDOS effects present in the SWCNT studied here, which could be attributed to interactions with point defects or domain edges in RbI, we find that interaction with GBDs lead to significant perturbations of the SWCNT LDOS.

7.4 Conclusions

To summarize, we have characterized the local density of states of SWCNTs adsorbed across monolayer islands of RbI. The SWCNT local density of states exhibits many localized states, each associated with a RbI grain boundary defect in its vicinity. Our DFT calculations show that strong Au-I interactions lead to a stabilizing electrostatic environment at the RbI defects, as experimentally evidenced by the downshifting of image potential states at the grain boundary defects. The adsorbed SWCNT is coupled to this electrostatic environment, resulting in downshifted and localized states near the grain boundary defects. More broadly, since the presence of an electrostatic disturbance at the grain boundary defects is not tied to a particular

atomic configuration, we expect that the physical picture described here may be relevant for adsorbates on other ultra-thin films containing grain boundary defects. Finally, our results provide an electronic state-resolved visualization of the impact of external electrostatic disorder on the SWCNT electronic landscape, a question of relevance for SWCNT-based devices affected by the presence of individual charge traps in the vicinity of SWCNTs.

7.5 Bridge to Conclusion

In this work, we have shown an example of a system in which coupling in a single-layer material leads to impactful interactions in a nanoscale electronic device setting. The physical picture we present shows a mechanism by which an ultra-thin dielectric is affected by coupling to the substrate it is grown on, and in turn significantly affects the electronic structure of an adsorbed SWCNT. This observation is important, in that it identifies a previously unreported effect that could be present in SWCNT-based devices, which is impactful in the ongoing effort to improve the performance of SWCNT-based devices. For example, the abundance of GBDs in single-layer RbI could be affected by the experimental conditions under which the sample is annealed. By annealing the sample for longer or at higher temperatures, the RbI atoms are given more energy to find the most stable structure, which we expect to be a pristine monolayer without GBDs. More broadly, this work serves as further motivation to better understand the coupling in other nanoscale materials, as we have shown that coupling can be impactful in the setting of nanoscale electronic devices.

CHAPTER VIII

CONCLUSION AND FUTURE WORK

In this work, we examined the role of strong chemical interactions in nanoscale materials that lead to structural and electronic coupling. Using RbI as a model dielectric, we began by showing that single-layer RbI can exhibit structural coupling to the surface it is grown on. Our scanning tunneling microscopy/spectroscopy (STM/STS) results show that RbI forms two distinct, bistable structures on Ag(111), in contrast to the expected behavior for other alkali halides which showed only one structure type. These distinct, bistable structure types are the direct result of coupling to the Ag(111) surface; one structure corresponds to a single layer of the bulk structure, while the other is template by the Ag(111) surface and adopts its symmetry. This work shows that strong interactions between an ultra-thin dielectric and metal surface can lead to structural coupling, and in this case resulting in a previously unreported RbI structure.

Next, we showed that these distinct single-layer RbI structures have important electronic differences – a result of differences in the strength of interaction between each RbI structure and the Ag(111) surface. By using a combination of STS and first-principles numerical simulation, we show that these differences are manifested by dramatically different electronic properties, where the work function and dielectric constant are distinct for each single-layer RbI structure. Our STM/STS results also show that there are local variations in the electronic properties of each single-layer RbI structure, which are manifested in a moiré pattern and grain boundary defects (GBDs). These results extend the physical picture offered in the previous section to show how strong chemical interactions can lead to distinct electronic properties in the pristine and defect structures of single-layer RbI.

Again using RbI as a model dielectric system, we then examined how coupling between the Ag(111) surface and single-layer RbI leads to spatial modulation of electronic states confined to the substrate/adlayer interface (IES). Here, we find that the spatial modulation of IES is stronger for RbI than has been reported for other alkali halides, which is a direct result of RbI having stronger substrate/adlayer interactions than other alkali halides. An interesting result of RbI having stronger/substrate adlayer interaction is seen in the electron mass, which is anisotropic (by a factor of roughly 3x) for different directions along the surface, in surprising contrast to previous results for other alkali halides which report a single, isotropic mass. This comparison to existing results for other alkali halides develops a notion of how the behavior of IES should change for materials with different strengths of substrate/adlayer coupling.

Next, we examined how our understanding of RbI as a model dielectric could be used to interpret interactions with a single walled carbon nanotube (SWCNT). We used STM/STS to show that single-layer RbI can impact the electronic structure of an adsorbed SWCNT by inducing band-bending, and that this interaction can be modeled through electrostatic interaction with a simple dipole.

From this, we extended our characterization of this system to consider localized interactions at GBDs in the RbI. Our STM/STS results show that GBDs in single-layer RbI lead to localized electronic states in an adsorbed SWCNT, as well as significant band-bending. By modeling these GBDs with density functional theory (DFT), we show that these GBDs transfer more electrons to the substrate (relative to the pristine structure), resulting in locally stabilizing electron potentials. These stabilizing electron potentials are relatively diffuse away from the surface, and thus trap electronic states in the adsorbed SWCNT. Importantly, these conclusions are a general observation of GBDs, and may be broadly applicable to similar defects in other

dielectric materials. This work is thus an important observation of a specific mechanism by which SWCNT-based devices might underperform relative to theory, as a result of electron trapping and scattering by local electrostatic potentials in the substrate.

In summary, we have explored the role of coupling in nanoscale materials, which leads to both structural and electronic effects. The work described here identifies the role of substrate/adlayer interactions in instilling this coupling, and we identify how the strength of these interactions might scale with expected chemical trends. Furthermore, we show how this coupling can be significant in the setting of a nanoscale electronic device, where a single-layer dielectric was shown to significantly affect the behavior of a transistor material. The insight offered here serves as further motivation to better understand the electronic behavior of materials in nanoscale devices.

APPENDIX A

SUPPORTING MATERIAL FOR CHAPTER III

LDOS of RbI monolayer structure types

Our density functional theory (DFT) optimized structures provide insight on the local density of states (LDOS) of the RbI monolayer (Figure A.1). These results show that the occupied states are primarily contributed by iodine. Unoccupied states up to around 0.5-1 eV above the Fermi level are also dominated by iodine orbitals, while the unoccupied states at higher energies are dominated by Rb orbitals. This finding is consistent for both structure types observed in experiment, as well as other test structures. Additionally, there is significant mixing with Ag states, resulting in the loss of a well-defined band gap, as is present for the case of an adlayer isolated from the substrate.

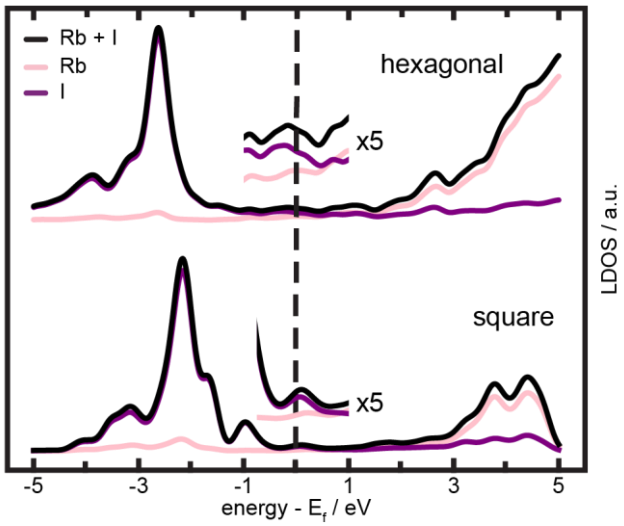

Figure A.1. Normalized DFT-calculated LDOS for both structure types of the RbI monolayer. The spectra are averaged across each atom in the unit cell.

Scanning tunneling spectroscopy of field emission resonances on RbI and Ag(111)

To qualitatively characterize how electrons are transferred between the adlayer and substrate, we have performed scanning tunneling spectroscopy (STS) in the bias voltage range that corresponds to field emission resonance states (Figure A.2). These results show that the first field emission resonance state is lower on both RbI structures relative to the bare Ag(111) surface. This indicates that the work function is reduced by adsorption of RbI, which is associated with a net electron transfer from the adlayer to the substrate.[1, 2]

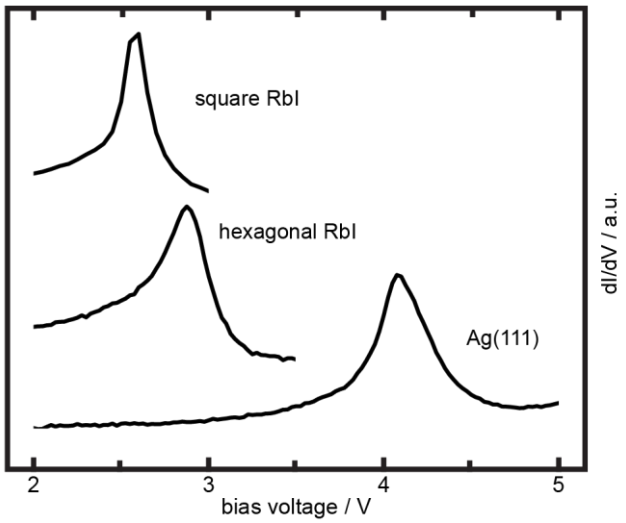

Figure A.2. Representative STS measurements (V_b = 2 V, I = 10 pA, V_{pp} = 40 mV) recorded on both RbI structures and the bare Ag(111) surface. The STM feedback was left on for each of these measurements.

Dependence of LDOS on adsorption site

Our DFT results suggest that charge redistribution interactions result in shared electron density between the adlayer and substrate. Previous studies of other alkali halides have characterized this shared charge density by comparing the LDOS of adlayer atoms in distinct adsorption sites.[3, 4] In following this approach, we consider the how the LDOS near the Fermi level is affected by the adsorption geometry of the RbI hexagonal structure (Figure A.3). The variation in LDOS near the Fermi level for different adsorption sites is much more significant for

iodine (Figure A.3c) than Rb (Figure A.3b). This suggests that the formation of covalent bonding between the adlayer and substrate is more sensitive to the placement of iodine than Rb, in agreement with previous results for other alkali halides.[3, 4] Further, both Rb and iodine show a significant difference in LDOS for atoms in the first vs second layer. Atoms in the first layer show a manifold of states around the Fermi level, whereas there is a pronounced band gap for atoms in the second layer. This indicates that the states near the Fermi level arise from interaction with the Ag substrate.

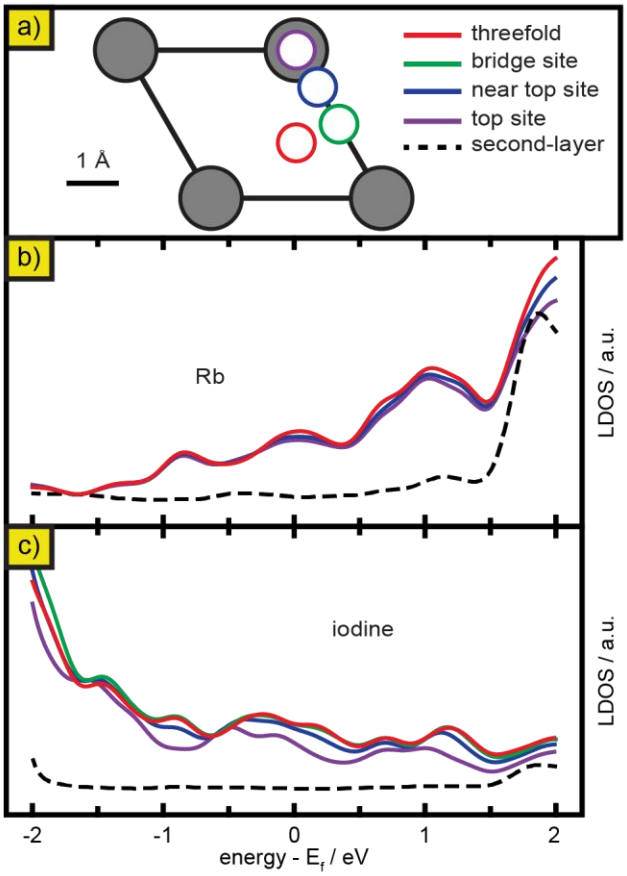

Figure A.3. Varation of adlayer LDOS with adsorption site for the hexagonal RbI monolayer. a) the different distinct adlayer positions considered in b,c. b,c) the average DFT-calculated LDOS for Rb (b) and iodine (c) for different distinct adsorption sites, as indicated by the color of the spectra. The black, dashed curve corresponds to the average LDOS for an atom in the second layer of the hexagonal RbI structure.

Calculation of preferred Ag(111) binding sites for Rb and iodine

To characterize the binding interaction of Rb and iodine adlayer atoms on the Ag(111) surface, we performed a series of DFT calculations in which a single adlayer atom was placed at a position on the surface and allowed to relax in the direction perpendicular to the surface. The results of these calculations are shown in Figure A.4, were we have mapped the relative height of the adlayer atom and relative binding energy for each adlayer atom type.

These results show that both adlayer atom types prefer to bind in a hollow between three Ag atoms, as opposed to on top of an Ag atom. Both the hcp and fcc hollow sites show a similar binding preference. However, iodine favors binding in a hollow site by approximately 7.5 times more than Rb. This indicates that iodine is more influential in determining the adlayer structure, since it has a stronger preference to bind in a hollow site. In both cases, the adlayer atoms sit closer to the surface in a hollow site than when placed on top of an Ag atom.

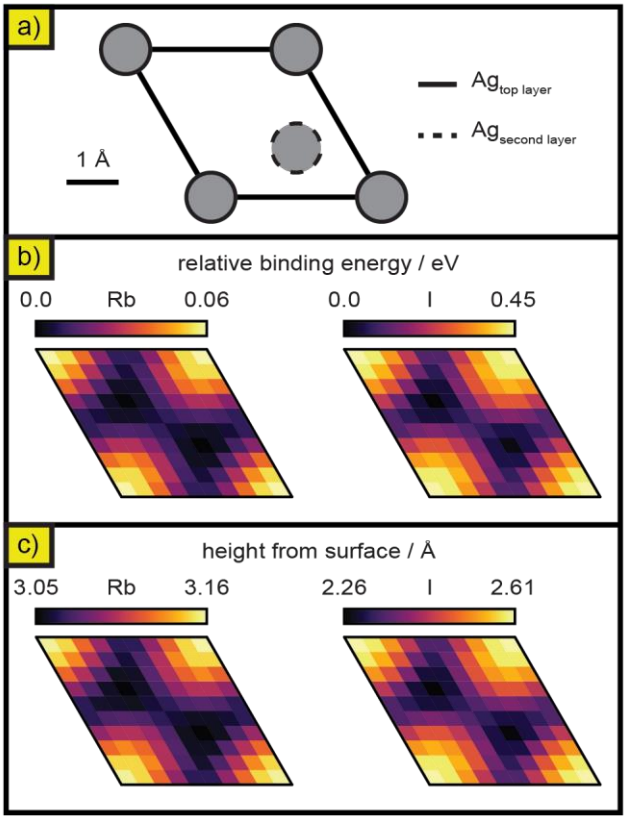

Figure A.4. Mapping binding parameters for a single adlayer atom on the Ag(111) unit cell. The adlayer atom is translated to each position in the unit cell and allowed to relax in the direction perpendicular to the surface. a) the unit cell of Ag(111) over which an adlayer atom is translated in b,c. b) map of relative binding energy for Rb (left) and iodine (right) atoms. c) map of the optimized height from surface for Rb (left) and iodine (right) atoms.

Calculation of possible hexagonal RbI structures

In our characterization of the hexagonal RbI monolayer, we determined several high-symmetry structures that show the periodicity observed in experiment. These structures (shown in Figure S5) differ by translation of the RbI monolayer relative to the Ag(111) surface, which changes the coordination of individual adlayer atoms to the surface.

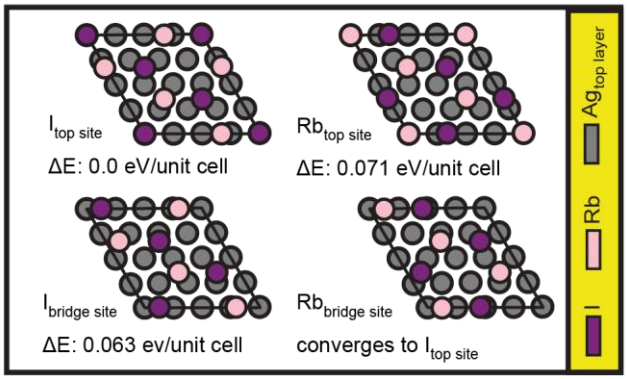

Figure A.5. Possible structures with unit cells commensurate with our experimental results are shown, with their relative DFT-optimized energy.

These results indicate that the most stable structure is the $I_{top\ site}$, since it shows the smallest relative energy. In experiment, we have observed these structures to span hundreds of unit cells, indicating that a difference of 0.063 eV per unit cell is significant and likely dictates the selective formation of the $I_{top\ site}$ structure.

Morphology of the square RbI structure

While scanning tunneling microscopy (STM) topography at low bias is dominated primarily by the morphology of the surface, at higher bias voltages the topography is affected by

both the morphology and the LDOS of the surface due to a larger tip-sample distance. In STM topographies of the square RbI monolayer at high bias voltages, we observe features that are commensurate with the moiré pattern formed with the Ag(111) surface. To understand whether these features originate primarily from the morphology or LDOS of the surface, we compare the adlayer morphology to simulated STM topographies in Figure A.6.

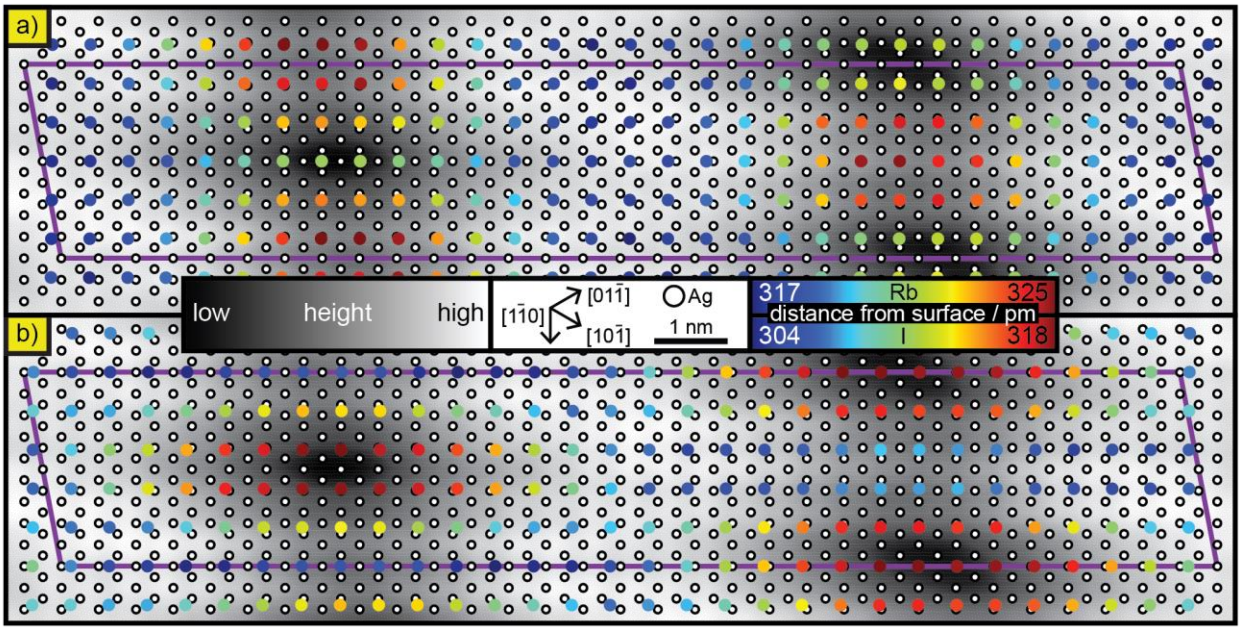

Figure A.6. Comparison of RbI structure morphology to simulated STM topography. The color of adlayer atoms represents their height above the top layer of Ag, as indicated by the colorbar on the right. For clarity, only one adlayer atom type is shown in each panel: Rb in (a) and iodine in (b). A LDOS map (identical to that shown in the main text, Figure 3.5d; integrated from 0.0 to 1.2 eV above the Fermi level and sampled at a height of 12 Å above the surface) is shown for each panel.

Here, we compare the height of adlayer atoms to a simulated STM topography. In general, the relative height of adlayer atoms is the opposite of what one would expect from the STM topography. Areas that appear high (low) in STM topography align with regions of the adlayer that are closer to (further from) the surface. Additionally, the overall height variation of adlayer atoms (Rb: 8 pm; I: 13 pm) is roughly 10x smaller than the height variation observed in STM topography (~100 pm, see main text, Figure 3.5b). As a result, the features observed in

STM topography at high bias voltages do not originate from the morphology of the RbI square structure.

Relation of coordination and charge transfer in the square RbI monolayer

Due the large size of the unit cell for the square RbI monolayer (300 adlayer atoms per unit cell), it is insufficient to describe the coordination of atoms categorically, as we have done for the smaller hexagonal RbI monolayer. As a result, it is necessary to visualize the spatial dependence of net electron counts in the adlayer, from which a qualitative understanding of the surface/adlayer coordination follows intuitively. These visualizations are shown below, and depict the net electron counts for Rb (Figure A.7a) and iodine (Figure A.7b).

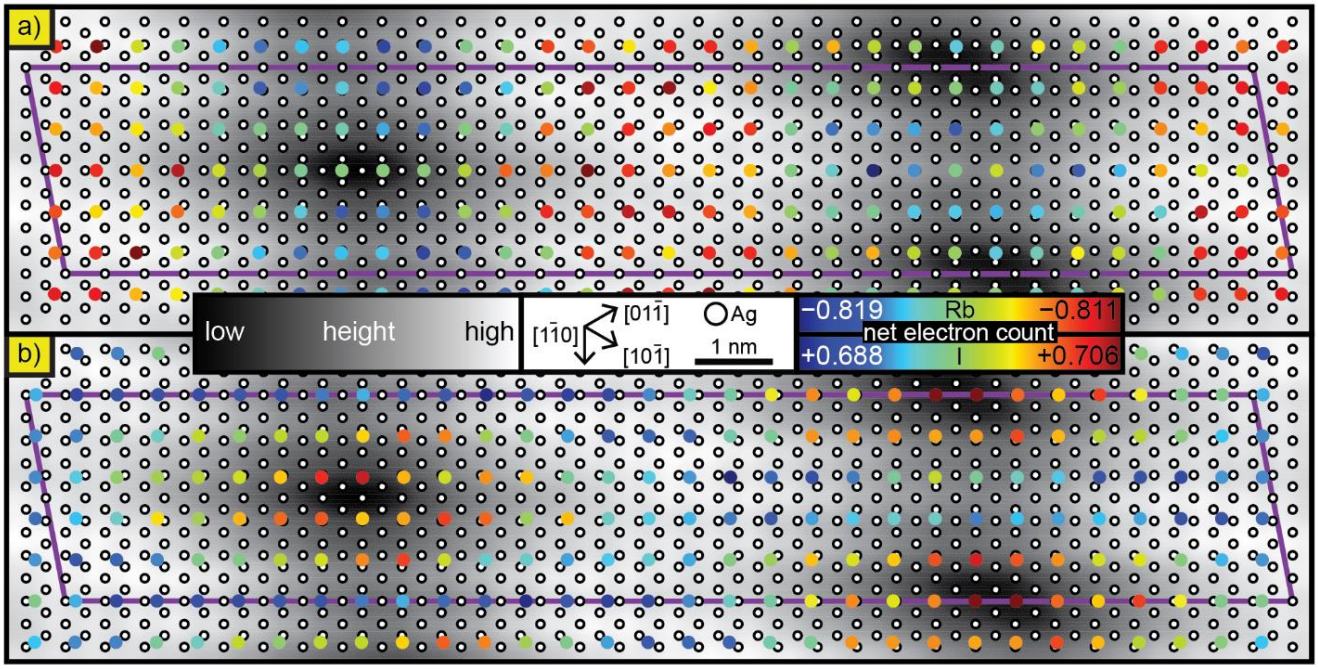

Figure A.7. Visual depictions of the dependence of adlayer (a: Rb; b: I) net electron counts on the extent of surface/adlayer coordination. The color of adlayer atoms represents their net electron counts, as indicated by the colorbar on the right. For clarity, only one adlayer atom type is shown in each panel. A LDOS map (identical to that shown in the main text, Figure 3.5d; integrated from 0.0 to 1.2 eV above the Fermi level and sampled at a height of 12 Å above the surface) is also shown for each panel.

From this visualization, several relationships are qualitatively apparent. First, the net electron counts of iodine have a wider range (+0.688 to +0.706 net electrons) than for Rb (-0.819 to -0.811 net electrons). This is a consistent finding for many different kinds of RbI monolayer structures that we have calculated, and we attribute it to iodine (Rb) forming stronger (weaker) bonds with Ag (see main text Figure 3.3). Second, the net electron counts of iodine are more closely related to surface/adlayer coordination than for Rb. Iodine atoms that are coordinated to more (less) Ag atoms have a lower (higher) net electron count, which is not necessarily true for all Rb's. This follows from the previous point, which suggests that we expect iodine (Rb) to experience more (less) charge transfer with Ag. As a result, the net electron count of iodine is mostly dictated by its own coordination to Ag. Conversely, the net electron count of Rb is related to its coordination to Ag, but also experiences a significant contribution that depends on the surface/adlayer coordination of the iodines to which it is bound. Third, the LDOS intensity is most closely related to the net electron count of iodine, not Rb. For example, the sections of the unit cell with high LDOS contain Rb's with both the highest and lowest net electron counts, while the sections of the unit cell with low LDOS contain Rb's with mostly average net electron counts. On the contrary, the sections of the unit cell with high (low) LDOS contain iodines with the lowest (highest) net electron counts. This result for iodine is consistent with our results for the hexagonal phase, which showed that smaller (larger) net electron counts yield more (less) unoccupied states. Since we observe a wider range of net electron counts for iodine than for Rb, it follows that the contrast in our STM topography aligns most closely with the surface/adlayer coordination of iodine.

Calculation of binding energies for RbI structures on Ag(111)

In calculating the strength of binding between Ag(111) and the various RbI structures considered, we address the effects of Van der Waals (VDW) corrections below. We find that, while inclusion of VDW corrections leads to a larger overall binding energy for each RbI structure, the relative differences in binding energies between structures changes less significantly (see Table A.1). For example, including VDW corrections for the square structure only changes the binding energy by ~20 meV per RbI molecule relative to the hexagonal single-layer structure, which could be within the error of the calculation. The change associated with including VDW corrections for the hexagonal double-layer structure is more pronounced, and the binding energy increases by ~120 meV per RbI molecule relative to the hexagonal single-layer structure. This difference is likely due to the fact that the VDW forces are largest when the surface/adlayer interfacial area is maximized, as in the case for the single-layer structures. In conclusion, we find that, while the inclusion of VDW corrections leads to stronger binding energies, the relative differences between the different RbI structures remains qualitatively similar. Therefore, for ease of reproducibility, we have chosen to include the relative binding energies without VDW corrections in the main text.

	Hexagonal (single layer)	**Square**		**Hexagonal (double layer)**	
Binding energy (eV per RbI molecule)	Actual	Actual	Relative to hexagonal (single-layer)	Actual	Relative to hexagonal (single-layer)
No VDW correction	-0.53564	-0.2989	0.236741	-0.21366	0.321977
DFT-D2	-1.1469	-0.94239	0.204509	-0.63885	0.508053
DFT-D3	-0.99438	-0.76609	0.228291	-0.49966	0.494717
Average			0.223180		0.441582

Table A.1. DFT-calculated binding energies for the different RbI structures considered. Binding energies were calculated by subtracting the energy of the isolated substrate and adlayer from the energy of the substrate/adlayer structure. All reported values are in eV per RbI molecule. The

binding energies are calculated as: $\Delta E_{binding} = \frac{E_{substrate+adlayer} - E_{substrate} - E_{adlayer}}{\#\ of\ RbI\ molecules\ in\ unit\ cell}$, using the geometry of the structure optimized without VDW corrections.

Double-layer hexagonal RbI structure

To understand the growth preference of ultra-thin RbI, it is helpful to consider the energetics of adding additional RbI layers to the monolayer structure. We have optimized a double-layer hexagonal RbI structure, in which each adlayer atom in the first layer is coordinated to one of the opposite species in the second layer. This structure is shown below in Figure S8.

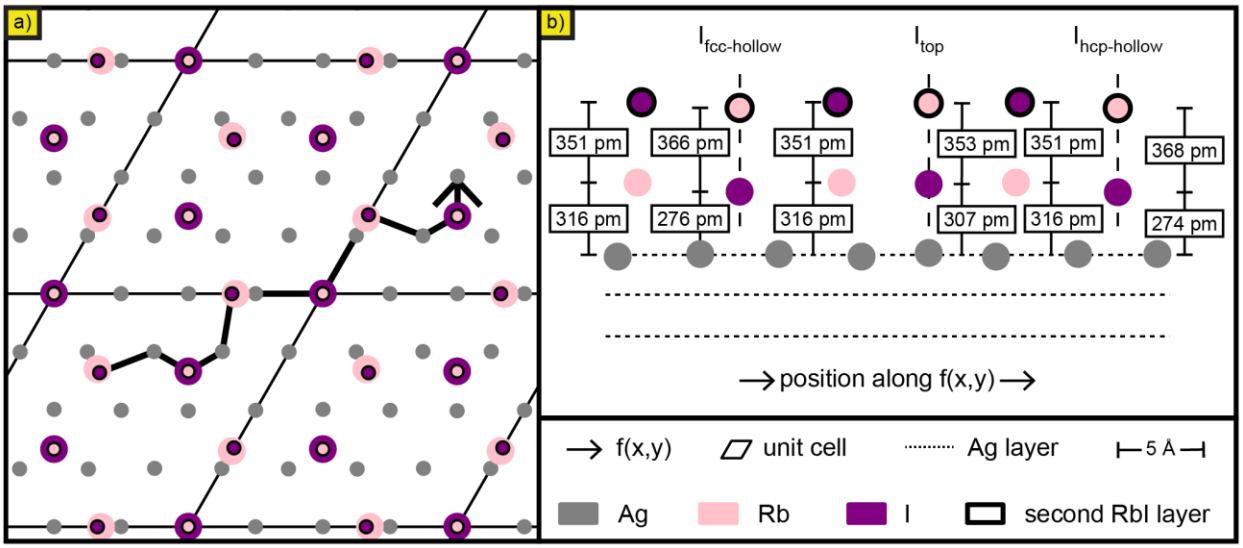

Figure A.8. Atomic model of a double-layer hexagonal RbI structure optimized via DFT, viewed orthogonally to the surface (a) and along the surface (b).

RbI monolayer structure at high surface coverage

Our DFT calculations suggest that the square RbI structure becomes energetically preferable when the density of deposited atoms exceeds the packing density of the hexagonal single-layer structure. This notion is supported by our STM topography of a sample with a high surface coverage of RbI (Figure A.9). Here, we observe a strong preference to form the square structure over the single-layer hexagonal structure.

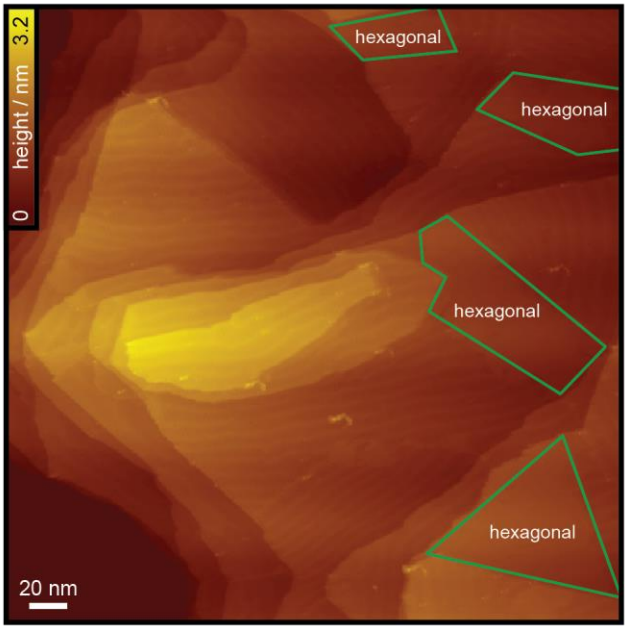

Figure A.9. Characterization of RbI monolayer structure at high adlayer coverage. STM topography (V_b = 2 V, I = 5 pA) showing high surface coverage with a strong preference to form the square phase (everywhere not outlined in green) over the hexagonal phase (outlined in green).

RbI monolayer structure in the presence of Ag step edges

The presence of Ag step edges has a profound impact on the prevalence of hexagonal vs square RbI structures in our STM images. Typically, only the square RbI phase is observed at step edges (Figure A.10). Furthermore, we observe only a single orientation of the square structure, in which the $S_{1\bar{1}0}$ direction is oriented along the step edge (Figure A.10b). When an RbI island is adjacent to two Ag step edges (as in the left side of Figure A.10b), the $S_{1\bar{1}0}$ direction is oriented along the step edge which has the longest shared interface with RbI. Interestingly, the positioning of the moiré pattern relative to the step edge is also consistent between RbI islands. To characterize the position of the moiré pattern, we consider two types of regions in the supercell that are distinguished by their topographic appearance along the L_{short} axis: 1) the topography alternates between light and dark; 2) the topography is consistently bright. This topographic difference originates from the surface-adlayer registry (see main text,

Figure 3.5d), where regions with higher Ag-Rb/I coordination show consistently bright topography along the L_{short} axis. There are two regions in the moiré supercell which show this topographic pattern, and thus could correspond to the preferred positioning of the square RbI structure at Ag step edges where entire rows of iodine or Rb can be situated in the pockets between Ag atoms (Figure A.10c,d). As discussed previously (see discussion of Figure 3.4 in main text, for example), this kind of coordination leads to the strongest substrate-adlayer interactions, resulting in the most favorable binding with the electrostatic environment of the Ag step edge. Thus, the charged environment at step edges leads to a preference for RbI to form the square structure, which is positioned and oriented to maximize favorable electrostatic interactions with the substrate.

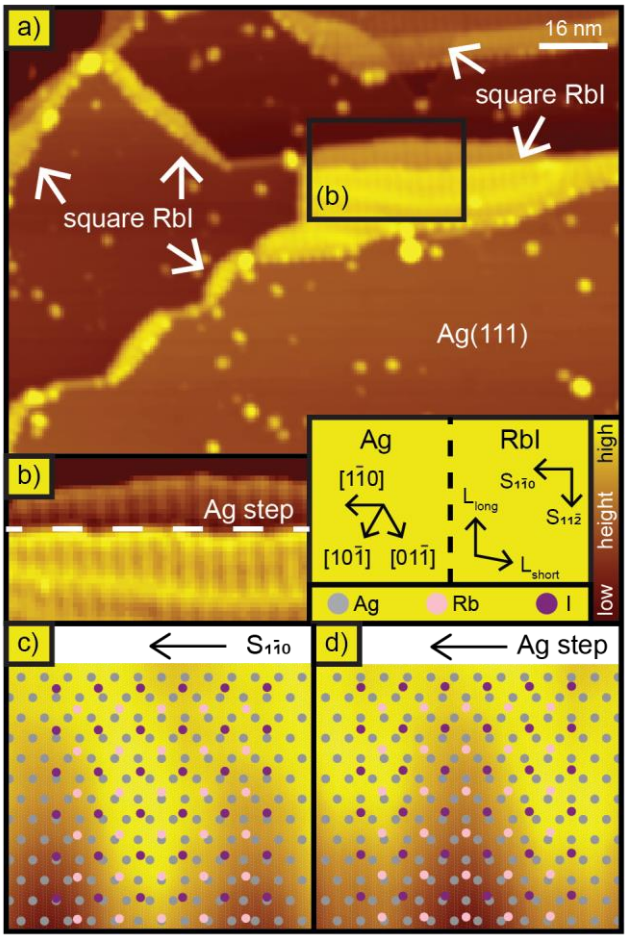

Figure A.10. Characterization of RbI monolayer structure at low adlayer coverage. a) Representative STM topography (V_b = 2 V, I = 5 pA) showing RbI nucleation along Ag step edges. b) STM topography (V_b = 2 V, I = 5 pA) of a square RbI island from (a). c,d) Atomic model of possible adlayer structure at Ag step edges, matching the topography shown in (b). The LDOS map overlaid is identical to that shown in the main text, Figure 3.5d and is integrated from 0.0 to 1.2 eV above the Fermi level and sampled at a height of 12 Å above the surface.

Next, we consider the significance of these findings in discussing the nucleation site of RbI. Importantly, the consistency in the orientation and position of the moiré pattern with respect to Ag step edges suggests that RbI nucleates at the step edge. For example, if the nucleation site were somewhere other than the step edge, we would expect to see variations in the RbI topography at step edges for different RbI islands. Since we observe the same RbI topography at many Ag step edges, the position of the nucleation site relative to the step edge must be consistent. This suggests that RbI preferentially nucleates at Ag step edges.

Interestingly, when the RbI coverage is closer to a full monolayer in coverage, we observe both hexagonal and square structures grown at Ag step edges (Figure A.11). The orientation of the square structure is the same for both sub (Figure A.10) and near-monolayer (Figure A.11) coverage, with the $S_{1\bar{1}0}$ axis oriented along the step edge.

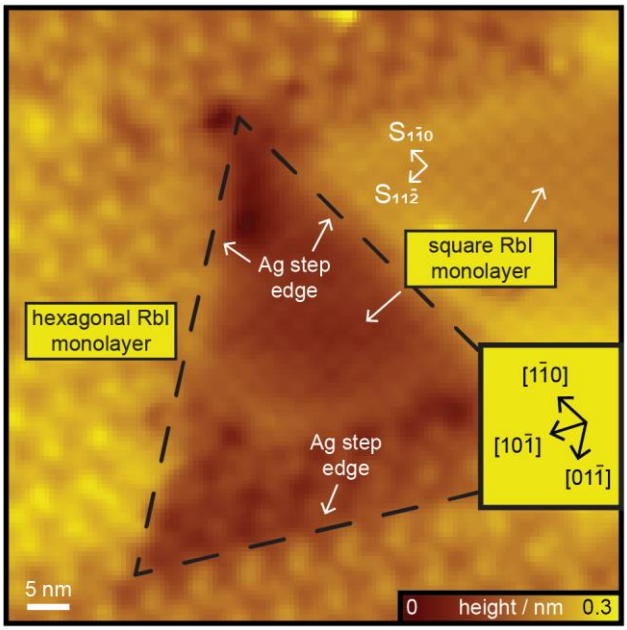

Figure A.11. STM topography (V_b = -200 mV, I = -100 pA) showing coexistence of hexagonal and square RbI structures at Ag step edges. The dashed black line shows the approximate location of the Ag step.

Interpolation of LDOS maps

The tunneling current (I) is proportional to the tip-sample tunneling probability and the number of tip/sample states available to participate in tunneling. Assuming a constant density of states for the tip gives:

$$I(E,r) \propto T(E,r) \times DOS_{sample}(E) \qquad (1)$$

Using the tunneling probability for a general potential barrier, derived by Landau and Lifshitz[5] and presented by Chen[6], gives the tunneling current in terms of the potential shape ($U(r)$), the electron mass (m), and the width of the potential barrier (r_0):

$$I(E,r) \propto DOS_{sample}(E) \times exp\left(\frac{2}{\hbar}\int_0^{r_0}[2m(U(r)-E)]^{1/2}\,dr\right) \qquad (2)$$

We consider the case in which the potential decays linearly between the tip and sample and is related to the bias voltage (V) and the work function (φ):

$$U(r) = \varphi - E - \frac{Vr}{r_0} \qquad (3)$$

Substituting (3) into (2) and solving the integral gives:

$$I(E,r) \propto DOS_{sample}(E) \times exp\left(\frac{\sqrt{32m}r_i}{3\hbar V}\left[(\varphi-E-V)^{3/2}-(\varphi-E)^{3/2}\right]\right) \qquad (4)$$

For compatibility with DFT calculations, it is useful to reference the transmitted eigenenergy to the Fermi energy of the sample, which is done by subtracting V from E. A sum is taken over individual atoms (i) for each spatial point over which the LDOS is mapped. Similarly, a sum is also taken over energies from 0 to V, in order to account for all eigenstates contributing to the tunneling current. This gives Equation 1 from the main text:

$$I(E,r) \propto \sum_i \sum_E^V D_i(E) \times exp\left(-\frac{\sqrt{32m}r_i}{3\hbar V}\left[(\varphi-E+V)^{3/2}-(\varphi-E)^{3/2}\right]\right) \qquad (5)$$

APPENDIX B

SUPPORTING MATERIALS FOR CHAPTER IV

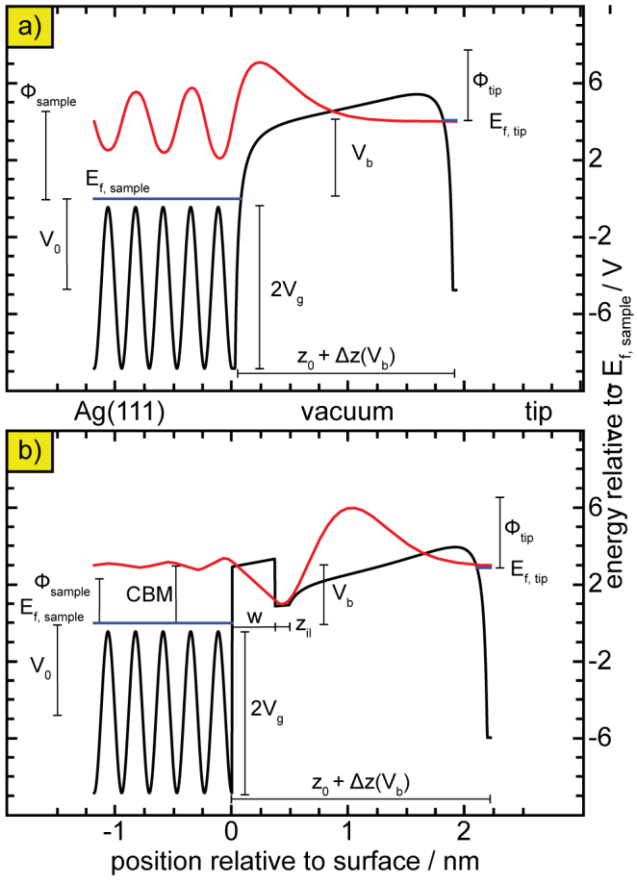

Figure B.1: Representative potential/wavefunction for numerical integration of image potentials states. Potentials (black) and lowest-energy wavefunctions (red) are shown for the bare Ag(111) (a) and hexagonal RbI (b) for the spectra shown in Figure 4.1a. The parameters of the model are overlaid, where E_f indicates the Fermi energy of the tip and sample respectively, V_b is the voltage bias between the tip and sample, z_0 is the tip-sample distance at the initial bias voltage of the scanning tunneling spectroscopy (STS) measurement, Δz is the change in tip-sample distance as the voltage bias is changed during the STS measurement, ϕ is the work function of the tip and sample respectively, R is the radius of the tip in the spherical-tip approximation, w is the width of the RbI monolayer, z_{il}, adjusts the position of the mirror plane relative to the surface, CBM is the conduction band minima of the RbI monolayer, V_0 is the position of the Ag(111) lattice potential relative to the Fermi level of the sample, and V_g determines the amplitude of the lattice potential. The model shown here is similar to that used elsewhere to model image potential states (IPS).[1]

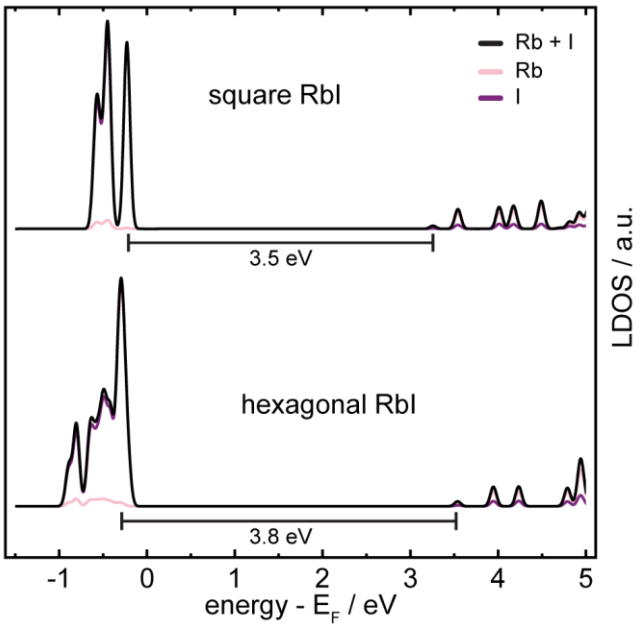

Figure B.2: Comparison of local density of states (LDOS) between isolated square and hexagonal RbI structures. The average LDOS is plotted for a square (top) and hexagonal (bottom) RbI structure, where there is no substrate present. The Rb-I bond length is the average value found in each structure type on Ag(111).

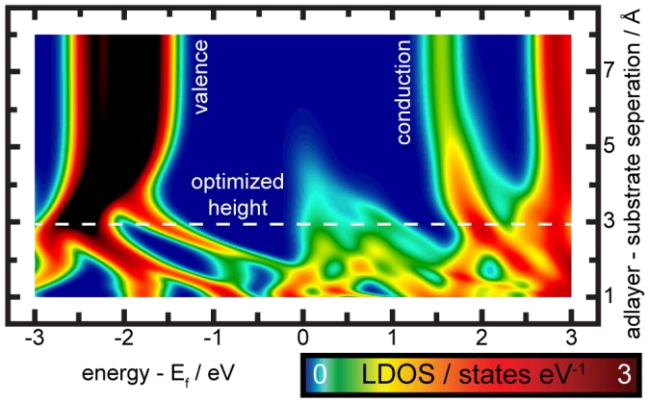

Figure B.3: Effect of substrate interaction on adlayer LDOS. The average LDOS of a hexagonal RbI monolayer is shown for a range of substrate-adlayer distances as calculated by density functional theory (DFT), where the RbI structure is isolated from the substrate at large distances. The DFT-optimized substrate-adlayer height is indicated by the horizontal dashed line.

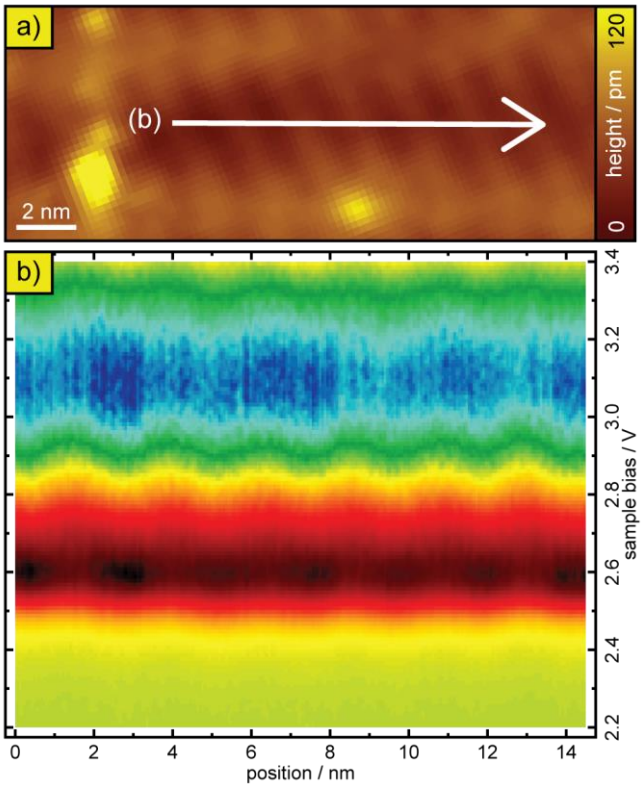

Figure B.4: STS measurements of image potential state (IPS) energy along short moiré axis of square RbI. a) STM topography (V_b = 2 V, I = 5 pA) of square RbI, with path along which STS measurements were taken in (b). b) Progression of STS spectra (V_b = 3.4 V, I = 50 pA, V_{pp} = 40 mV), showing there is not significant modulation of the first IPS energy along the short moiré axis of the square RbI structure.

APPENDIX C

SUPPORTING MATERIALS FOR CHAPTER V

Simulated STM topographies of various RbI vacancy defects

To aid in identifying the point defects observed in the RbI monolayer, we have simulated STM topographies for various RbI vacancy defects using methods described elsewhere.[1] Our results show that the Rb vacancy appears as a depression in STM topography recorded at low bias voltages (see Figure C.1), in agreement with previous findings for other atomic vacancies.[2-4] In contrast, our results show that the iodine vacancy appears as a protrusion in low bias STM topographies (see Figure C.1), which is different than previous results for NaCl, where Cl vacancies appeared as a depression.[2-4]

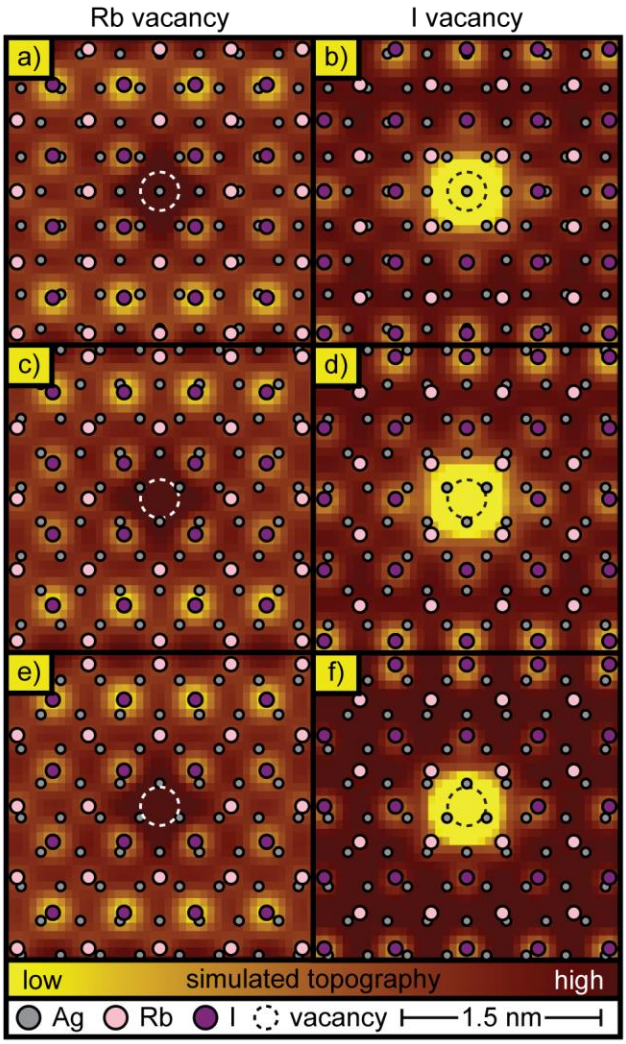

Figure C.1: Simulated STM topographies of RbI vacancy defects using a spatially-dependent local work function. STM topographies are simulated for several different configurations of the Rb and iodine vacancy defects, calculated at a height from the surface of 0.2 nm and integrated from 200 mV below the Fermi level up to the Fermi level, in line with biases used in experimental STM images (Figure 5.2b,c). The registry of different vacancies correspond to: top-site (a,b), fcc-hollow-site (c,d), and hcp-hollow-site (e,f) following the convention for adsorption configurations used previously.[1] The local work function is calculated by modifying the nominal work function of the pristine RbI monolayer structure by the change in potential energy due to the presence of the defect: $\phi(r) = \phi_{pristine\ structure} + (E(r)_{defect\ structure} - E(r)_{pristine\ structure})$.

To understand the origin of this difference in appearance for Cl vs iodine atomic vacancies in STM topography, we have also simulated STM topographies using the average, spatially-independent work function of the pristine RbI structure (Figure C.2). This ignores any

local effects the vacancy-type defects might have on the work function, and thus is a measure of only the morphology and LDOS of the RbI structure. In this version of the simulated topographies, all vacancy-type defects appear as depressions, and we do not observe the presence of both protrusion and depression-type defects as in experiment. Our results suggest that, in order to observe both protrusion-type and depression-type defects as in experiment, it is necessary to account for changes in the local work function at the defect. This distinction in behavior between the NaCl and RbI structures is likely due to differences in the impact of the vacancy defect on the local electrostatic potential, where the RbI structure interacts more significantly with the substrate and thus exhibits a more significant change in potential at the defect than for NaCl.[1]

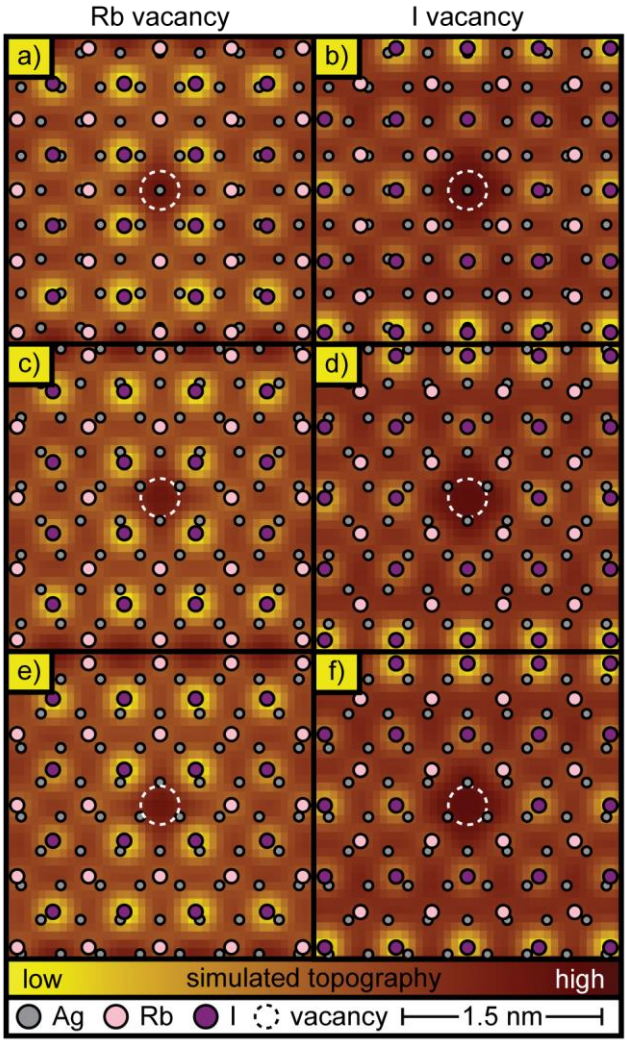

Figure C.2: Simulated STM topographies of RbI vacancy defects using a spatially-independent local work function. STM topographies are simulated for several different configurations of the Rb and iodine vacancy defects, calculated at a height from the surface of 0.2 nm and integrated from 200 mV below the Fermi level up to the Fermi level, in line with biases used in experimental STM images (Figure 5.2b,c). The registry of different vacancies correspond to: top-site (a,b), fcc-hollow-site (c,d), and hcp-hollow-site (e,f) following the convention for adsorption configurations used previously.[1] The work function is the average value of the pristine RbI monolayer structure: $\phi = E_{vacuum\ level} - E_{Fermi}$.

Impact of substrate-adlayer registry on defect potential

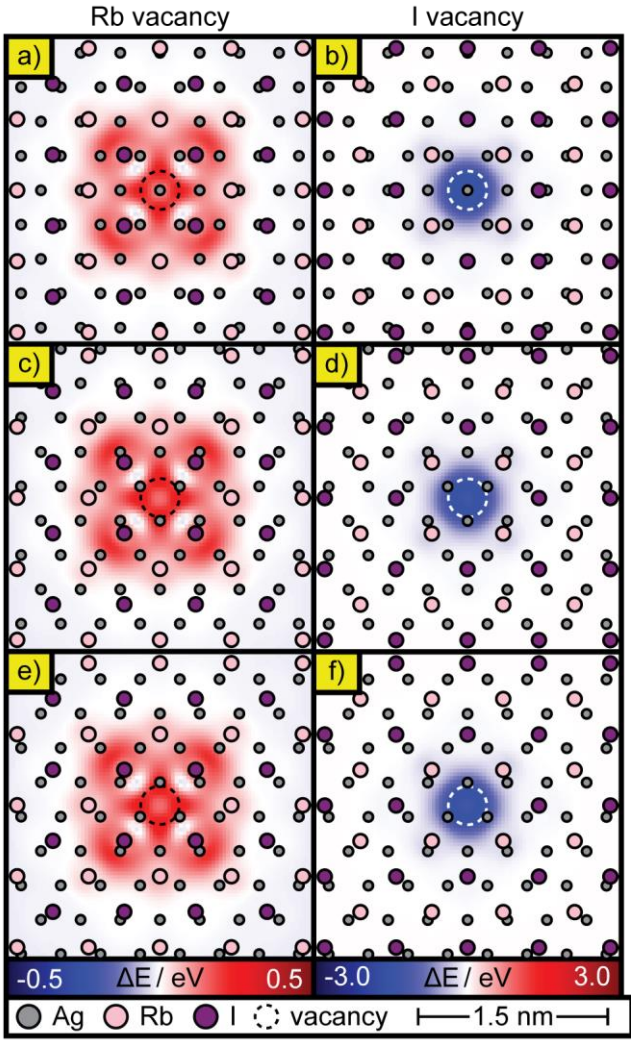

Figure C.3: DFT-calculated differential electron potentials of vacancy defects in the RbI monolayer. The difference in potential due to the presence of a vacancy defect is calculated for various configurations of Rb (a,c,e) and iodine (b,d,f). The registry of different vacancies correspond to: top-site (a,b), fcc-hollow-site (c,d), and hcp-hollow-site (e,f) following the convention for adsorption configurations used previously.[1] The change in potential is calculated as in the main text, Figure 5.5: $\Delta E(r) = E(r)_{defect\ structure} - E(r)_{pristine\ structure}$.

Spatial electrostatic variations in RbI monolayer

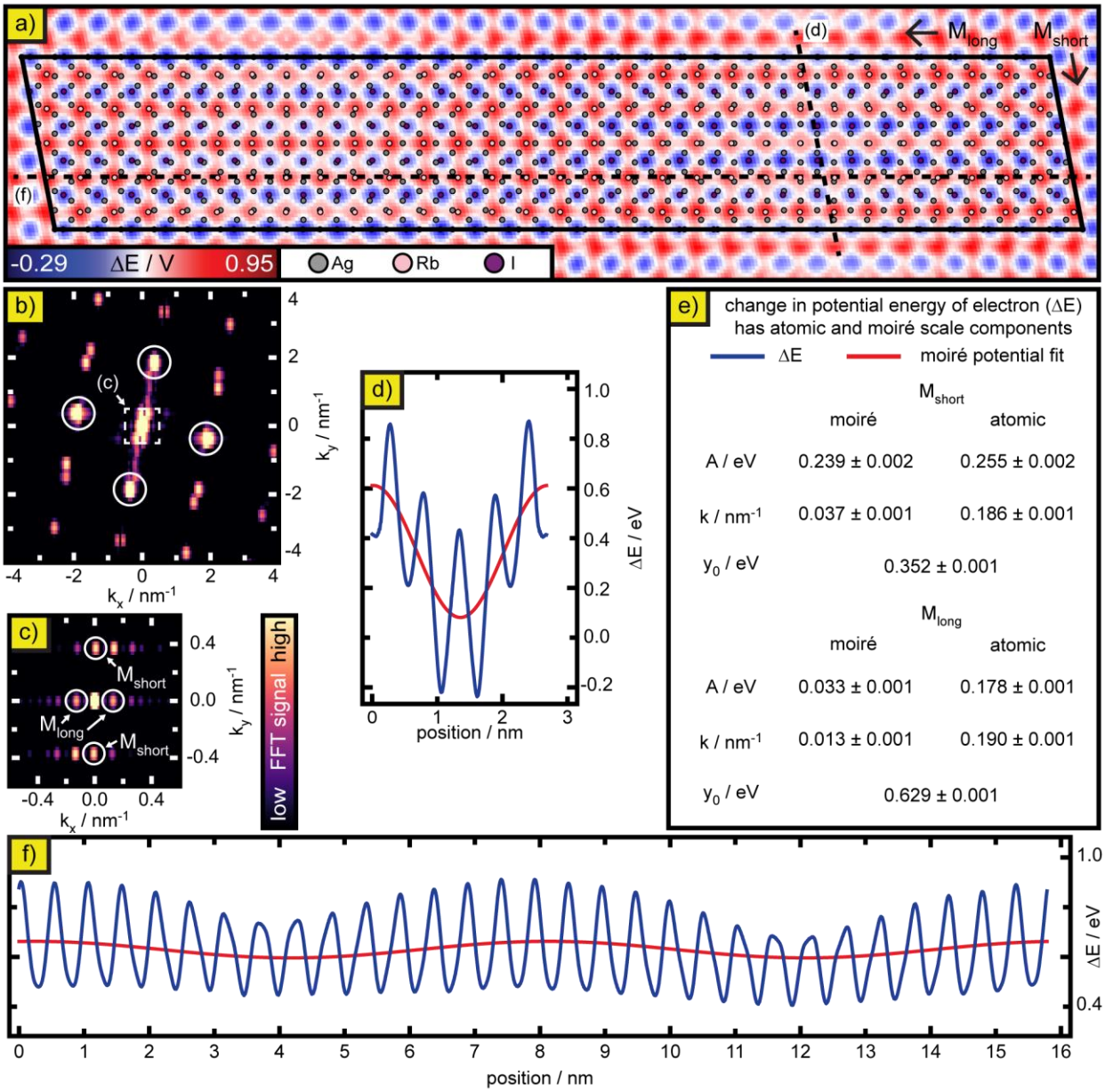

Figure C.4: Spatial variation of DFT-calculated potential for square RbI on Ag(111). a) Change in potential energy of an electron (ΔE) along the top layer of Ag due to adsorption of RbI: $\Delta E(r) = E(r)_{Ag/RbI} - E(r)_{Ag} - E(r)_{RbI}$ b,c) 2D fast Fourier transform of the potential shown in (a). The different momentum ranges show the fast (b) and slow (c) spatial oscillations. d,f) Slices of potential in (a) taken along M_{short} and M_{long} respectively. Each slice shows fast (atomic) and slow (moiré) spatial oscillations, which have been fit to cosine functions. The cosine fit corresponding to the moiré supercell has been overlaid in red. e) Optimized fit parameters for the atomic and moiré oscillations.

Defining a potential using the Mathieu equation

Starting from Schrodinger's equation, we set the potential equal to a cosine with amplitude (A) and spatial frequency (k), where x is our spatial coordinate:

$$\left(\frac{-\hbar^2}{2m}\right)\frac{d\Psi^2}{dx^2} + Acos(2\pi kx)\Psi = E\Psi$$

We rearrange to get:

$$\frac{d\Psi^2}{dx^2} - \left(\frac{2m}{\hbar^2}\right)Acos(2\pi kx)\Psi + \left(\frac{2m}{\hbar^2}\right)E\Psi = 0$$

Next we convert our spatial units from x to r, where $r = \pi kx$:

$$\left(\frac{dr}{dx}\right)^2\left(\frac{d\Psi^2}{dr^2}\right) - \left(\frac{2m}{\hbar^2}\right)Acos(2r)\Psi + \left(\frac{2m}{\hbar^2}\right)E\Psi = 0$$

Simplifying gives the following:

$$\left(\frac{d\Psi^2}{dr^2}\right) - \left(\frac{\sqrt{2m}}{\pi k\hbar}\right)^2 Acos(2r)\Psi + \left(\frac{\sqrt{2m}}{\pi k\hbar}\right)^2 E\Psi = 0$$

From this we can rewrite in the traditional form of the Mathieu differential equation:[5, 6]

$$\left(\frac{d^2}{dr^2} + a - 2qcos(2r)\right)\Psi = 0$$

Where:

$$q = Am\left(\frac{1}{\pi k\hbar}\right)^2$$

and

$$a = 2Em\left(\frac{1}{\pi k\hbar}\right)^2$$

Estimation of effective electron mass for bands calculated from the Mathieu equation

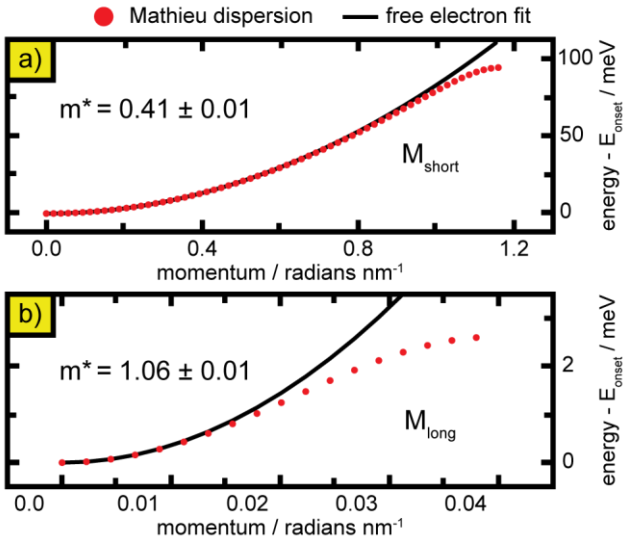

Figure C.5: Dispersion relation of the Mathieu model. The calculated dispersion relation of the onset band is shown for the short (a) and long (b) moiré axis as the red circles. The curvature of each band is determined by a parabolic fit, from which the effective mass is calculated.

APPENDIX D

SUPPORTING MATERIALS FOR CHAPTER VI

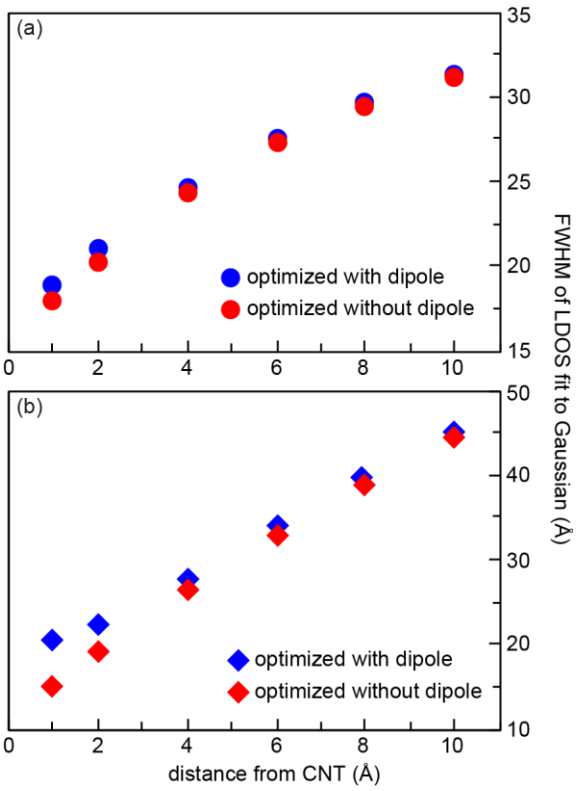

Figure D.1: For dipole interactions resulting in a localization of states (homo-n when the negative charge is closest **(b)** and lumo+n when the positive charge is closest **(a)**), a Gaussian fit was applied the LDOS. The FWHM of the fit functions are compared for (6,5) CNT optimized with and without the presence of a dipole charge pair. This comparison was performed with B3LYP/STO-3G for a (6,5) CNT.

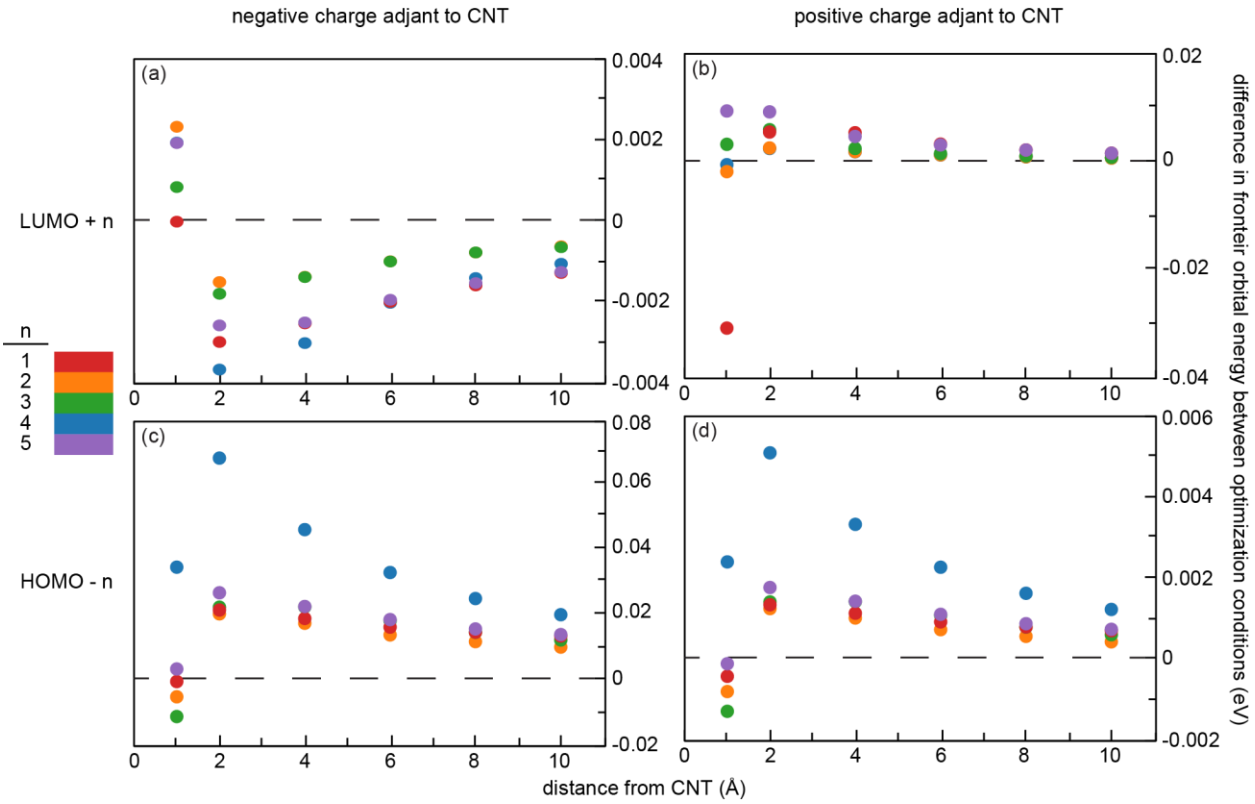

Figure D.2: The difference in energies for frontier molecular orbitals between structures optimized with and without the presence of a dipole is shown. Differences are shown for: a) the five lowest energy unoccupied states with the negative charge adjacent to the CNT b) the five lowest energy unoccupied states with the positive charge adjacent to the CNT c) the five highest energy occupied states with the negative charge adjacent to the CNT d) the five highest energy occupied states with the positive charge adjacent to the CNT. Shown differences correspond to calculations performed with B3LYP/STO-3G for a (6,5) CNT.

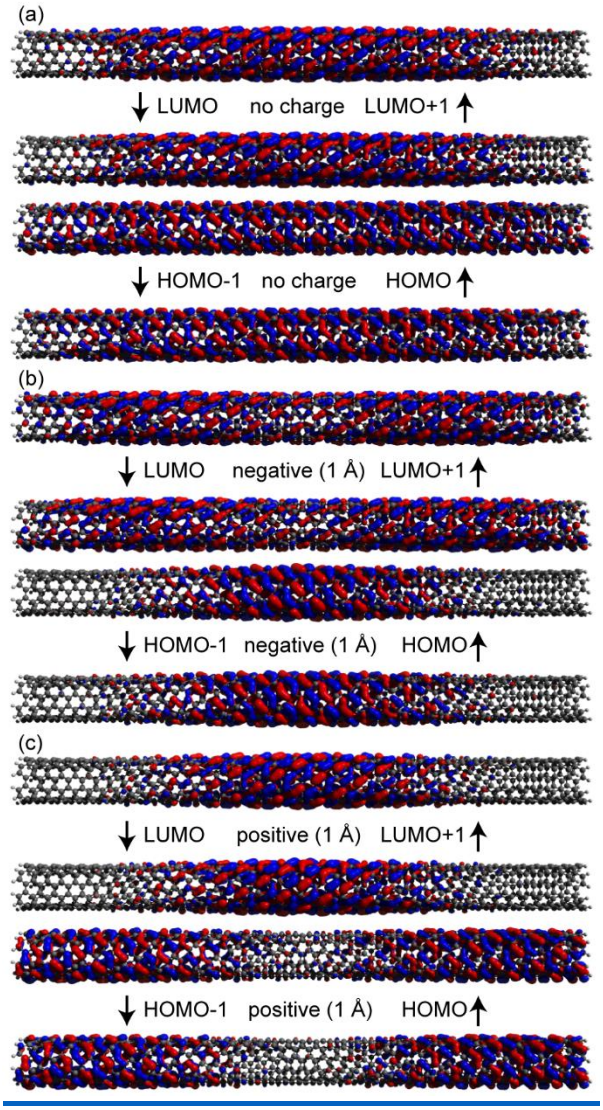

Figure D.3. LUMO+1, LUMO, HOMO, and HOMO-1 of a (6,5) CNT with (a) no external charges, (b) an external dipole as shown in Figure 6.1b with the negative charge 1 Å from the CNT edge, and (c) an external dipole as shown in Figure 6.1b with the positive charge 1 Å from the CNT edge. DFT electronic structure calculated using CAM-B3LYP/STO-3G.

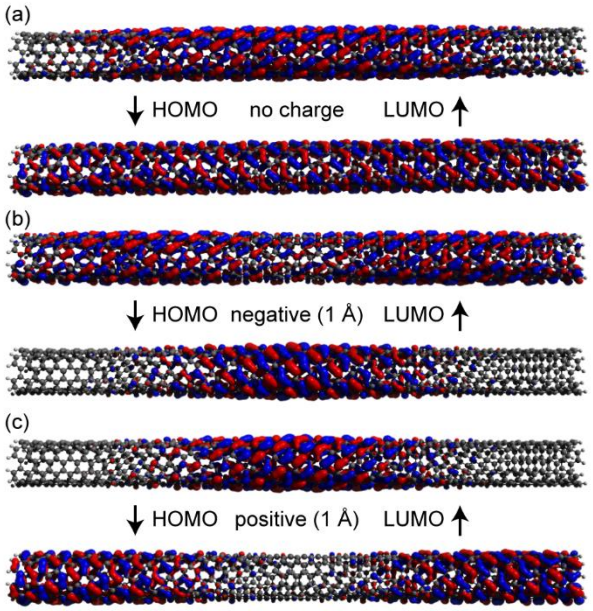

Figure D.4. Frontier molecular orbitals of a (6,5) CNT with (a) no external charges, (b) an external dipole as shown in Figure 6,1b with the negative charge 1 Å from the CNT edge, and (c) an external dipole as shown in Figure 6.1b with the positive charge 1 Å from the CNT edge. DFT electronic structure calculated using B3LYP/STO-3G.

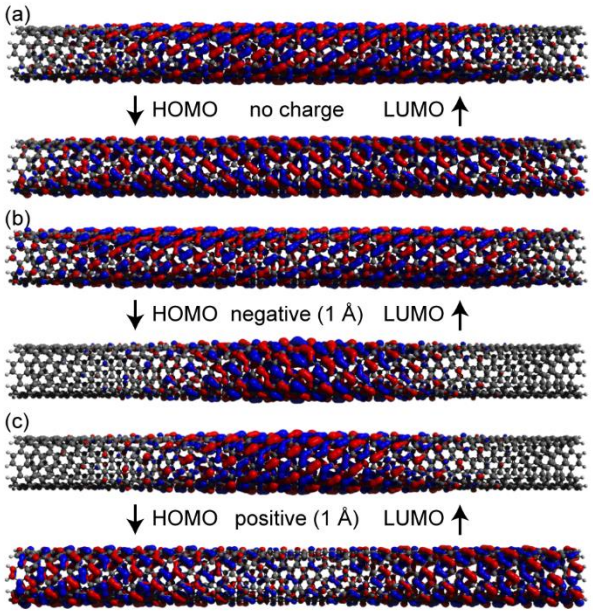

Figure D.5. Frontier molecular orbitals of a (7,6) CNT with (a) no external charges, (b) an external dipole as shown in Figure 6.1b with the negative charge 1 Å from the CNT edge, and (c) an external dipole as shown in Figure 6.1b with the positive charge 1 Å from the CNT edge. DFT electronic structure calculated using CAM-B3LYP/STO-3G.

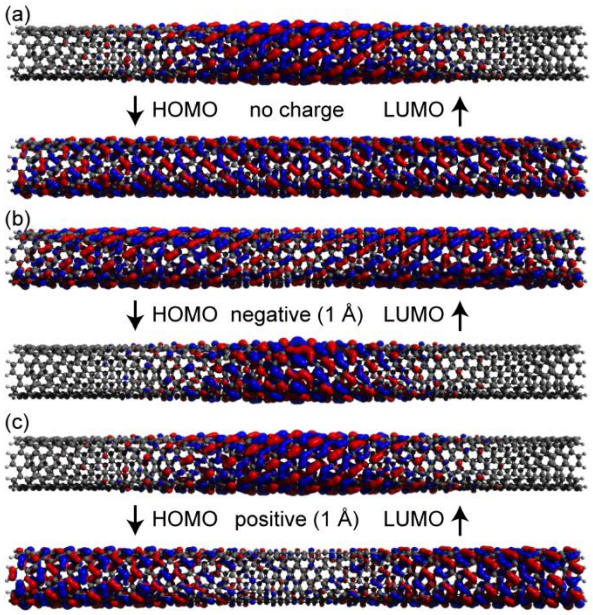

Figure D.6. Frontier molecular orbitals of a (7,6) CNT with (a) no external charges, (b) an external dipole as shown in Figure 6.1b with the negative charge 1 Å from the CNT edge, and (c) an external dipole as shown in Figure 6.1b with the positive charge 1 Å from the CNT edge. DFT electronic structure calculated using B3LYP/STO-3G.

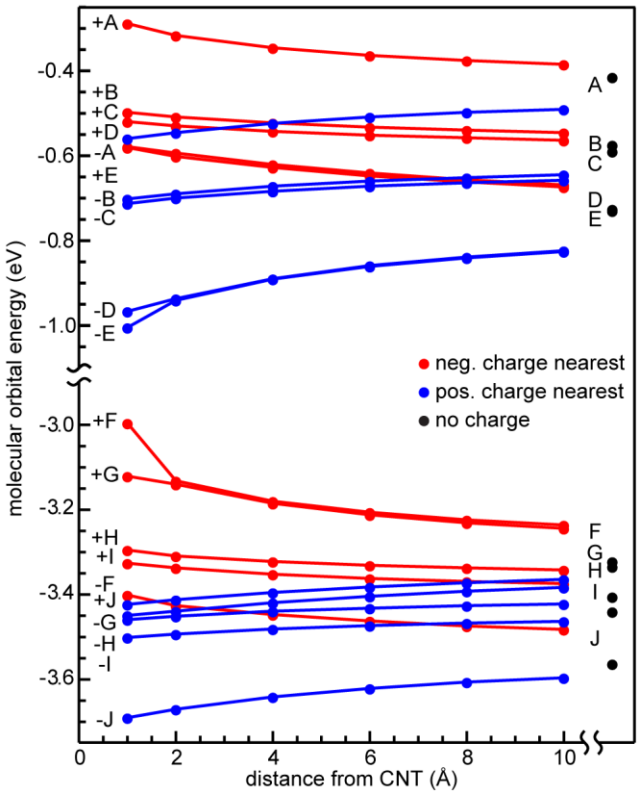

Figure D.7. Calculated molecular orbital energies for the five highest occupied and five lowest unoccupied MOs of a 10 nm-long (7,6) CNT in the presence and absence of an external dipole. DFT electronic structure calculated using CAM-B3LYP/STO-3G.

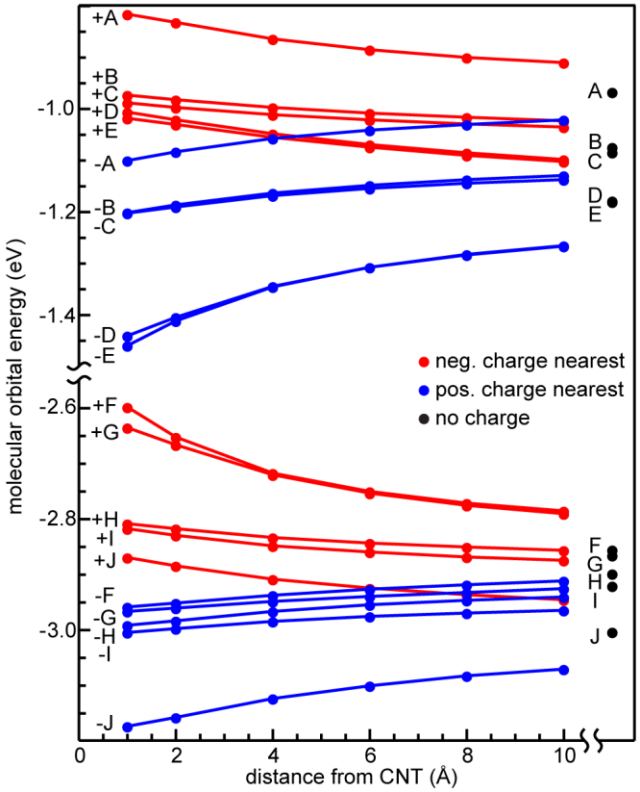

Figure D.8. Calculated molecular orbital energies for the five highest occupied and five lowest unoccupied MOs of a 10 nm-long (6,5) CNT in the presence and absence of an external dipole. DFT electronic structure calculated using B3LYP/STO-3G.

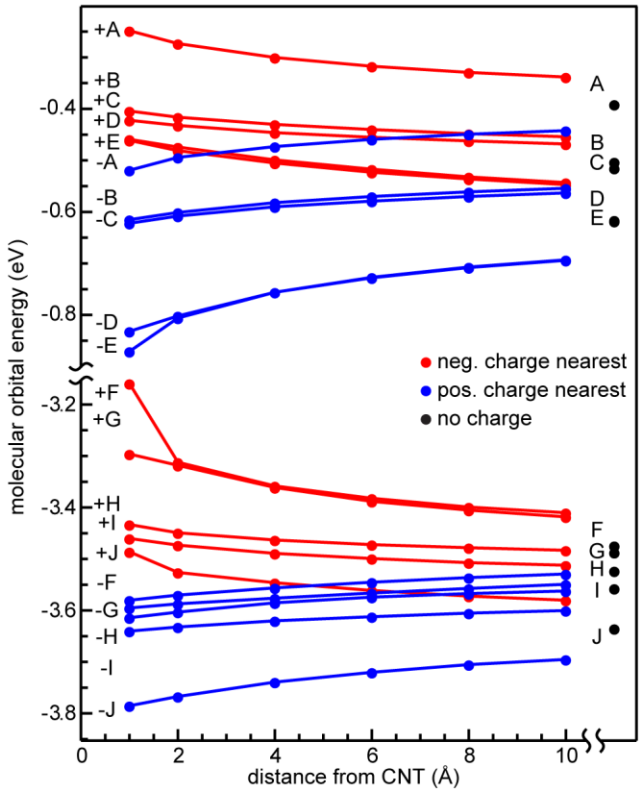

Figure D.9. Calculated molecular orbital energies for the five highest occupied and five lowest unoccupied MOs of a 10 nm-long (7,6) CNT in the presence and absence of an external dipole. DFT electronic structure calculated using B3LYP/STO-3G.

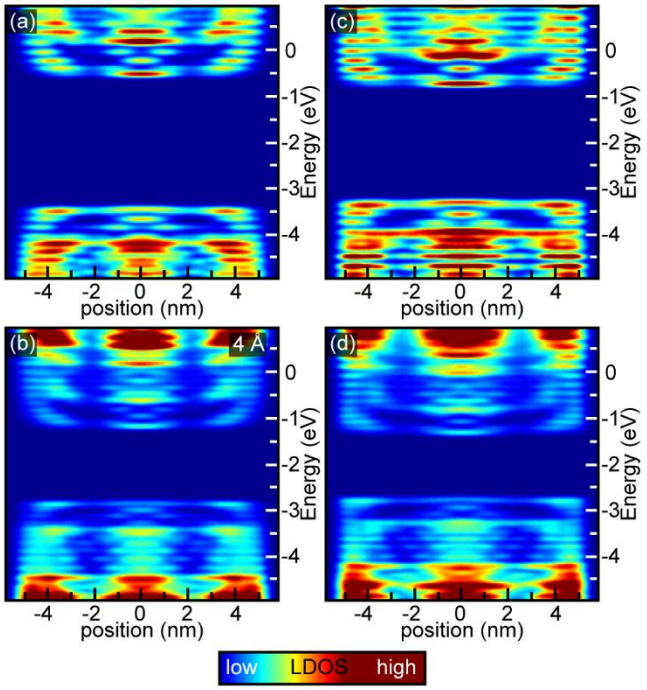

Figure D.10. Plots of LDOS along the center of 10 nm-long CNTs (no external charges). (a, b) (6,5) CNTs and (c, d) (7,6) CNTs with DFT geometries optimized using (a, c) CAM-B3LYP/STO-3G and (b, d) B3LYP/STO-3G, with a LDOS FWHM of 100 meV.

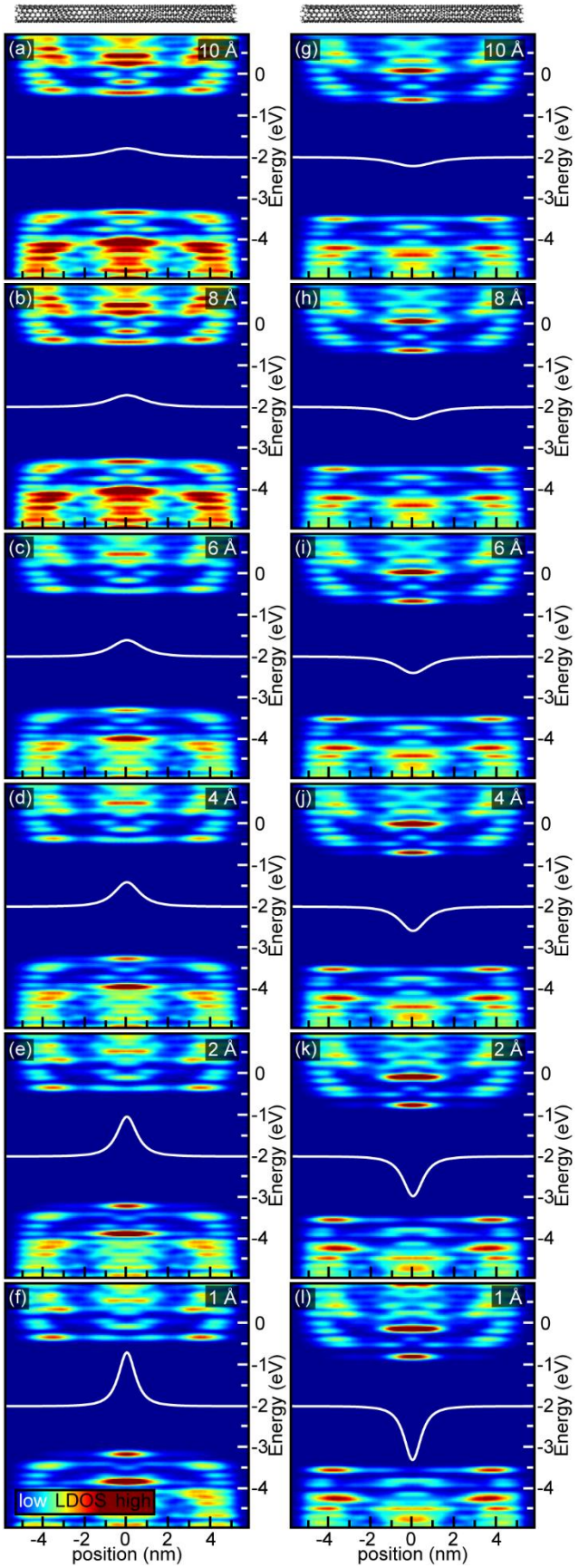

Figure D.11. Extended version of Figure 6.4. Plots of LDOS along the center of a 10 nm-long (6,5) CNT with external dipoles of varying distances, as described in Figure 6.1 of the main text, showing the spatial and energetic impact of the external charges. (a-f) LDOS maps and the electric potential energy (white line, offset by -2 eV) of an electron along the central axis of the CNT due to the external dipole, with the negative charge pair nearest to the CNT at the distance (indicated on each plot) of (a) 10 Å, (b) 8 Å, (c) 6 Å, (d) 4 Å, (e) 2 Å, and (f) 1 Å from the CNT edge. (g-l) same as (a-f) but with the positive charge nearest the CNT. For convenience, CNTs reflecting their spatial extent in the LDOS plots are located above (a) and (g). LDOS calculated using CAM-B3LYP/STO-3G, with a FWHM of 100 meV and 3 Å.

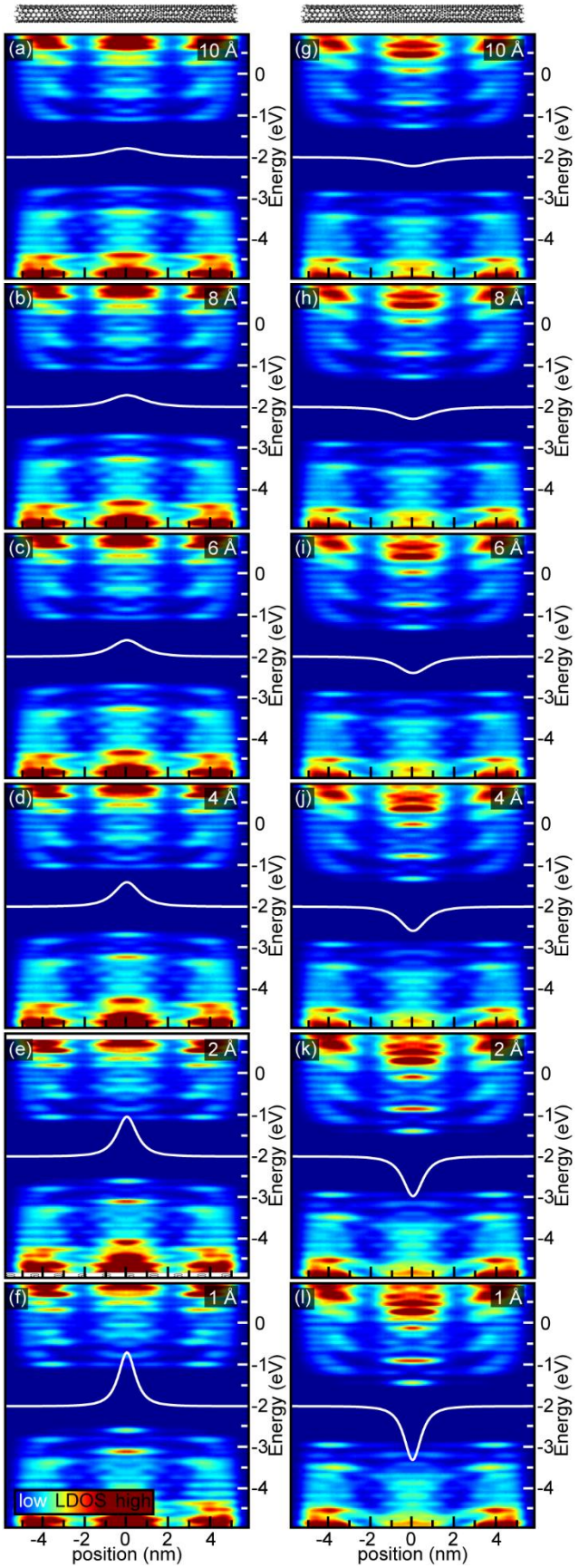

Figure D.12. Plots of LDOS along the center of a 10 nm-long (6,5) CNT with external dipoles of varying distances, as described in Figure 6.1 of the main text, showing the spatial and energetic impact of the external charges. (a-f) LDOS maps and the electric potential energy (white line, offset by -2 eV) of an electron along the central axis of the CNT due to the external dipole, with the negative charge pair nearest to the CNT at the distance (indicated on each plot) of (a) 10 Å, (b) 8 Å, (c) 6 Å, (d) 4 Å, (e) 2 Å, and (f) 1 Å from the CNT edge. (g-l) same as (a-f) but with the positive charge nearest the CNT. For convenience, CNTs reflecting their spatial extent in the LDOS plots are located above (a) and (g). LDOS calculated using B3LYP/STO-3G, with a FWHM of 100 meV and 3 Å.

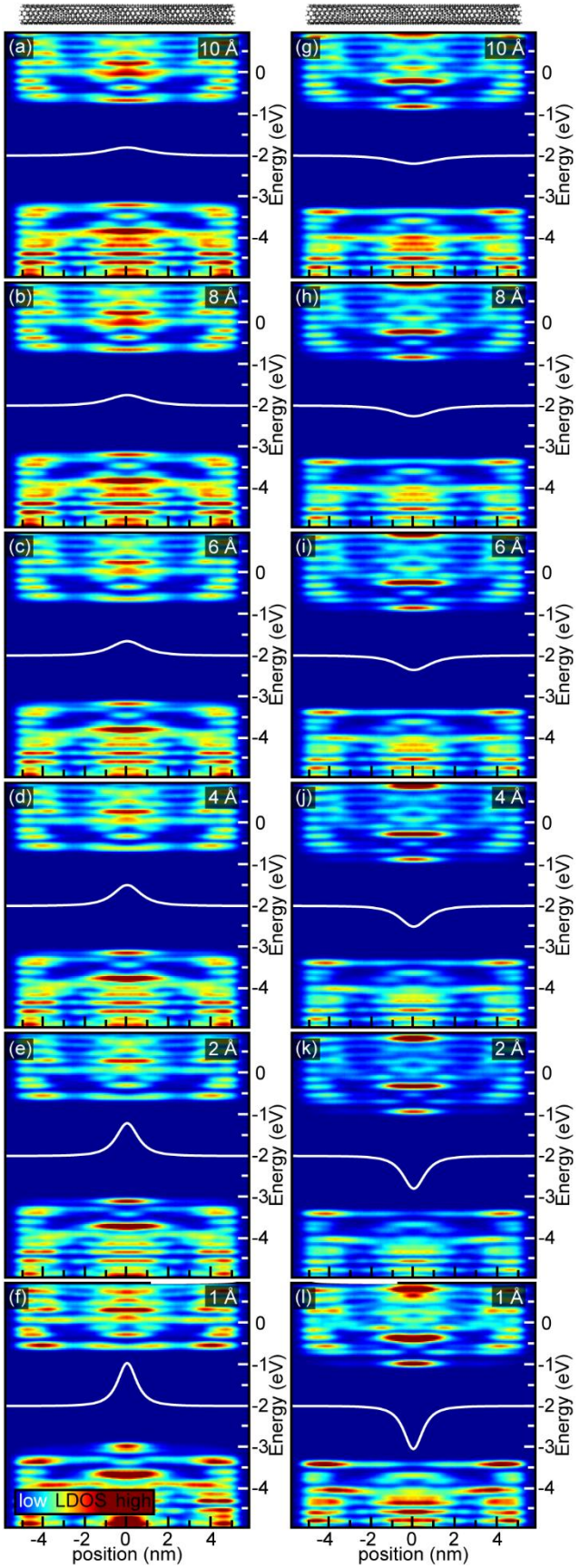

Figure D.13. Plots of LDOS along the center of a 10 nm-long (7,6) CNT with external dipoles of varying distances, as described in Figure 6.1 of the main text, showing the spatial and energetic impact of the external charges. (a-f) LDOS maps and the electric potential energy (white line, offset by -2 eV) of an electron along the central axis of the CNT due to the external dipole, with the negative charge pair nearest to the CNT at the distance (indicated on each plot) of (a) 10 Å, (b) 8 Å, (c) 6 Å, (d) 4 Å, (e) 2 Å, and (f) 1 Å from the CNT edge. (g-l) same as (a-f) but with the positive charge nearest the CNT. For convenience, CNTs reflecting their spatial extent in the LDOS plots are located above (a) and (g). LDOS calculated using CAM-B3LYP/STO-3G, with a FWHM of 100 meV and 3 Å.

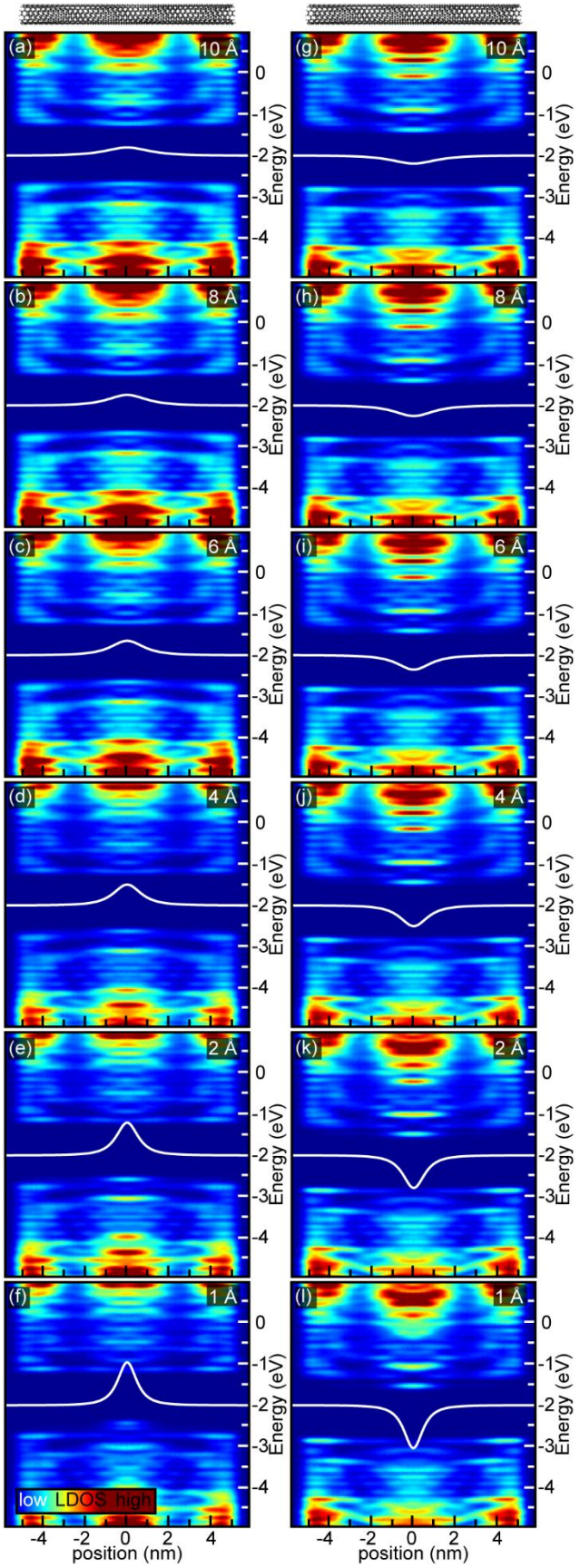

Figure D.14. Plots of LDOS along the center of a 10 nm-long (7,6) CNT with external dipoles of varying distances, as described in Figure 6.1 of the main text, showing the spatial and energetic impact of the external charges. (a-f) LDOS maps and the electric potential energy (white line, offset by 2 eV) of an electron along the central axis of the CNT due to the external dipole, with the negative charge pair nearest to the CNT at the distance (indicated on each plot) of (a) 10 Å, (b) 8 Å, (c) 6 Å, (d) 4 Å, (e) 2 Å, and (f) 1 Å from the CNT edge. (g-l) same as (a-f) but with the positive charge nearest the CNT. For convenience, CNTs reflecting their spatial extent in the LDOS plots are located above (a) and (g). LDOS calculated using B3LYP/STO-3G, with a FWHM of 100 meV and 3 Å.

APPENDIX E

SUPPORTING MATERIALS FOR CHAPTER VII

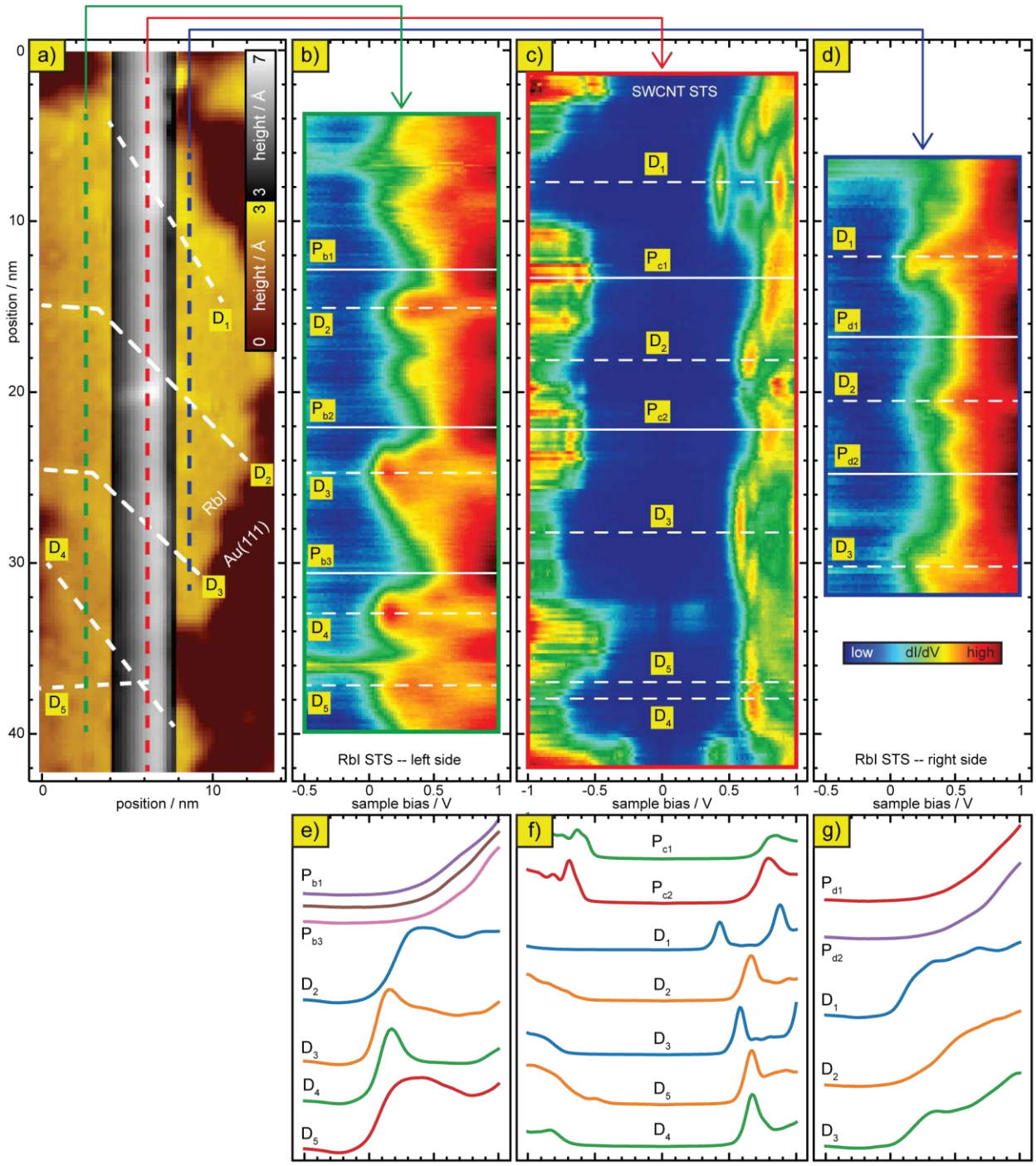

Figure E.1: STS measurements of LDOS variation along SWCNT. a) STM topography (V_b = 1 V, I = 2 pA) of an SWCNT on RbI/Au(111). The white dashed lines indicate the position of linear defects (D_1 – D_5) in the RbI monolayer. The black dashed lines show the path of STS measurements. b-d) STS measurements along SWCNT, recorded to the left of (b), on top of (c),

and to the right of (d). The horizontal white dashed lines show the position of linear defects in each STS measurement. e,f,g) Individual STS spectra from significant spatial locations in the progressions of STS spectra shown in b-d.

SWCNT Point Defects

In addition to the substrate-induced localized states in the SWCNT, we also observe SWCNT states that can be attributed to point defects in the nanotube. One such example is a Stone-Wales (SW) defect, which we identify by the presence of two localized mid-gap states centered around the Fermi level (Figure S2b).[1] Furthermore, we are able to confirm the presence of this SW defect by healing it via a voltage pulse (~3 V) from the STM tip, which can be visualized as the difference in STS spectra between Figure S2b and Figure S2c, and is in agreement with reports of SW defect manipulation by STM in other studies.[2, 3] By identifying this SW defect, it is clear that the LDOS features we discuss in the main text cannot be attributed to an SW defect due to their distinctly different LDOS behavior. Similarly, the LDOS variations discussed in the main text cannot be attributed to other point defects, like SWCNT atomic vacancy defects, which previous studies have shown would exhibit sharp LDOS features near the Fermi level,[1, 4] in contrast to what we observe in experiment.

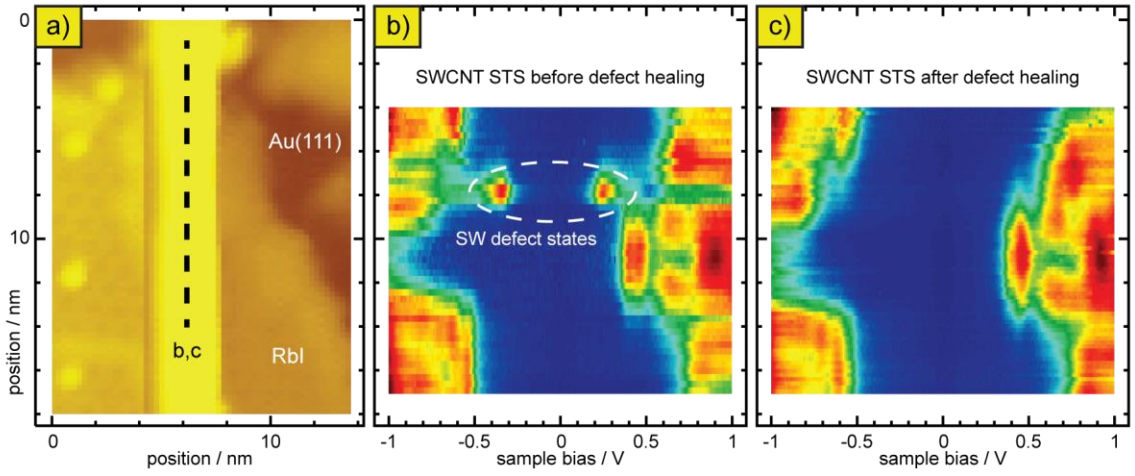

Figure E.2: STS measurements of LDOS variation along SWCNT. a) STM topography (V_b = 1 V, I = 2 pA) of an SWCNT on RbI/Au(111). The black dashed line shows the path of STS

measurements in b,c. b,c) STS measurements taken along the top of a SWCNT, recorded before (b) and after (c) the healing of a Stone-Wales defect in the SWCNT.

High contrast version of STM topography of linear RbI defects

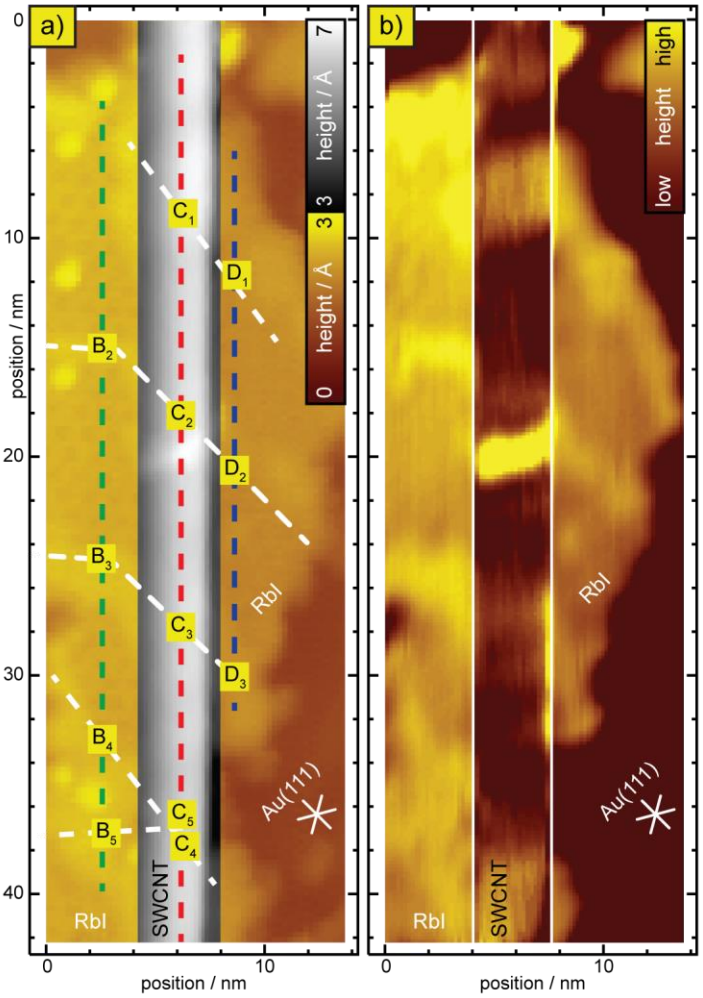

Figure E.3: High contrast STM topography of SWCNT adsorbed across RbI linear defects. a) STM topography (V_b = 1 V, I = 2 pA) of an SWCNT on RbI/Au(111). b) High-contrast version of (a), which highlights the linear RbI defects.

Alignment of DFT-calculated structures to experimental STM image

To characterize the atomic structure of the grain boundary defects (GBDs) in RbI, we begin by finding the structural discontinuity between the two adjacent phases of RbI which, in Figure S4 corresponds to one Au lattice spacing. This discontinuity is identical for both narrow

and wide regions of the defect, with the difference between the two being one additional unit cell of space between adjacent domains. We find that our DFT-calculated structure (see Figure S4) aligns well with the STM topography on either side of the defect, and the STM topography at the defect (bright, raised regions in Figure S4) follows from the electrostatic behavior of the defect (see main text, Figure 4 and Supporting Information, Figure S4), where higher LDOS leads to more tunneling current at the defect.

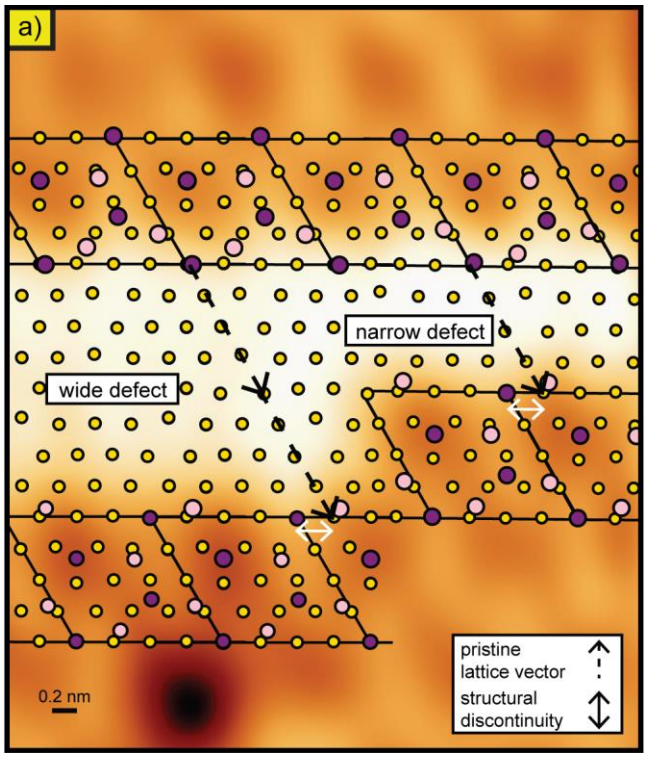

Figure E.4: Alignment of DFT-calculated RbI structure to experiment. The DFT-calculated structure of pristine RbI is overlaid on an experimental STM topography (V_b = 1 V, I = 5 pA), showing the structural discontinuity between adjacent RbI phases for both narrow and wide regions of a grain boundary defect in RbI.

Calculation of structure and electronic potential for 'wide' RbI grain boundary defect

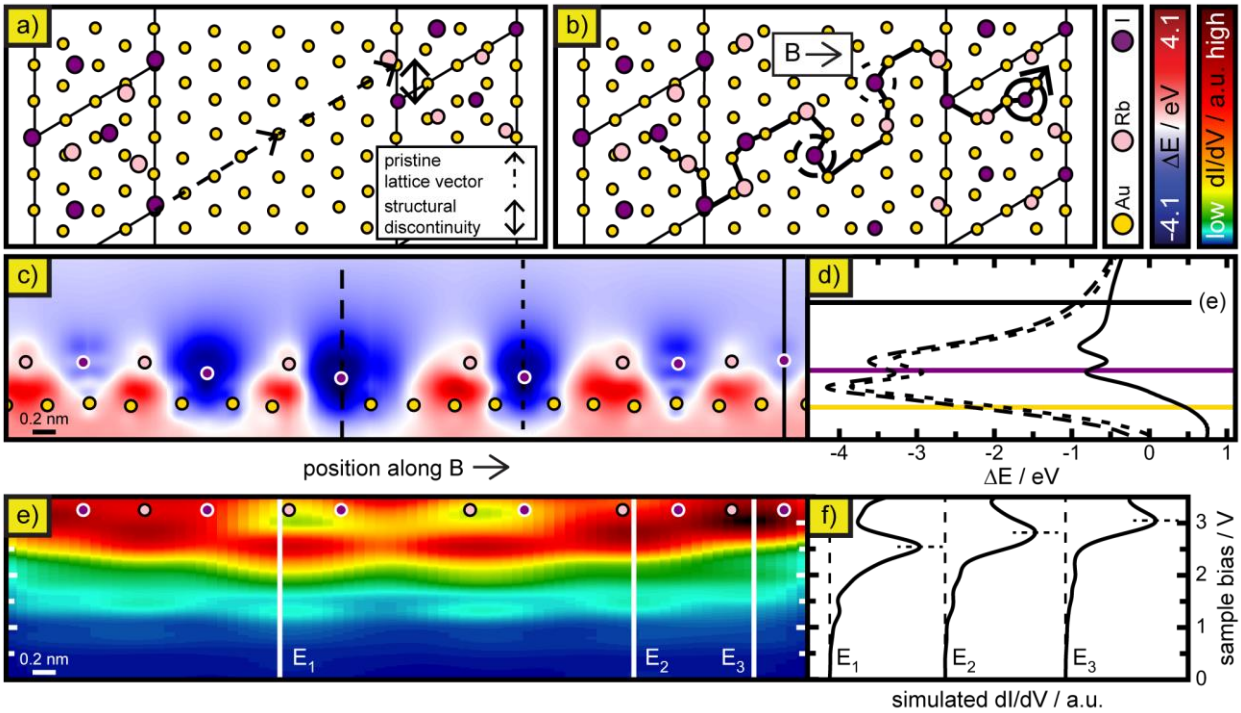

Figure E.5: DFT-calculated electronic potential changes at 'wide' RbI GBD. a,b) DFT-optimized atomic models of 'wide' GBD in an RbI monolayer. The structural discontinuity between two adjacent RbI phases is highlighted in (a), with the dashed arrow showing the propagation of the pristine lattice vector from the left-side domain and the discontinuity shown as the vertical double-arrow. In (b), three RbI molecules per unit cell are added to bridge the empty region between discontinuous phases. The path along which potential energy (c) and simulated STS (e) are taken is indicated by the arrow. c) DFT-calculated change in potential due to RbI-Au interaction is shown in the direction orthogonal to the surface, and is sliced along the path shown in b. d) Change in electronic potential due to RbI-Au interaction sliced at the position of specific iodine atoms, indicated by the circles in b and the vertical lines in c. The horizontal lines show the average position of Au (gold), iodine (purple), and the height at which the STS measurement is simulated (e). e) Simulated STS measurement at a height of 0.5 nm above the surface, taken along the path shown in (b). f) Individual simulated STS spectra, taken from the position of the vertical lines shown in (e).

Calculation of RbI binding preference on fcc vs reconstructed Au

It is well known that it is energetically favorable for the nominally fcc Au(111) surface to reconstruct, resulting in a structure that varies spatially between fcc and hcp character.[5] To understand how the presence of RbI affects this energetic preference, we have performed DFT calculations for monolayer RbI on both pristine fcc and reconstructed Au(111) surfaces. This

was done by building a reconstructed Au surface[5] with dimensions of 4 x 44 Au interatomic spacings, which is commensurate with the hexagonal RbI structure observed here. The pristine fcc Au surface had dimensions of 4 x 4 Au interatomic spacings, and we used a 1 x 11 k-point grid to model the electronic structure at a similar level as for the reconstructed surface. We found that one layer of Au was insufficient to describe charge transfer interactions at the Au/RbI interface, and so two layers of Au atoms were used in each structure.

The results for the DFT-calculated binding preference of RbI on both pristine fcc and reconstructed Au(111) surfaces is shown below in Table E.1. Our results show that the preference of RbI to bind to fcc Au is stronger than the energy gained by allowing Au to reconstruct, indicating that it is energetically preferable (by 0.15 eV nm^{-2}) for monolayer RbI to grow on pristine fcc Au surfaces. This finding is in agreement with our STM images, where we do not observe reconstruction effects underneath RbI.

	reconstructed Au	fcc Au	calculation
energy of substrate + adlayer / eV	-1379.128	-121.645	from DFT
energy of substrate / eV	-1196.278	-104.509	from DFT
energy of adlayer / eV	-161.690	-14.622	from DFT
unit cell area / nm^2	13.687	1.244	from DFT
binding energy / eV nm^{-2}	-1.545	-2.019	$E_{substrate/adlayer} - E_{substrate} - E_{adlayer}$

planar density of Au in top layer / atoms nm^{-2}	13.442	12.858	from DFT
energy of reconstruction / eV per Au atom	-0.024	0	from literature[5]
Reconstruction energy / eV nm^{-2}	-0.322	0	$\frac{energy\ of\ recontruction\ per\ Au\ atom}{planar\ density\ of\ Au\ atoms}$
Binding + reconstruction energy / eV nm^{-2}	-1.868	-2.019	$E_{binding} + E_{recontruction}$

Table E.1: DFT-calculated results for RbI adsorption. Various raw and calculated values are shown which were used to calculate the binding preference of RbI on reconstructed vs fcc Au surfaces. For calculated values, the equations used are indicated in the right-most column.

REFERNCES CITED

REFERENCES CITED FOR CHAPTER I

1. Myny, K. The development of flexible integrated circuits based on thin-film transistors. *Nat. Electron.***2018,** *1* (1), 30-39.

2. Sirringhaus, H. 25th Anniversary Article: Organic Field-Effect Transistors: The Path Beyond Amorphous Silicon. *Adv. Mater.* **2014,** *26* (9), 1319-1335.

3. Khan, Y.; Thielens, A.; Muin, S.; Ting, J.; Baumbauer, C.; Arias, A. C. A New Frontier of Printed Electronics: Flexible Hybrid Electronics. *Adv. Mater.* **2020,** *32* (15), 1905279-1905279.

4. Schwierz, F. Graphene transistors. *Nat. Nanotechnol.* **2010,** *5* (7), 487-496.

5. Illarionov, Y. Y.; Knobloch, T.; Jech, M.; Lanza, M.; Akinwande, D.; Vexler, M. I.; Mueller, T.; Lemme, M. C.; Fiori, G.; Schwierz, F.; Grasser, T. Insulators for 2D nanoelectronics: the gap to bridge. *Nat. Comm.* **2020,** *11* (1), 1-15.

6. Tan, C.; Cao, X.; Wu, X. J.; He, Q.; Yang, J.; Zhang, X.; Chen, J.; Zhao, W.; Han, S.; Nam, G. H.; Sindoro, M.; Zhang, H. Recent Advances in Ultrathin Two-Dimensional Nanomaterials. *Chem. Rev.* **2017,** *117* (9), 6225-6331.

7. Novoselov, K. S.; Mishchenko, A.; Carvalho, A.; Castro Neto, A. H. 2D materials and van der Waals heterostructures. *Science* **2016,** *353* (6298).

8. Wang, Q. H.; Kalantar-Zadeh, K.; Kis, A.; Coleman, J. N.; Strano, M. S. Electronics and optoelectronics of two-dimensional transition metal dichalcogenides. *Nat. Nanotechnol.* **2012,** *7* (11), 699-712.

9. Weiss, N. O.; Zhou, H.; Liao, L.; Liu, Y.; Jiang, S.; Huang, Y.; Duan, X.; Duan, X.; Zhou, H.; Liao, L.; Jiang, S.; Huang, Y.; Weiss, N. O.; Liu, Y. Graphene: An Emerging Electronic Material. *Adv. Mater.* **2012,** *24* (43), 5782-5825.

10. Walsh, M. A.; Hersam, M. C. Atomic-Scale Templates Patterned by Ultrahigh Vacuum Scanning Tunneling Microscopy on Silicon. *Annu. Rev. Phys. Chem.* **2009,** *60*, 193-216.

11. Fischer, S. A.; Isborn, C. M.; Prezhdo, O. V. Excited states and optical absorption of small semiconducting clusters: Dopants, defects and charging. *Chem. Sci.* **2011,** *2* (3), 400-406.

12. Bechstedt, F.; Scheffler, M. Alkali adsorption on GaAs(110): atomic structure, electronic states and surface dipoles. *Surf. Sci. Rep.* **1993,** *18* (5-6), 145-198.

13. Castro Neto, A. H.; Guinea, F.; Peres, N. M. R.; Novoselov, K. S.; Geim, A. K. The electronic properties of graphene. *Rev. Mod. Phys.* **2009,** *81* (1), 109-162.

14. Geim, A. K. Graphene: Status and prospects. *Science* **2009,** *324* (5934), 1530-1534.

15. Li, Y. Carbon Nanotube Research in Its 30th Year. *ACS Nano* **2021,** *15* (6), 9197-9200.

16. Mélinon, P. Vitreous Carbon, Geometry and Topology: A Hollistic Approach. *Nanomater.* **2021,** *11* (7), 1694-1694.

17. Illarionov, Y. Y.; Banshchikov, A. G.; Polyushkin, D. K.; Wachter, S.; Knobloch, T.; Thesberg, M.; Mennel, L.; Paur, M.; Stöger-Pollach, M.; Steiger-Thirsfeld, A.; Vexler, M. I.; Waltl, M.; Sokolov, N. S.; Mueller, T.; Grasser, T. Ultrathin calcium fluoride insulators for two-dimensional field-effect transistors. *Nature Electronics 2019 2:6* **2019,** *2* (6), 230-235.

18. Li, W.; Zhou, J.; Cai, S.; Yu, Z.; Zhang, J.; Fang, N.; Li, T.; Wu, Y.; Chen, T.; Xie, X.; Ma, H.; Yan, K.; Dai, N.; Wu, X.; Zhao, H.; Wang, Z.; He, D.; Pan, L.; Shi, Y.; Wang, P.; Chen, W.; Nagashio, K.; Duan, X.; Wang, X. Uniform and ultrathin high-κ gate dielectrics for two-dimensional electronic devices. *Nat. Electron.* **2019,** *2* (12), 563-571.

19. Pivetta, M.; Patthey, F.; Stengel, M.; Baldereschi, A.; Schneider, W. D. Local work function Moiré pattern on ultrathin ionic films: NaCl on Ag(100). *Physical Review B* **2005,** *72* (11), 115404-115404.

20. Zhang, Z.; Hu, J.; Yang, P.; Pan, S.; Quan, W.; Li, N.; Zhu, L.; Zhang, Y. Modulating the periods and electronic properties of striped moiré superstructures for monolayer WSe2 on Au(100) by varied interface coupling. *Nanoscale* **2022,** *14* (20), 7720-7728.

21. Piquero-Zulaica, I.; Lobo-Checa, J.; El-Fattah, Z. M. A.; Ortega, J. E.; Klappenberger, F.; Auwärter, W.; Barth, J. V. Engineering quantum states and electronic landscapes through surface molecular nanoarchitectures. *Rev. Mod. Phys.* **2022,** *94* (4), 045008-045008.

22. Kolpatzeck, K.; Brendel, L.; Möller, R.; Robles, R.; Lorente, N. Paradoxical effects for a one-dimensional periodic potential embedded in a two-dimensional system. *Phys. Rev. B* **2023,** *107* (15), 155418-155418.

23. Xiao, Y.; Liu, J.; Fu, L. Moiré is More: Access to New Properties of Two-Dimensional Layered Materials. *Matter* **2020,** *3* (4), 1142-1161.

24. Lopes Dos Santos, J. M. B.; Peres, N. M. R.; Castro Neto, A. H. Graphene bilayer with a twist: Electronic structure. *Phys. Rev. Lett.* **2007,** *99* (25), 256802-256802.

25. Zhang, Q.; Yu, J.; Ebert, P.; Zhang, C.; Pan, C. R.; Chou, M. Y.; Shih, C. K.; Zeng, C.; Yuan, S. Tuning Band Gap and Work Function Modulations in Monolayer hBN/Cu(111) Heterostructures with Moiré Patterns. *ACS Nano* **2018,** *12* (9), 9355-9362.

26. Huang, D.; Choi, J.; Shih, C. K.; Li, X. Excitons in semiconductor moiré superlattices. *Nat. Nanotechnol.* **2022,** *17* (3), 227-238.

27. Hong, X.; Kim, J.; Shi, S. F.; Zhang, Y.; Jin, C.; Sun, Y.; Tongay, S.; Wu, J.; Zhang, Y.; Wang, F. Ultrafast charge transfer in atomically thin MoS2/WS2 heterostructures. *Nat. Nanotechnol.* **2014,** *9* (9), 682-686.

28. Bian, K.; Gerber, C.; Heinrich, A. J.; Müller, D. J.; Scheuring, S.; Jiang, Y. Scanning probe microscopy. *Nat. Rev. Methods Primers* **2021,** *1* (1), 1-29.

REFERENCES CITED FOR CHAPTER II

1. Hackley, J. D.; Kislitsyn, D. A.; Beaman, D. K.; Ulrich, S.; Nazin, G. V. High-stability cryogenic scanning tunneling microscope based on a closed-cycle cryostat. *Rev. Sci. Instrum*. **2014,** *85* (10), 103704.

2. Taber, B. N.; Neill, M. L.; Thom, T. N.; Clapp, O. D.; Lee, J. In situ plasmonic tip preparation and validation techniques for scanning tunneling microscopy. *J. Vac. Sci. Technol. A* **2023,** *41* (5), 53205-53205.

3. Ploigt, H. C.; Brun, C.; Pivetta, M.; Patthey, F.; Schneider, W. D. Local work function changes determined by field emission resonances: NaCl/Ag (100). *Phys. Rev. B* **2007,** *76* (19), 195404-195404.

4. Pivetta, M.; Patthey, F.; Stengel, M.; Baldereschi, A.; Schneider, W. D. Local work function Moiré pattern on ultrathin ionic films: NaCl on Ag(100). *Phys. Rev. B* **2005,** *72* (11), 115404-115404.

5. Chen, C. J. *Introduction to Scanning Tunneling Microscopy, 2nd ed*. Oxford University Press, **2007**, p 1-432.

6. Landau, L. D.; Lifshi͡ts, E. M.; Pitaevskiĭ, L. P.; Sykes, J. B.; Bell, J. S. *Quantum mechanics : non-relativistic theory*, 3rd ed. Pergamon Press. **1977**, p 1-673.

7. McDowell, B. W.; Mills, J. M.; Honda, M.; Nazin, G. V. Structural Bistability in RbI Monolayers on Ag(111). *J. Phys. Chem. Lett.* **2023,** *14*, 3023-3030.

8. McDowell, B. W.; Mills, J. M.; Honda, M.; George; Nazin, V.; Nazin, G. V.; Affiliations. Spatially modulated interface states in a two-dimensional potential: Single-layer RbI on Ag(111). *J. Chem. Phys.* **2023,** *159* (22), 224705-224705.

9. McDowell, B. W.; Taber, B. N.; Mills, J. M.; Gervasi, C. F.; Honda, M.; Nazin, G. V. Modulation of Carbon Nanotube Electronic Structure by Grain Boundary Defects in RbI on Au(111). *J. Phs. Chem. Lett.* **2024,** *15*, 439-446.

REFERENCES CITED FOR CHAPTER III

1. Tan, C.; Cao, X.; Wu, X. J.; He, Q.; Yang, J.; Zhang, X.; Chen, J.; Zhao, W.; Han, S.; Nam, G. H.; Sindoro, M.; Zhang, H. Recent Advances in Ultrathin Two-Dimensional Nanomaterials. *Chem. Rev.* **2017,** *117* (9), 6225-6331.

2. Novoselov, K. S.; Mishchenko, A.; Carvalho, A.; Castro Neto, A. H. 2D materials and van der Waals heterostructures. *Science* **2016,** *353* (6298).

3. Wang, Q. H.; Kalantar-Zadeh, K.; Kis, A.; Coleman, J. N.; Strano, M. S. Electronics and optoelectronics of two-dimensional transition metal dichalcogenides. *Nat. Nanotechnol.* **2012,** *7* (11), 699-712.

4. Weiss, N. O.; Zhou, H.; Liao, L.; Liu, Y.; Jiang, S.; Huang, Y.; Duan, X.; Duan, X.; Zhou, H.; Liao, L.; Jiang, S.; Huang, Y.; Weiss, N. O.; Liu, Y. Graphene: An Emerging Electronic Material. *Adv. Mater.* **2012,** *24* (43), 5782-5825.

5. Illarionov, Y. Y.; Knobloch, T.; Jech, M.; Lanza, M.; Akinwande, D.; Vexler, M. I.; Mueller, T.; Lemme, M. C.; Fiori, G.; Schwierz, F.; Grasser, T. Insulators for 2D nanoelectronics: the gap to bridge. *Nat. Comm.* **2020,** *11* (1), 1-15.

6. Illarionov, Y. Y.; Banshchikov, A. G.; Polyushkin, D. K.; Wachter, S.; Knobloch, T.; Thesberg, M.; Mennel, L.; Paur, M.; Stöger-Pollach, M.; Steiger-Thirsfeld, A.; Vexler, M. I.; Waltl, M.; Sokolov, N. S.; Mueller, T.; Grasser, T. Ultrathin calcium fluoride insulators for two-dimensional field-effect transistors. *Nat. Electron.* **2019,** *2* (6), 230-235.

7. Li, W.; Zhou, J.; Cai, S.; Yu, Z.; Zhang, J.; Fang, N.; Li, T.; Wu, Y.; Chen, T.; Xie, X.; Ma, H.; Yan, K.; Dai, N.; Wu, X.; Zhao, H.; Wang, Z.; He, D.; Pan, L.; Shi, Y.; Wang, P.; Chen, W.; Nagashio, K.; Duan, X.; Wang, X. Uniform and ultrathin high-κ gate dielectrics for two-dimensional electronic devices. *Nat. Electron.* **2019,** *2* (12), 563-571.

8. Fröhlich, D.; Staginnus, B. New assignment of the band gap in the alkali bromides by two-photon spectroscopy. *Phys. Rev. Lett.* **1967,** *19* (9), 496-498.

9. Brown, F. C.; Gähwiller, C.; Fujita, H.; Kunz, A. B.; Scheifley, W.; Carrera, N. Extreme-ultraviolet spectra of ionic crystals. *Phys. Rev. B* **1970,** *2* (6), 2126-2138.

10. Pivetta, M.; Patthey, F.; Stengel, M.; Baldereschi, A.; Schneider, W. D. Local work function Moiré pattern on ultrathin ionic films: NaCl on Ag(100). *Phys. Rev. B* **2005,** *72* (11), 115404-115404.

11. Hebenstreit, W.; Redinger, J.; Horozova, Z.; Schmid, M.; Podloucky, R.; Varga, P. Atomic resolution by STM on ultra-thin films of alkali halides: Experiment and local density calculations. *Surf. Sci.* **1999,** *424* (2), L321-L328.

12. Sun, X.; Felicissimo, M. P.; Rudolf, P.; Silly, F. NaCl multi-layer islands grown on Au(111)-(22 × √3) probed by scanning tunneling microscopy. *Nanotechnol.* **2008,** *19* (49).

13. Olsson, F. E.; Persson, M. A density functional study of adsorption of sodium-chloride overlayers on a stepped and a flat copper surface. *Surf. Sci.* **2003,** *540* (2-3), 172-184.

14. Olsson, F. E.; Persson, M.; Repp, J.; Meyer, G. Scanning tunneling microscopy and spectroscopy of NaCl overlayers on the stepped Cu(311) surface: Experimental and theoretical study. *Phys. Rev. B.* **2005,** *71* (7), 075419-075419.

15. Matthaei, F.; Heidorn, S.; Boom, K.; Bertram, C.; Safiei, A.; Henzl, J.; Morgenstern, K. Coulomb attraction during the carpet growth mode of NaCl. *J. Phys. Condens. Matter* **2012,** *24* (35), 354006-354006.

16. Tikhomirova, K. A.; Tantardini, C.; Sukhanova, E. V.; Popov, Z. I.; Evlashin, S. A.; Tarkhov, M. A.; Zhdanov, V. L.; Dudin, A. A.; Oganov, A. R.; Kvashnin, D. G.; Kvashnin, A. G. Exotic Two-Dimensional Structure: The First Case of Hexagonal NaCl. *J. Phys. Chem. Lett.* **2020,** *11* (10), 3821-3827.

17. Parkinson, G. S. Iron oxide surfaces. *Surf. Sci. Rep.* **2016,** *71* (1), 272-365.

18. Benia, H. M.; Myrach, P.; Nilius, N.; Freund, H. J. Structural and electronic characterization of the MgO/Mo(0 0 1) interface using STM. *Surf. Sci.* **2010,** *604* (3-4), 435-441.

19. Matencio, S.; Barrena, E.; Ocal, C. Coming across a novel copper oxide 2D framework during the oxidation of Cu(111). *Phys. Chem. Chem. Phys.* **2016,** *18* (48), 33303-33309.

20. Möller, C.; Barreto, J.; Stavale, F.; Nilius, N. Manganese Oxide Thin Films on Au(111): Growth Competition between MnO and Mn3O4. *J. Phys. Chem. C* **2019,** *123* (13), 7665-7672.

21. Dudin, P.; Barinov, A.; Gregoratti, L.; Kiskinova, M.; Esch, F.; Dri, C.; Africh, C.; Comelli, G. Initial oxidation of a Rh(110) surface using atomic or molecular oxygen and reduction of the surface oxide by hydrogen. *J. Phys. Chem. B* **2005,** *109* (28), 13649-13655.

22. Shao, X.; Nilius, N.; Myrach, P.; Freund, H. J.; Martinez, U.; Prada, S.; Giordano, L.; Pacchioni, G. Strain-induced formation of ultrathin mixed-oxide films. *Phys. Rev. B* **2011,** *83* (24), 245407-245407.

23. Schoiswohl, J.; Sock, M.; Eck, S.; Surnev, S.; Ramsey, M. G.; Netzer, F. P.; Kresse, G. Atomic-level growth study of vanadium oxide nanostructures on Rh(111). *Phys. Rev. B* **2004,** *69* (15), 155403-155403.

24. Hackley, J. D.; Kislitsyn, D. A.; Beaman, D. K.; Ulrich, S.; Nazin, G. V. High-stability cryogenic scanning tunneling microscope based on a closed-cycle cryostat. *Rev. Sci. Instrum.* **2014,** *85* (10), 103704.

25. Kohn, W.; Sham, L. J. Self-consistent equations including exchange and correlation effects. *Phys. Rev.* **1965,** *140* (4A), A1133-A1133.

26. Kresse, G.; Furthmüller, J. Efficiency of ab-initio total energy calculations for metals and semiconductors using a plane-wave basis set. *Comput. Mater. Sci.* **1996,** *6* (1), 15-50.

27. Kresse, G.; Furthmüller, J. Efficient iterative schemes for ab initio total-energy calculations using a plane-wave basis set. *Phys. Rev. B* **1996,** *54* (16), 11169-11186.

28. Kresse, G.; Hafner, J. Ab initio molecular dynamics for liquid metals. *Phys. Rev. B* **1993,** *47* (1), 558-561.

29. Blöchl, P. E. Projector augmented-wave method. *Phys. Rev. B* **1994,** *50* (24), 17953-17979.

30. Tran, R.; Xu, Z.; Radhakrishnan, B.; Winston, D.; Sun, W.; Persson, K. A.; Ong, S. P. Surface energies of elemental crystals. *Sci. Data* **2016,** *3* (1), 160080.

31. Perdew, J. P.; Ruzsinszky, A.; Csonka, G. I.; Vydrov, O. A.; Scuseria, G. E.; Constantin, L. A.; Zhou, X.; Burke, K. Restoring the density-gradient expansion for exchange in solids and surfaces. *Phys. Rev. Lett.* **2008,** *100* (13), 136406-136406.

32. Krukau, A. V.; Vydrov, O. A.; Izmaylov, A. F.; Scuseria, G. E. Influence of the exchange screening parameter on the performance of screened hybrid functionals. *J. Chem. Phys.* **2006,** *125* (22), 224106-224106.

33. Henkelman, G.; Arnaldsson, A.; Jónsson, H. A fast and robust algorithm for Bader decomposition of charge density. *Comput. Mater. Sci.* **2006,** *36* (3), 354-360.

34. Sanville, E.; Kenny, S. D.; Smith, R.; Henkelman, G. Improved grid-based algorithm for Bader charge allocation. *J. Comput. Chem.* **2007,** *28* (5), 899-908.

35. Tang, W.; Sanville, E.; Henkelman, G. A grid-based Bader analysis algorithm without lattice bias. *J. Phys. Condens. Matter* **2009,** *21* (8), 084204-084204.

36. Yu, M.; Trinkle, D. R. Accurate and efficient algorithm for Bader charge integration. *J. Chem. Phys.* **2011,** *134* (6), 64111-64111.

37. Momma, K.; Izumi, F. VESTA 3 for three-dimensional visualization of crystal, volumetric and morphology data. *J. Appl. Crystallogr.* **2011,** *44* (6), 1272-1276.

38. Chen, C. J. *Introduction to Scanning Tunneling Microscopy, 2nd ed*. Oxford University Press, **2007**, p 1-432.

39. Wilson, J. N.; Curtis, R. M. Dipole polarizabilities of ions in alkali halide crystals. *J. Phys. Chem.* **2002,** *74* (1), 187-196.

40. Liljeroth, P.; Repp, J.; Meyer, G. Current-Induced Hydrogen Tautomerization and Conductance Switching of Naphthalocyanine Molecules. *Science* **2007,** *317* (5842), 1203-1206.

41. Bartels, L.; Hla, S. W.; Kühnle, A.; Meyer, G.; Rieder, K. H.; Manson, J. R. STM observations of a one-dimensional electronic edge state at steps on Cu(111). *Phys. Rev. B* **2003,** *67* (20), 205416-205416.

42. Jia, J.; Inoue, K.; Hasegawa, Y. Variation of the local work function at steps on metal surfaces studied with STM. *Phys. Rev. B* **1998,** *58* (3), 1193-1193.

43. Smoluchowski, R. Anisotropy of the Electronic Work Function of Metals. *Phys. Rev.* **1941,** *60* (9), 661-661.

REFERENCES CITED FOR CHAPTER IV

1. Tan, C.; Cao, X.; Wu, X. J.; He, Q.; Yang, J.; Zhang, X.; Chen, J.; Zhao, W.; Han, S.; Nam, G. H.; Sindoro, M.; Zhang, H. Recent Advances in Ultrathin Two-Dimensional Nanomaterials. *Chem. Rev.* **2017,** *117* (9), 6225-6331.

2. Liu, Y.; Duan, X.; Huang, Y.; Duan, X. Two-dimensional transistors beyond graphene and TMDCs. *Chem. Society Rev.* **2018,** *47* (16), 6388-6409.

3. Parkinson, G. S. Iron oxide surfaces. *Surf. Sci. Rep.* **2016,** *71* (1), 272-365.

4. Gao, L.; Cui, X.; Sewell, C. D.; Li, J.; Lin, Z. Recent advances in activating surface reconstruction for the high-efficiency oxygen evolution reaction. *Chem. Society Rev.* **2021,** *50* (15), 8428-8469.

5. Illarionov, Y. Y.; Knobloch, T.; Jech, M.; Lanza, M.; Akinwande, D.; Vexler, M. I.; Mueller, T.; Lemme, M. C.; Fiori, G.; Schwierz, F.; Grasser, T. Insulators for 2D nanoelectronics: the gap to bridge. *Nat. Comm.* **2020,** *11* (1), 1-15.

6. McDowell, B. W.; Mills, J. M.; Honda, M.; Nazin, G. V. Structural Bistability in RbI Monolayers on Ag(111). *J. Phys. Chem Lett.* **2023,** *14*, 3023-3030.

7. Matencio, S.; Barrena, E.; Ocal, C. Coming across a novel copper oxide 2D framework during the oxidation of Cu(111). *Phys. Chem. Chem. Phys.* **2016,** *18* (48), 33303-33309.

8. Möller, C.; Barreto, J.; Stavale, F.; Nilius, N. Manganese Oxide Thin Films on Au(111): Growth Competition between MnO and Mn3O4. *J. Phys. Chem. C* **2019,** *123* (13), 7665-7672.

9. Shao, X.; Nilius, N.; Myrach, P.; Freund, H. J.; Martinez, U.; Prada, S.; Giordano, L.; Pacchioni, G. Strain-induced formation of ultrathin mixed-oxide films. *Phys. Rev. B* **2011,** *83* (24), 245407-245407.

10. Schoiswohl, J.; Sock, M.; Eck, S.; Surnev, S.; Ramsey, M. G.; Netzer, F. P.; Kresse, G. Atomic-level growth study of vanadium oxide nanostructures on Rh(111). *Phys. Rev. B* **2004,** *69* (15), 155403-155403.

11. Benia, H. M.; Myrach, P.; Nilius, N.; Freund, H. J. Structural and electronic characterization of the MgO/Mo(0 0 1) interface using STM. *Surf. Sci.* **2010,** *604* (3-4), 435-441.

12. Pivetta, M.; Patthey, F.; Stengel, M.; Baldereschi, A.; Schneider, W. D. Local work function Moiré pattern on ultrathin ionic films: NaCl on Ag(100). *Phys. Rev. B* **2005,** *72* (11), 115404-115404.

13. Kolpatzeck, K.; Brendel, L.; Möller, R.; Robles, R.; Lorente, N. Paradoxical effects for a one-dimensional periodic potential embedded in a two-dimensional system. *Phys. Rev. B* **2023,** *107* (15), 155418-155418.

14. Repp, J.; Meyer, G.; Rieder, K. H. Snell's Law for Surface Electrons: Refraction of an Electron Gas Imaged in Real Space. *Phys. Rev. Lett.* **2004,** *92* (3), 4-4.

15. McDowell, B. W.; Mills, J. M.; Honda, M.; George; Nazin, V.; Nazin, G. V.; Affiliations. Spatially modulated interface states in a two-dimensional potential: Single-layer RbI on Ag(111). J. *Chem. Phys.* **2023,** *159* (22), 224705-224705.

16. Pan, Y.; Benedetti, S.; Nilius, N.; Freund, H. J. Change of the surface electronic structure of Au(111) by a monolayer MgO(001) film. *Phys. Rev. B* **2011,** *84* (7), 075456-075456.

17. Bian, K.; Gerber, C.; Heinrich, A. J.; Müller, D. J.; Scheuring, S.; Jiang, Y. Scanning probe microscopy. *Nat. Rev. Methods Primers* **2021,** *1* (1), 1-29.

18. Fröhlich, D.; Staginnus, B. New assignment of the band gap in the alkali bromides by two-photon spectroscopy. *Phys. Rev. Lett.* **1967,** *19* (9), 496-498.

19. Brown, F. C.; Gähwiller, C.; Fujita, H.; Kunz, A. B.; Scheifley, W.; Carrera, N. Extreme-ultraviolet spectra of ionic crystals. *Phys. Rev. B* **1970,** *2* (6), 2126-2138.

20. Hebenstreit, W.; Redinger, J.; Horozova, Z.; Schmid, M.; Podloucky, R.; Varga, P. Atomic resolution by STM on ultra-thin films of alkali halides: Experiment and local density calculations. *Surf. Sci.* **1999,** *424* (2), L321-L328.

21. Sun, X.; Felicissimo, M. P.; Rudolf, P.; Silly, F. NaCl multi-layer islands grown on Au(111)-(22 × √3) probed by scanning tunneling microscopy. *Nanotechnol.* **2008,** *19* (49).

22. Olsson, F. E.; Persson, M. A density functional study of adsorption of sodium-chloride overlayers on a stepped and a flat copper surface. *Surf. Sci.* **2003,** *540* (2-3), 172-184.

23. Olsson, F. E.; Persson, M.; Repp, J.; Meyer, G. Scanning tunneling microscopy and spectroscopy of NaCl overlayers on the stepped Cu(311) surface: Experimental and theoretical study. *Phys. Rev. B.* **2005,** *71* (7), 075419-075419.

24. McDowell, B. W.; Taber, B. N.; Mills, J. M.; Gervasi, C. F.; Honda, M.; Nazin, G. V. Modulation of Carbon Nanotube Electronic Structure by Grain Boundary Defects in RbI on Au(111). *J. Phys. Chem. Lett.* **2024,** *15*, 439-446.

25. Heidorn, S.; Bertram, C.; Koch, J.; Boom, K.; Matthaei, F.; Safiei, A.; Henzl, J.; Morgenstern, K. Influence of substrate surface-induced defects on the interface state between NaCl(100) and Ag(111). *J. Phys. Chem. C* **2013,** *117* (31), 16095-16103.

26. Repp, J.; Meyer, G.; Paavilainen, S.; Olsson, F. E.; Persson, M. Scanning tunneling spectroscopy of Cl vacancies in NaCl films: Strong electron-phonon coupling in double-barrier tunneling junctions. *Phys. Rev. Lett.* **2005,** *95* (22), 225503-225503.

27. Hackley, J. D.; Kislitsyn, D. A.; Beaman, D. K.; Ulrich, S.; Nazin, G. V. High-stability cryogenic scanning tunneling microscope based on a closed-cycle cryostat. *Rev. Sci. Instrum.* **2014,** *85* (10), 103704.

28. Taber, B. N.; Neill, M. L.; Thom, T. N.; Clapp, O. D.; Lee, J. In situ plasmonic tip preparation and validation techniques for scanning tunneling microscopy. *J. Vac. Sci. Technol. A* **2023,** *41* (5), 53205-53205.

29. Ploigt, H. C.; Brun, C.; Pivetta, M.; Patthey, F.; Schneider, W. D. Local work function changes determined by field emission resonances: NaCl/Ag (100). *Phys. Rev. B* **2007,** *76* (19), 195404-195404.

30. Kohn, W.; Sham, L. J. Self-consistent equations including exchange and correlation effects. *Phys. Rev.* **1965,** *140* (4A), A1133-A1133.

31. Kresse, G.; Furthmüller, J. Efficiency of ab-initio total energy calculations for metals and semiconductors using a plane-wave basis set. *Comput. Mater. Sci.* **1996,** *6* (1), 15-50.

32. Kresse, G.; Furthmüller, J. Efficient iterative schemes for ab initio total-energy calculations using a plane-wave basis set. *Phys. Rev. B* **1996,** *54* (16), 11169-11186.

33. Kresse, G.; Hafner, J. Ab initio molecular dynamics for liquid metals. *Phys. Rev. B* **1993,** *47* (1), 558-561.

34. Blöchl, P. E. Projector augmented-wave method. *Phys. Rev. B* **1994,** *50* (24), 17953-17979.

35. Tran, R.; Xu, Z.; Radhakrishnan, B.; Winston, D.; Sun, W.; Persson, K. A.; Ong, S. P. Surface energies of elemental crystals. *Sci. Data* **2016,** *3* (1), 160080.

36. Perdew, J. P.; Ruzsinszky, A.; Csonka, G. I.; Vydrov, O. A.; Scuseria, G. E.; Constantin, L. A.; Zhou, X.; Burke, K. Restoring the density-gradient expansion for exchange in solids and surfaces. *Phys. Rev. Lett.* **2008,** *100* (13), 136406-136406.

37. Henkelman, G.; Arnaldsson, A.; Jónsson, H. A fast and robust algorithm for Bader decomposition of charge density. *Comput. Mater. Sci.* **2006,** *36* (3), 354-360.

38. Sanville, E.; Kenny, S. D.; Smith, R.; Henkelman, G. Improved grid-based algorithm for Bader charge allocation. *J. Comput. Chem.* **2007,** *28* (5), 899-908.

39. Tang, W.; Sanville, E.; Henkelman, G. A grid-based Bader analysis algorithm without lattice bias. *J. Phys. Condens. Matter* **2009,** *21* (8), 084204-084204.

40. Yu, M.; Trinkle, D. R. Accurate and efficient algorithm for Bader charge integration. *J. Chem. Phys.* **2011,** *134* (6), 64111-64111.

41. Momma, K.; Izumi, F. VESTA 3 for three-dimensional visualization of crystal, volumetric and morphology data. *J. Appl. Crystallogr.* **2011,** *44* (6), 1272-1276.

42. P. Morse and H. Feshbach, *Methods of Theoretical Physics* (Mcgraw-Hill, 1953), Vol. 2. p.1298-1299

43. Smith, N. V.; Chen, C. T.; Weinert, M. Distance of the image plane from metal surfaces. *Phys. Rev. B* **1989,** *40* (11), 7565-7565.

44. Blowey, P. J.; Sohail, B.; Rochford, L. A.; Lafosse, T.; Duncan, D. A.; Ryan, P. T. P.; Warr, D. A.; Lee, T. L.; Costantini, G.; Maurer, R. J.; Woodruff, D. P. Alkali Doping Leads to Charge-Transfer Salt Formation in a Two-Dimensional Metal-Organic Framework. *ACS Nano* **2020,** *14* (6), 7475-7483.

45. Haags, A.; Rochford, L. A.; Felter, J.; Blowey, P. J.; Duncan, D. A.; Woodruff, D. P.; Kumpf, C. Growth and evolution of tetracyanoquinodimethane and potassium coadsorption phases on Ag(111). *New J. Phys.* **2020,** *22* (6), 063028-063028.

46. Kamiyoshi, K.; Nigara, Y. Dielectric constant of some alkali halides. *Phys. Status Solidi* **1970,** *3* (3), 735-741.

47. Tan, X.; Pan, J.; Feng, J.; Zhang, Z.; Liu, M.; Ma, D.; Qiu, X. One-Dimensional Periodic Buckling at a Symmetry-Incompatible Heterointerface of the NaCl(001) Monolayer on Ir(111). *J. Phys. Chem. C* **2023,** *127* (12), 6109-6114.

REFERENCES CITED FOR CHAPTER V

1. Piquero-Zulaica, I.; Lobo-Checa, J.; El-Fattah, Z. M. A.; Ortega, J. E.; Klappenberger, F.; Auwärter, W.; Barth, J. V. Engineering quantum states and electronic landscapes through surface molecular nanoarchitectures. *Rev. Mod. Phys.* **2022,** *94* (4), 045008-045008.

2. Goronzy, D. P.; Ebrahimi, M.; Rosei, F.; Arramel; Fang, Y.; De Feyter, S.; Tait, S. L.; Wang, C.; Beton, P. H.; Wee, A. T. S.; Weiss, P. S.; Perepichka, D. F. Supramolecular assemblies on surfaces: Nanopatterning, functionality, and reactivity. *ACS Nano* **2018,** *12* (8), 7445-7481.

3. Nicoara, N.; Méndez, J.; Gómez-Rodríguez, J. M. Visualizing the interface state of PTCDA on Au(111) by scanning tunneling microscopy. *Nanotechnol.* **2016,** *27* (47), 475707-475707.

4. Sabitova, A.; Temirov, R.; Tautz, F. S. Lateral scattering potential of the PTCDA/Ag(111) interface state. *Phys. Rev. B* **2018,** *98* (20), 205429-205429.

5. Eschmann, L.; Sabitova, A.; Temirov, R.; Tautz, F. S.; Krüger, P.; Rohlfing, M. Coverage-dependent anisotropy of the NTCDA/Ag(111) interface state dispersion. *Phys. Rev. B* **2019,** *100* (12), 125155-125155.

6. Park, J. Y.; Ham, U. D.; Kahng, S. J.; Kuk, Y.; Miyake, K.; Hata, K.; Shigekawa, H. Modification of surface-state dispersion upon Xe adsorption: A scanning tunneling microscope study. *Phys. Rev. B* **2000,** *62* (24), R16341-R16341.

7. Bowen, H. F.; Space, B. The effective mass of excess electrons in condensed xenon: Toward methods for modeling metal-dielectric interfaces. *J. Chem. Phys.* **1997,** *107* (6), 1922-1930.

8. Wolf, M.; Knoesel, E.; Hertel, T. Ultrafast dynamics of electrons in image-potential states on clean and Xe-covered Cu(111). *Phys. Rev. B* **1996,** *54* (8), R5295-R5295.

9. Hövel, H.; Grimm, B.; Reihl, B. Modification of the Shockley-type surface state on Ag(1 1 1) by an adsorbed xenon layer. *Surface Science* **2001,** *477* (1), 43-49.

10. Kolpatzeck, K.; Brendel, L.; Möller, R.; Robles, R.; Lorente, N. Paradoxical effects for a one-dimensional periodic potential embedded in a two-dimensional system. *Phys. Rev. B* **2023,** *107* (15), 155418-155418.

11. Heidorn, S. C.; Sabellek, A.; Morgenstern, K. Size dependence of the dispersion relation for the interface state between NaCl(100) and Ag(111). *Nano Lett.* **2014,** *14* (1), 13-17.

12. Heidorn, S.; Bertram, C.; Koch, J.; Boom, K.; Matthaei, F.; Safiei, A.; Henzl, J.; Morgenstern, K. Influence of substrate surface-induced defects on the interface state between NaCl(100) and Ag(111). *J. Phys. Chem. C* **2013,** *117* (31), 16095-16103.

13. Repp, J.; Meyer, G.; Rieder, K. H. Snell's Law for Surface Electrons: Refraction of an Electron Gas Imaged in Real Space. *Phys. Rev. Lett.* **2004,** *92* (3), 4-4.

14. Repp, J.; Meyer, G.; Paavilainen, S.; Olsson, F. E.; Persson, M. Scanning tunneling spectroscopy of Cl vacancies in NaCl films: Strong electron-phonon coupling in double-barrier tunneling junctions. *Phys. Rev. Lett.* **2005,** *95* (22), 225503-225503.

15. Schouteden, K.; Li, Z.; Iancu, V.; Muzychenko, D. A.; Janssens, E.; Lievens, P.; Van Haesendonck, C. Engineering the band structure of nanoparticles by an incommensurate cover layer. *J. Phys. Chem. C* **2014,** *118* (31), 18271-18277.

16. Min, K.-A.; Park, J.; Wallace, R. M.; al; Han, D.; Zhu, J.; Lauwaet, K.; Schouteden, K.; Janssens, E.; Van Haesendonck, C.; Lievens, P. Dependence of the NaCl/Au(111) interface state on the thickness of the NaCl layer. *J. Phys. Condens. Matter* **2012,** *24* (47), 475507-475507.

17. Del Puppo, S.; Carnevali, V.; Perilli, D.; Zarabara, F.; Rizzini, A. L.; Fornasier, G.; Zupanič, E.; Fiori, S.; Patera, L. L.; Panighel, M.; Bhardwaj, S.; Zou, Z.; Comelli, G.; Africh, C.; Cepek, C.; Di Valentin, C.; Peressi, M. Tuning graphene doping by carbon monoxide intercalation at the Ni(111) interface. *Carbon* **2021,** *176*, 253-261.

18. Omidian, M.; Néel, N.; Manske, E.; Pezoldt, J.; Lei, Y.; Kröger, J. Structural and local electronic properties of clean and Li-intercalated graphene on SiC(0001). *Surf. Sci.* **2020,** *699*, 121638-121638.

19. Ziegler, M.; Kröger, J.; Berndt, R.; Borisov, A. G.; Gauyacq, J. P. Linewidth of a cesium adatom resonance on Ag(111). *Phys. Rev. B* **2009,** *79* (7), 075401-075401.

20. Zhang, Z.; Hu, J.; Yang, P.; Pan, S.; Quan, W.; Li, N.; Zhu, L.; Zhang, Y. Modulating the periods and electronic properties of striped moiré superstructures for monolayer WSe2 on Au(100) by varied interface coupling. *Nanoscale* **2022,** *14* (20), 7720-7728.

21. Xiao, Y.; Liu, J.; Fu, L. Moiré is More: Access to New Properties of Two-Dimensional Layered Materials. *Matter* **2020,** *3* (4), 1142-1161.

22. Lopes Dos Santos, J. M. B.; Peres, N. M. R.; Castro Neto, A. H. Graphene bilayer with a twist: Electronic structure. *Phys. Rev. Lett.* **2007,** *99* (25), 256802-256802.

23. Zhang, Q.; Yu, J.; Ebert, P.; Zhang, C.; Pan, C. R.; Chou, M. Y.; Shih, C. K.; Zeng, C.; Yuan, S. Tuning Band Gap and Work Function Modulations in Monolayer hBN/Cu(111) Heterostructures with Moiré Patterns. *ACS Nano* **2018,** *12* (9), 9355-9362.

24. Varykhalov, A.; Sánchez-Barriga, J.; Shikin, A. M.; Biswas, C.; Vescovo, E.; Rybkin, A.; Marchenko, D.; Rader, O. Electronic and magnetic properties of quasifreestanding graphene on Ni. *Phys. Rev. Lett.* **2008,** *101* (15), 157601-157601.

25. Rizzo, D. J.; Veber, G.; Cao, T.; Bronner, C.; Chen, T.; Zhao, F.; Rodriguez, H.; Louie, S. G.; Crommie, M. F.; Fischer, F. R. Topological band engineering of graphene nanoribbons. *Nature* **2018,** *560* (7717), 204-208.

26. Brun, C.; Cren, T.; Roditchev, D. Review of 2D superconductivity: the ultimate case of epitaxial monolayers. *Supercond. Sci. Technol.* **2016,** *30* (1), 013003-013003.

27. Fröhlich, D.; Staginnus, B. New assignment of the band gap in the alkali bromides by two-photon spectroscopy. *Phys. Rev. Lett.* **1967,** *19* (9), 496-498.

28. Brown, F. C.; Gähwiller, C.; Fujita, H.; Kunz, A. B.; Scheifley, W.; Carrera, N. Extreme-ultraviolet spectra of ionic crystals. *Phys. Rev. B* **1970,** *2* (6), 2126-2138.

29. Pivetta, M.; Patthey, F.; Stengel, M.; Baldereschi, A.; Schneider, W. D. Local work function Moiré pattern on ultrathin ionic films: NaCl on Ag(100). *Phys. Rev. B* **2005,** *72* (11), 115404-115404.

30. Hebenstreit, W.; Redinger, J.; Horozova, Z.; Schmid, M.; Podloucky, R.; Varga, P. Atomic resolution by STM on ultra-thin films of alkali halides: Experiment and local density calculations. *Surf. Sci.* **1999,** *424* (2), L321-L328.

31. Sun, X.; Felicissimo, M. P.; Rudolf, P.; Silly, F. NaCl multi-layer islands grown on Au(111)-(22 × √3) probed by scanning tunneling microscopy. *Nanotechnology* **2008,** *19* (49).

32. Olsson, F. E.; Persson, M. A density functional study of adsorption of sodium-chloride overlayers on a stepped and a flat copper surface. *Surf. Sci.* **2003,** *540* (2-3), 172-184.

33. Olsson, F. E.; Persson, M.; Repp, J.; Meyer, G. Scanning tunneling microscopy and spectroscopy of NaCl overlayers on the stepped Cu(311) surface: Experimental and theoretical study. *Phys. Rev. B* **2005,** *71* (7), 075419-075419.

34. Pan, Y.; Benedetti, S.; Nilius, N.; Freund, H. J. Change of the surface electronic structure of Au(111) by a monolayer MgO(001) film. *Phys. Rev. B* **2011,** *84* (7), 075456-075456.

35. McDowell, B. W.; Mills, J. M.; Honda, M.; Nazin, G. V. Structural Bistability in RbI Monolayers on Ag(111). J. Phys. Chem. *Lett.* **2023,** *14*, 3023-3030.

36. Hackley, J. D.; Kislitsyn, D. A.; Beaman, D. K.; Ulrich, S.; Nazin, G. V. High-stability cryogenic scanning tunneling microscope based on a closed-cycle cryostat. *Rev. Sci. Instrum.* **2014,** *85* (10), 103704.

37. Kohn, W.; Sham, L. J. Self-consistent equations including exchange and correlation effects. *Phys. Rev.* **1965,** *140* (4A), A1133-A1133.

38. Kresse, G.; Furthmüller, J. Efficiency of ab-initio total energy calculations for metals and semiconductors using a plane-wave basis set. *Comput. Mater. Sci.* **1996,** *6* (1), 15-50.

39. Kresse, G.; Furthmüller, J. Efficient iterative schemes for ab initio total-energy calculations using a plane-wave basis set. *Phys. Rev. B* **1996,** *54* (16), 11169-11186.

40. Kresse, G.; Hafner, J. Ab initio molecular dynamics for liquid metals. *Phys. Rev. B* **1993,** *47* (1), 558-561.

41. Blöchl, P. E. Projector augmented-wave method. *Phys. Rev. B* **1994,** *50* (24), 17953-17979.

42. Tran, R.; Xu, Z.; Radhakrishnan, B.; Winston, D.; Sun, W.; Persson, K. A.; Ong, S. P. Surface energies of elemental crystals. *Sci. Data* **2016,** *3* (1), 160080.

43. Perdew, J. P.; Ruzsinszky, A.; Csonka, G. I.; Vydrov, O. A.; Scuseria, G. E.; Constantin, L. A.; Zhou, X.; Burke, K. Restoring the density-gradient expansion for exchange in solids and surfaces. *Phys. Rev. Lett.* **2008,** *100* (13), 136406-136406.

44. Momma, K.; Izumi, F. VESTA 3 for three-dimensional visualization of crystal, volumetric and morphology data. *J. Appl. Crystallogr.* **2011,** *44* (6), 1272-1276.

45. Quertite, K.; Enriquez, H.; Trcera, N.; Bendounan, A.; Mayne, A. J.; Dujardin, G.; El Kenz, A.; Benyoussef, A.; Dappe, Y. J.; Kara, A.; Oughaddou, H. Electron beam analysis induces Cl vacancy defects in a NaCl thin film. *Nanotechnol.* **2021,** *33* (9), 095706-095706.

46. Abramowitz, M.; Stegun, I. A. *Handbook of Mathematical Functions with Formulas, Graphs, and Mathematical Tables, 9th printing*. Dover: New York, 1972; p 722-722.

47. Zwillinger, D. *Handbook of Differential Equations*. 3rd ed.; Acadamic Press: Boston, 1997; p 125-125.

48. Reinert, F.; Nicolay, G.; Schmidt, S.; Ehm, D.; Hüfner, S. Direct measurements of the L-gap surface states on the (111) face of noble metals by photoelectron spectroscopy. *Phys. Rev. B* **2001,** *63* (11), 115415-115415.

REFERENCES CITED FOR CHAPTER VI

1. De Volder, M. F. L.; Tawfick, S. H.; Baughman, R. H.; Hart, A. J. Carbon Nanotubes: Present and Future Commercial Applications. *Science* **2013**, *339* (6119), 535-539

2. Novoselov, K. S.; Fal'ko, V. I.; Colombo, L.; Gellert, P. R.; Schwab, M. G.; Kim, K. A roadmap for graphene. *Nature* **2012**, *490* (7419), 192-200.

3. Charlier, J. C.; Blase, X.; Roche, S. Electronic and transport properties of nanotubes. *Rev. Mod. Phys.* **2007**, *79* (2), 677-732

4. Meunier, V.; Souza, A. G.; Barros, E. B.; Dresselhaus, M. S. Physical properties of low-dimensional sp(2)-based carbon nanostructures. *Rev. Mod. Phys.* **2016**, *88* (2)

5. Baughman, R. H.; Zakhidov, A. A.; de Heer, W. A. Carbon nanotubes - the route toward applications. *Science* **2002**, *297* (5582), 787-792

6. Yu, M. F.; Files, B. S.; Arepalli, S.; Ruoff, R. S. Tensile loading of ropes of single wall carbon nanotubes and their mechanical properties. *Phys. Rev. Lett.* **2000**, *84* (24), 5552-5555

7. Balandin, A. A. Thermal properties of graphene and nanostructured carbon materials. *Nat. Mater.* **2011**, *10* (8), 569-581

8. Javey, A.; Guo, J.; Wang, Q.; Lundstrom, M.; Dai, H. J. Ballistic carbon nanotube field-effect transistors. *Nature* **2003**, *424* (6949), 654-657

9. Zhang, J.; Liu, X. H.; Neri, G.; Pinna, N. Nanostructured Materials for Room-Temperature Gas Sensors. *Adv. Mater.* **2016**, *28* (5), 795-831

10. Collins, P. G.; Bradley, K.; Ishigami, M.; Zettl, A. Extreme oxygen sensitivity of electronic properties of carbon nanotubes. *Science* **2000**, *287* (5459), 1801-1804

11. Liu, Z.; Tabakman, S.; Welsher, K.; Dai, H. J. Carbon Nanotubes in Biology and Medicine: In vitro and in vivo Detection, Imaging and Drug Delivery. *Nano Res.* **2009**, *2* (2), 85-120

12. Liu, Y. X.; Dong, X. C.; Chen, P. Biological and chemical sensors based on graphene materials. *Chem. Soc. Rev.* **2012**, *41* (6), 2283-2307

13. Franklin, A. D. Nanomaterials in transistors: From high-performance to thin-film applications. *Science* **2015**, *349* (6249)

14. Avouris, P.; Chen, Z. H.; Perebeinos, V. Carbon-based electronics. *Nat. Nanotechnol.* **2007**, *2* (10), 605-615

15. Tulevski, G. S.; Franklin, A. D.; Frank, D.; Lobez, J. M.; Cao, Q.; Park, H.; Afzali, A.; Han, S. J.; Hannon, J. B.; Haensch, W. Toward High-Performance Digital Logic Technology with Carbon Nanotubes. *Acs Nano* **2014**, *8* (9), 8730-8745

16. Ostroverkhova, O. Organic Optoelectronic Materials: Mechanisms and Applications. *Chem. Rev.* **2016**, *116* (22), 13279-1341

17. Cao, Q.; Tersoff, J.; Farmer, D. B.; Zhu, Y.; Han, S. J. Carbon nanotube transistors scaled to a 40-nanometer footprint. *Science* **2017**, *356* (6345), 1369-1372

18. Franklin, A. D.; Luisier, M.; Han, S. J.; Tulevski, G.; Breslin, C. M.; Gignac, L.; Lundstrom, M. S.; Haensch, W. Sub-10 nm Carbon Nanotube Transistor. *Nano Lett.* **2012**, *12* (2), 758-762

19. Abou-Rachid, H.; Hu, A. G.; Timoshevskii, V.; Song, Y. F.; Lussier, L. S. Nanoscale high energetic materials: A polymeric nitrogen chain N(8) confined inside a carbon nanotube. *Phys. Rev. Lett.* **2008**, *100* (19)

20. Arico, A. S.; Bruce, P.; Scrosati, B.; Tarascon, J. M.; Van Schalkwijk, W. Nanostructured materials for advanced energy conversion and storage devices. *Nat. Mater.* **2005**, *4* (5), 366-377

21. Wang, G. P.; Zhang, L.; Zhang, J. J. A review of electrode materials for electrochemical supercapacitors. *Chem. Soc. Rev.* **2012**, *41* (2), 797-828

22. Corso, B. L.; Perez, I.; Sheps, T.; Sims, P. C.; Gul, O. T.; Collins, P. G. Electrochemical Charge-Transfer Resistance in Carbon Nanotube Composites. *Nano Lett.* **2014**, *14* (3), 1329-1336

23. Hirana, Y.; Tanaka, Y.; Niidome, Y.; Nakashima, N. Strong Micro-Dielectric Environment Effect on the Band Gaps of (n,m)Single-Walled Carbon Nanotubes. *J. Am. Chem. Soc.* **2010**, *132* (37), 13072-13077

24. Avouris, P. Molecular electronics with carbon nanotubes. *Acc. Chem. Res.* **2002**, *35* (12), 1026-103

25. Bachtold, A.; Hadley, P.; Nakanishi, T.; Dekker, C. Logic circuits with carbon nanotube transistors. *Science* **2001**, *294* (5545), 1317-1320

26. Tersoff, J. Low-frequency noise in nanoscale ballistic transistors. *Nano Lett.* **2007**, *7* (1), 194-198

27. Wang, N. P.; Heinze, S.; Tersoff, J. Random-telegraph-signal noise and device variability in ballistic nanotube transistors. *Nano Lett.* **2007**, *7* (4), 910-913

28. Clair, S.; Shin, H. J.; Kim, Y.; Kawai, M. Electronic modulations in a single wall carbon nanotube induced by the Au(111) surface reconstruction. *Appl. Phys. Lett.* **2015**, *106* (5), 4

29. Shin, H.-J.; Clair, S.; Kim, Y.; Kawai, M. Substrate-induced array of quantum dots in a single-walled carbon nanotube. *Nat. Nanotechnol.* **2009**, *4* (9), 567-570

(30) Kislitsyn, D. A.; Hackley, J. D.; Nazin, G. V. Vibrational Excitation in Electron Transport through Carbon Nanotube Quantum Dots. *J. Phys. Chem. Lett.* **2014**, 3138-3143

31. Chen, C. J. *Introduction to Scanning Tunneling Microscopy*; Oxford University Press, 2008.

32. Hackley, J. D.; Kislitsyn, D. A.; Beaman, D. K.; Ulrich, S.; Nazin, G. V. High-stability cryogenic scanning tunneling microscope based on a closed-cycle cryostat. *Rev. Sci. Instrum.* **2014**, *85* (10), 103704

33. Albrecht, P. M.; Lyding, J. W. Ultrahigh-vacuum scanning tunneling microscopy and spectroscopy of single-walled carbon nanotubes on hydrogen-passivated Si(100) surfaces. *Appl. Phys. Lett.* **2003**, *83* (24), 5029-5031

34. Hanwell, M. D.; Curtis, D. E.; Lonie, D. C.; Vandermeersch, T.; Zurek, E.; Hutchison, G. R. Avogadro: an advanced semantic chemical editor, visualization, and analysis platform. *J. Cheminformatics* **2012**, *4*, 17,

35. Stephens, P. J.; Devlin, F. J.; Chabalowski, C. F.; Frisch, M. J. Ab Initio Calculation of Vibrational Absorption and Circular Dichroism Spectra Using Density Functional Force Fields. *J. Phys. Chem.* **1994**, *98*, 11623-11627

36. Yanai, T.; Tew, D. P.; Handy, N. C. A new hybrid exchange-correlation functional using the Coulomb-attenuating method (CAM-B3LYP). *Chem. Phys. Lett.* **2004**, *393* (1-3), 51-57

37. Hehre, W. J.; Stewart, R. F.; Pople, J. A. Self-consistent molecular-orbital methods .i. Use of gaussian expansions of slater-type atomic orbitals. *J. Chem. Phys.* **1969**, *51* (6), 2657

38. *Gaussian 09*; Gaussian, Inc.: Wallingford, CT, USA, 2009. (accessed.

39. Lu, T.; Chen, F. Multiwfn: A Multifunctional Wavefunction Analyzer. *J. Comput. Chem.* **2012**, *33* (5), 580-592

40. Kislitsyn, D. A.; Taber, B.; Gervasi, C. F.; Zhang, L.; Mannsfeld, S. C. B.; Prell, J.; Briseno, A.; Nazin, G. Y. Oligothiophene Wires: Impact of Torsional Conformation on the Electronic Structure. *Phys. Chem. Chem. Phys.* **2016**

41. Taber, B. N.; Kislitsyn, D. A.; Gervasi, C. F.; Mills, J. M.; Rosenfield, A. E.; Zhang, L.; Mannsfeld, S. C. B.; Prell, J. S.; Briseno, A. L.; Nazin, G. V. Real-space visualization of conformation-independent oligothiophene electronic structure. *J. Chem. Phys.* **2016**, *144* (19), 7

42. Barth, J. V.; Brune, H.; Ertl, G.; Behm, R. J. Scanning tunneling microscopy observations on the reconstructed au(111) surface - atomic-structure, long-range superstructure, rotational domains, and surface-defects. *Phys. Rev. B* **1990**, *42* (15), 9307-9318

43. Jaklevic, R. C.; Elie, L. Scanning-tunneling-microscope observation of surface-diffusion on an atomic scale - au on au(111). *Phys. Rev. Lett.* **1988**, *60* (2), 120-123

44. Woll, C.; Chiang, S.; Wilson, R. J.; Lippel, P. H. Determination of atom positions at stacking-fault dislocations on au(111) by scanning tunneling microscopy. *Phys. Rev. B* **1989**, *39* (11), 7988-7991

45. Ma, J.; Alfe, D.; Michaelides, A.; Wang, E. Stone-Wales defects in graphene and other planar sp(2)-bonded materials. *Phys. Rev. B* **2009**, *80* (3)

46. Miyamoto, Y.; Rubio, A.; Berber, S.; Yoon, M.; Tomanek, D. Spectroscopic characterization of Stone-Wales defects in nanotubes. *Phys. Rev. B* **2004**, *69* (12)

47. Berthe, M.; Yoshida, S.; Ebine, Y.; Kanazawa, K.; Okada, A.; Taninaka, A.; Takeuchi, O.; Fukui, N.; Shinohara, H.; Suzuki, S.; et al. Reversible defect engineering of single-walled carbon nanotubes using scanning tunneling microscopy. *Nano Lett.* **2007**, *7* (12), 3623-3627

48. Clair, S.; Kim, Y.; Kawai, M. Energy level alignment of single-wall carbon nanotubes on metal surfaces. *Phys. Rev. B* **2011**, *83* (24), 245422

49. Hanke, F.; Björk, J. Structure and Local Reactivity of the Au(111) Surface Reconstruction. *Phys. Rev. B* **2013**, *87* (23), 235422.

50. Mena-Osteritz, E.; Urdanpilleta, M.; El-Hosseiny, E.; Koslowski, B.; Ziemann, P.; Bauerle, P. STM Study on the Self-Assembly of Oligothiophene-Based Organic Semiconductors. *Nanotechnol.* **2011**, *2*, 802-808

51. Buimaga-Iarinca, L.; Morari, C. Adsorption of Small Aromatic Molecules on Gold: a DFT Localized Basis Set Study Including Van Der Waals Effects. *Theor. Chem. Acc.* **2014**, *133* (7), 1502

52. Taber, B. N.; Kislitsyn, D. A.; Gervasi, C. F.; Mannsfeld, S. C. B.; Zhang, L.; Briseno, A. L.; Nazin, G. V. Adsorption-Induced Conformational Isomerization of Alkyl-Substituted Thiophene Oligomers on Au(111): Impact on the Interfacial Electronic Structure. *ACS Appl. Mater. Interfaces* **2015**, *7* (28), 15138-15142

53. Shin, H. J.; Clair, S.; Kim, Y.; Kawai, M. Electronic structure of single-walled carbon nanotubes on ultrathin insulating films. *Appl. Phys. Lett.* **2008**, *93* (23)

54. Suzuki, S.; Watanabe, Y.; Homma, Y.; Fukuba, S.; Heun, S.; Locatelli, A. Work functions of individual single-walled carbon nanotubes. *Appl. Phys. Lett.* **2004**, *85* (1), 127-129

55. Derry, G. N.; Kern, M. E.; Worth, E. H. Recommended values of clean metal surface work functions. *J. Vac. Sci. Technol. A* **2015**, *33* (6)

56. Park, J. Y.; Sacha, G. M.; Enachescu, M.; Ogletree, D. F.; Ribeiro, R. A.; Canfield, P. C.; Jenks, C. J.; Thiel, P. A.; Saenz, J. J.; Salmeron, M. Sensing dipole fields at atomic steps with combined scanning tunneling and force microscopy. *Phys. Rev. Lett.* **2005**, *95* (13)

57. Hwang, J.; Wan, A.; Kahn, A. Energetics of metal-organic interfaces: New experiments and assessment of the field. *Mater. Sci. Eng. Rep.* **2009**, *64* (1-2), 1-31

58. Nishidate, K.; Hasegawa, M. Deformation and transfer doping of a single-walled carbon nanotube adsorbed on metallic substrates. *Phys. Rev. B* **2010**, *81* (12)

59. Khomyakov, P. A.; Giovannetti, G.; Rusu, P. C.; Brocks, G.; van den Brink, J.; Kelly, P. J. First-principles study of the interaction and charge transfer between graphene and metals. *Phys. Rev. B* **2009**, *79* (19)

60. Neophytou, N.; Kienle, D.; Polizzi, E.; Anantram, M. P. Influence of defects on nanotube transistor performance. *Appl. Phys. Lett.* **2006**, *88* (24)

61. Repp, J.; Liljeroth, P.; Meyer, G. Coherent electron-nuclear coupling in oligothiophene molecular wires. *Nat. Phys.* **2010**, *6* (12), 975-979

62. Inouye, C. S.; Pong, W. Ultraviolet Electron Spectra of Rubidium Halides. *Phys. Rev. B* **1977**, *15* (4), 2265-2272

63. Aspitarte, L.; McCulley, D. R.; Bertoni, A.; Island, J. O.; Ostermann, M.; Rontani, M.; Steele, G. A.; Minot, E. D. Giant modulation of the electronic band gap of carbon nanotubes by dielectric screening. *Sci. Rep.* **2017**, *7* (1), 8828

64. Lin, H.; Lagoute, J.; Repain, V.; Chacon, C.; Girard, Y.; Lauret, J. S.; Ducastelle, F.; Loiseau, A.; Rousset, S. Many-body effects in electronic bandgaps of carbon nanotubes measured by scanning tunnelling spectroscopy. *Nat. Mater.* **2010**, *9* (3), 235-238

65. Brothers, E. N.; Izmaylov, A. F.; Scuseria, G. E.; Kudin, K. N. Analytically Calculated Polarizability of Carbon Nanotubes: Single Wall, Coaxial, and Bundled Systems. *J. Phys. Chem. C* **2008**, *112* (5), 1396-1400

66. Saito, R.; Fujita, M.; Dresselhaus, G.; Dresselhaus, M. S. Electronic-structure of chiral graphene tubules. *Appl. Phys. Lett.* **1992**, *60* (18), 2204-2206

67. Matsuo, Y.; Tahara, K.; Nakamura, E. Theoretical studies on structures and aromaticity of finite-length armchair carbon nanotubes. *Org. Lett.* **2003**, *5* (18), 3181-3184

68. Zhou, Z. Y.; Steigerwald, M.; Hybertsen, M.; Brus, L.; Friesner, R. A. Electronic structure of tubular aromatic molecules derived from the metallic (5,5) armchair single wall carbon nanotube. *J. Am. Chem. Soc.* **2004**, *126* (11), 3597-3607

69. Adamska, L.; Nazin, G. V.; Doorn, S. K.; Tretiak, S. Self-Trapping of Charge Carriers in Semiconducting Carbon Nanotubes: Structural Analysis. *J. Phys. Chem. Lett.* **2015**, *6* (19), 3873-3879

70. Petrushenko, I. K.; Ivanov, N. A. Ionization potentials and structural properties of finite-length single-walled carbon nanotubes: DFT study. *Phys. E* **2013**, *54*, 262-266

71. Matsuda, Y.; Tahir-Kheli, J.; Goddard, W. A. Definitive Band Gaps for Single-Wall Carbon Nanotubes. *J. Phys. Chem. Lett.* **2010**, *1* (19), 2946-2950

72. Champagne, B.; Perpete, E. A.; van Gisbergen, S. J. A.; Baerends, E. J.; Snijders, J. G.; Soubra-Ghaoui, C.; Robins, K. A.; Kirtman, B. Assessment of conventional density functional

schemes for computing the polarizabilities and hyperpolarizabilities of conjugated oligomers: An ab initio investigation of polyacetylene chains. *J. Chem. Phys.* **1998**, *109* (23), 10489-10498

73. Segawa, Y.; Omachi, H.; Itami, K. Theoretical Studies on the Structures and Strain Energies of Cycloparaphenylenes. *Org. Lett.* **2010**, *12* (10), 2262-2265

74. Tasis, D.; Tagmatarchis, N.; Bianco, A.; Prato, M. Chemistry of carbon nanotubes. *Chem. Rev.* **2006**, *106* (3), 1105-1136

75. Heyd, J.; Scuseria, G. E.; Ernzerhof, M. Hybrid functionals based on a screened Coulomb potential. *J. Chem. Phys.* **2003**, *118* (18), 8207-8215

76. Autschbach, J.; Srebro, M. Delocalization Error and "Functional Tuning" in Kohn-Sham Calculations of Molecular Properties. *Acc. Chem. Res.* **2014**, *47* (8), 2592-2602

77. Kupka, T.; Stachow, M.; Chelmecka, E.; Pasterny, K.; Stobinska, M.; Stobinski, L.; Kaminsky, J. Efficient Modeling of NMR Parameters in Carbon Nanosystems. *J. Chem. Theor. Comput.* **2013**, *9* (9), 4275-4286

78. Jensen, L.; Schmidt, O. H.; Mikkelsen, K. V.; Astrand, P. O. Static and frequency-dependent polarizability tensors for carbon nanotubes. *J. Phys. Chem. B* **2000**, *104* (45), 10462-10466

79. Peralta-Inga, Z.; Lane, P.; Murray, J. S.; Body, S.; Grice, M. E.; O'Connor, C. J.; Politzer, P. Characterization of surface electrostatic potentials of some (5,5) and (n,1) carbon and boron/nitrogen model nanotubes. *Nano Lett.* **2003**, *3* (1), 21-28

80. Wei, X. J.; Tanaka, T.; Yomogida, Y.; Sato, N.; Saito, R.; Kataura, H. Experimental determination of excitonic band structures of single-walled carbon nanotubes using circular dichroism spectra. *Nat. Comm.* **2016**, *7*

81. Pekker, Á.; Kamarás, K. Wide-range optical studies on various single-walled carbon nanotubes: Origin of the low-energy gap. *Phys. Rev. B* **2011**, *84* (7), 075475

82. Metzger, R. M. *The Physical Chemist's Toolbox*; Wiley, 2012.

83. Furlan, S.; Giannozzi, P. The interactions of nitrogen dioxide with graphene-stabilized Rh clusters: a DFT study. *Phys. Chem. Chem. Phys.* **2013**, *15* (38), 15896-15904

84. Laird, E. A.; Kuemmeth, F.; Steele, G. A.; Grove-Rasmussen, K.; Nygard, J.; Flensberg, K.; Kouwenhoven, L. P. Quantum transport in carbon nanotubes. *Rev. Mod. Phys.* **2015**, *87* (3), 703-764

85. Zhou, X.; Park, J.-Y.; Huang, S.; Liu, J.; McEuen, P. L. Band Structure, Phonon Scattering, and the Performance Limit of Single-Walled Carbon Nanotube Transistors. *Phys. Rev. Lett.* **2005**, *95* (14), 146805.

REFERENCES CITED FOR CHAPTER VII

1. Franklin, A. D. Nanomaterials in transistors: From high-performance to thin-film applications. *Sci.* **2015,** *349* (6249), aab2750.

2. Li, Y. Carbon Nanotube Research in Its 30th Year. *ACS Nano* **2021,** *15* (6), 9197-9200.

3. De Volder, M. F. L.; Tawfick, S. H.; Baughman, R. H.; Hart, A. J. Carbon nanotubes: Present and future commercial applications. *Sci.* **2013,** *339* (6119), 535-539.

4. Penzo, E.; Palma, M.; Chenet, D. A.; Ao, G.; Zheng, M.; Hone, J. C.; Wind, S. J. Directed Assembly of Single Wall Carbon Nanotube Field Effect Transistors. *ACS Nano* **2016,** *10* (2), 2975-2981.

5. Qiu, C.; Zhang, Z.; Zhong, D.; Si, J.; Yang, Y.; Peng, L. M. Carbon nanotube feedback-gate field-effect transistor: Suppressing current leakage and increasing on/off ratio. *ACS Nano* **2015,** *9* (1), 969-977.

6. Cao, C.; Andrews, J. B.; Kumar, A.; Franklin, A. D. Improving Contact Interfaces in Fully Printed Carbon Nanotube Thin-Film Transistors. *ACS Nano* **2016,** *10* (5), 5221-5229.

7. Lee, D.; Lee, B. H.; Yoon, J.; Ahn, D. C.; Park, J. Y.; Hur, J.; Kim, M. S.; Jeon, S. B.; Kang, M. H.; Kim, K.; Lim, M.; Choi, S. J.; Choi, Y. K. Three-Dimensional Fin-Structured Semiconducting Carbon Nanotube Network Transistor. *ACS Nano* **2016,** *10* (12), 10894-10900.

8. Tersoff, J. Low-frequency noise in nanoscale ballistic transistors. *Nano Lett.* **2007,** *7* (1), 194-198.

9. Wang, N. P.; Heinze, S.; Tersoff, J. Random-telegraph-signal noise and device variability in ballistic nanotube transistors. *Nano Lett.* **2007,** *7* (4), 910-913.

10. Kalinin, S. V.; Bonnell, D. A.; Freitag, M.; Johnson, A. T. Tip-gating effect in scanning impedance microscopy of nanoelectronic devices. *App. Phys. Lett.* **2002,** *81* (27), 5219-5221.

11. Bockrath, M.; Liang, W.; Bozovic, D.; Hafner, J. H.; Lieber, C. M.; Tinkham, M.; Park, H. Resonant electron scattering by defects in single-walled carbon nanotubes. *Sci.* **2001,** *291* (5502), 283-285.

12. Hunt, S. R.; Wan, D.; Khalap, V. R.; Corso, B. L.; Collins, P. G. Scanning gate spectroscopy and its application to carbon nanotube defects. *Nano Lett.* **2011,** *11* (3), 1055-1060.

13. Freitag, M.; Johnson, A. T.; Kalinin, S. V.; Bonnell, D. A. Role of Single Defects in Electronic Transport through Carbon Nanotube Field-Effect Transistors. *Phys. Rev. Lett.* **2002,** *89* (21), 216801.

14. Bian, K.; Gerber, C.; Heinrich, A. J.; Müller, D. J.; Scheuring, S.; Jiang, Y. Scanning probe microscopy. *Nat. Rev. Methods Primers* **2021,** *1* (1), 1-29.

15. Clair, S.; Shin, H. J.; Kim, Y.; Kawai, M. Electronic modulations in a single wall carbon nanotube induced by the Au(111) surface reconstruction. *App. Phys. Lett.* **2015,** *106* (5), 53111.

16. Kislitsyn, D. A.; Hackley, J. D.; Nazin, G. V. Vibrational excitation in electron transport through carbon nanotube quantum dots. *J. Phys. Chem. Lett.* **2014,** *5* (18), 3138-3143.

17. Shin, H. J.; Clair, S.; Kim, Y.; Kawai, M. Substrate-induced array of quantum dots in a single-walled carbon nanotube. *Nat. Nanotechnol.* **2009,** *4* (9), 567-570.

18. He, X.; Gifford, B. J.; Hartmann, N. F.; Ihly, R.; Ma, X.; Kilina, S. V.; Luo, Y.; Shayan, K.; Strauf, S.; Blackburn, J. L.; Tretiak, S.; Doorn, S. K.; Htoon, H. Low-Temperature Single Carbon Nanotube Spectroscopy of sp3 Quantum Defects. *ACS Nano* **2017,** *11* (11), 10785-10796.

19. Shin, H. J.; Clair, S.; Kim, Y.; Kawai, M. Electronic structure of single-walled carbon nanotubes on ultrathin insulating films. *App. Phys. Lett.* **2008,** *93* (23), 233104.

20. Taber, B. N.; McDowell, B. W.; Mills, J. M.; Gervasi, C. F.; Nazin, G. V. Impact of External Electronic Perturbations on Single-Walled Carbon Nanotube Electronic Structure: Scanning Tunneling Spectroscopy and Density Functional Theory. *J. Phys. Chem. C* **2023,** *127* (9), 4651-4659.

21. Pivetta, M.; Patthey, F.; Stengel, M.; Baldereschi, A.; Schneider, W. D. Local work function Moiré pattern on ultrathin ionic films: NaCl on Ag(100). *Phys. Rev. B - Condens. Matter Mater. Phys.* **2005,** *72* (11), 115404.

22. Hebenstreit, W.; Redinger, J.; Horozova, Z.; Schmid, M.; Podloucky, R.; Varga, P. Atomic resolution by STM on ultra-thin films of alkali halides: Experiment and local density calculations. *Surf. Sci.* **1999,** *424* (2), L321-L328.

23. Sun, X.; Felicissimo, M. P.; Rudolf, P.; Silly, F. NaCl multi-layer islands grown on Au(111)-(22 × √3) probed by scanning tunneling microscopy. *Nanotechnol.* **2008,** *19* (49), 495307.

24. Olsson, F. E.; Persson, M. A density functional study of adsorption of sodium-chloride overlayers on a stepped and a flat copper surface. *Surf. Sci.* **2003,** *540* (2-3), 172-184.

25. Olsson, F. E.; Persson, M.; Repp, J.; Meyer, G. Scanning tunneling microscopy and spectroscopy of NaCl overlayers on the stepped Cu(311) surface: Experimental and theoretical study. *Phys. Rev. B - Condens. Matter Mater. Phys.* **2005,** *71* (7), 075419.

26. Fröhlich, D.; Staginnus, B. New assignment of the band gap in the alkali bromides by two-photon spectroscopy. *Phys. Rev. Lett.* **1967,** *19* (9), 496-498.

27. Brown, F. C.; Gähwiller, C.; Fujita, H.; Kunz, A. B.; Scheifley, W.; Carrera, N. Extreme-ultraviolet spectra of ionic crystals. *Phys. Rev. B* **1970,** *2* (6), 2126-2138.

28. Mohn, F.; Gross, L.; Moll, N.; Meyer, G. Imaging the charge distribution within a single molecule. *Nat. Nanotechnol. 2012 7:4* **2012,** *7* (4), 227-231.

29. Repp, J.; Meyer, G. Scanning tunneling microscopy of adsorbates on insulating films. from the imaging of individual molecular orbitals to the manipulation of the charge state. *App. Phys. A: Mater. Sci. Process.* **2006,** *85* (4), 399-406.

30. Gross, L.; Moll, N.; Mohn, F.; Curioni, A.; Meyer, G.; Hanke, F.; Persson, M. High-resolution molecular orbital imaging using a p-wave STM tip. *Phys. Rev. Lett.* **2011,** *107* (8), 086101.

31. Scarfato, A.; Chang, S. H.; Kuck, S.; Brede, J.; Hoffmann, G.; Wiesendanger, R. Scanning tunneling microscope study of iron(II) phthalocyanine growth on metals and insulating surfaces. *Surf. Sci.* **2008,** *602* (3), 677-683.

32. Villagomez, C. J.; Zambelli, T.; Gauthier, S.; Gourdon, A.; Stojkovic, S.; Joachim, C. STM images of a large organic molecule adsorbed on a bare metal substrate or on a thin insulating layer: Visualization of HOMO and LUMO. *Surf. Sci.* **2009,** *603* (10-12), 1526-1532.

33. Heidorn, S. C.; Bertram, C.; Cabrera-Sanfelix, P.; Morgenstern, K. Consecutive mechanism in the diffusion of D2O on a NaCl(100) bilayer. *ACS Nano* **2015,** *9* (4), 3572-3578.

34. Guo, J.; Meng, X.; Chen, J.; Peng, J.; Sheng, J.; Li, X. Z.; Xu, L.; Shi, J. R.; Wang, E.; Jiang, Y. Real-space imaging of interfacial water with submolecular resolution. *Nat. Mater.* **2014,** *13* (2), 184-189.

35. Mura, M.; Silly, F.; Briggs, G. A. D.; Castell, M. R.; Kantorovich, L. N. H-bonding supramolecular assemblies of PTCDI molecules on the Au(111) surface. *J. Phys. Chem. C* **2009,** *113* (52), 21840-21848.

36. Ramoino, L.; Von Arx, M.; Schintke, S.; Baratoff, A.; Güntherodt, H. J.; Jung, T. A. Layer-selective epitaxial self-assembly of porphyrins on ultrathin insulators. *Chem. Phys. Lett.* **2006,** *417* (1-3), 22-27.

37. Liljeroth, P.; Repp, J.; Meyer, G. Current-induced hydrogen tautomerization and conductance switching of naphthalocyanine molecules. *Sci.* **2007,** *317* (5842), 1203-1206.

38. Repp, J.; Liljeroth, P.; Meyer, G. Coherent electron-nuclear coupling in oligothiophene molecular wires. *Nat. Phys.* **2010,** *6* (12), 975-979.

39. McDowell, B. W.; Mills, J. M.; Honda, M.; Nazin, G. V. Structural Bistability in RbI Monolayers on Ag(111). *J. Phys. Chem. Lett.* **2023,** *14*, 3023-3030.

40. McDowell, B. W.; Mills, J. M.; Honda, M.; George; Nazin, V.; Nazin, G. V.; Affiliations. Spatially modulated interface states in a two-dimensional potential: Single-layer RbI on Ag(111). *J. Chem. Phys.* **2023,** *159* (22), 224705.

41. Hackley, J. D.; Kislitsyn, D. A.; Beaman, D. K.; Ulrich, S.; Nazin, G. V. High-stability cryogenic scanning tunneling microscope based on a closed-cycle cryostat. *Rev. Sci. Instrum.* **2014,** *85* (10), 103704.

42. Taber, B. N.; Neill, M. L.; Thom, T. N.; Clapp, O. D.; Lee, J. In situ plasmonic tip preparation and validation techniques for scanning tunneling microscopy. *J. Vac. Sci. Technol. A* **2023,** *41* (5), 53205.

43. Albrecht, P. M.; Lyding, J. W. Ultrahigh-vacuum scanning tunneling microscopy and spectroscopy of single-walled carbon nanotubes on hydrogen-passivated Si(100) surfaces. *Appl. Phys. Lett.* **2003,** *83* (24), 5029-5031.

44. Kohn, W.; Sham, L. J. Self-consistent equations including exchange and correlation effects. *Phys. Rev.* **1965,** *140* (4A), A1133.

45. Kresse, G.; Furthmüller, J. Efficiency of ab-initio total energy calculations for metals and semiconductors using a plane-wave basis set. *Comput. Mater. Sci.* **1996,** *6* (1), 15-50.

46. Kresse, G.; Furthmüller, J. Efficient iterative schemes for ab initio total-energy calculations using a plane-wave basis set. *Phys. Rev. B - Condens. Matter Mater. Phys.* **1996,** *54* (16), 11169-11186.

47. Kresse, G.; Hafner, J. Ab initio molecular dynamics for liquid metals. *Phys. Rev. B* **1993,** *47* (1), 558-561.

48. Blöchl, P. E. Projector augmented-wave method. *Phys. Rev. B* **1994,** *50* (24), 17953-17979.

49. Tran, R.; Xu, Z.; Radhakrishnan, B.; Winston, D.; Sun, W.; Persson, K. A.; Ong, S. P. Surface energies of elemental crystals. *Sci. Data* **2016,** *3* (1), 160080.

50. Perdew, J. P.; Ruzsinszky, A.; Csonka, G. I.; Vydrov, O. A.; Scuseria, G. E.; Constantin, L. A.; Zhou, X.; Burke, K. Restoring the density-gradient expansion for exchange in solids and surfaces. *Phys. Rev. Lett.* **2008,** *100* (13), 136406.

51. Hanke, F.; Björk, J. Structure and local reactivity of the Au(111) surface reconstruction. *Phys. Rev. B* **2013,** *87*, 235422-235422.

52. Henkelman, G.; Arnaldsson, A.; Jónsson, H. A fast and robust algorithm for Bader decomposition of charge density. *Comput. Mater. Sci.* **2006,** *36* (3), 354-360.

53. Sanville, E.; Kenny, S. D.; Smith, R.; Henkelman, G. Improved grid-based algorithm for Bader charge allocation. *J. Comput. Chem.* **2007,** *28* (5), 899-908.

54. Tang, W.; Sanville, E.; Henkelman, G. A grid-based Bader analysis algorithm without lattice bias. *J. Phys. Condens. Matter* **2009,** *21* (8), 084204-084204.

55. Yu, M.; Trinkle, D. R. Accurate and efficient algorithm for Bader charge integration. *J. Chem. Phys.* **2011,** *134* (6), 64111.

56. Momma, K.; Izumi, F. VESTA 3 for three-dimensional visualization of crystal, volumetric and morphology data. *J. Appl. Crystallogr.* **2011,** *44* (6), 1272-1276.

57. Chen, C. J. *Introduction to Scanning Tunneling Microscopy: Second Edition*; Oxford University Press, **2007**58. Wildöer, J. W. G.; Venema, L. C.; Rinzler, A. G.; Smalley, R. E.; Dekker, C. Electronic structure of atomically resolved carbon nanotubes. *Nature 1998 391:6662* **1998,** *391* (6662), 59-62.

58. Wildöer, J. W. G.; Venema, L. C.; Rinzler, A. G.; Smalley, R. E.; Dekker, C. Electronic structure of atomically resolved carbon nanotubes. *Nat.* **1998,** *391* (6662), 59-62.

59. Odom, T. W.; Huang, J. L.; Kim, P.; Lieber, C. M. Atomic structure and electronic properties of single-walled carbon nanotubes. *Nat.* **1998,** *391* (6662), 62-64.

60. Venema, L.; Janssen, J.; Buitelaar, M.; Wildöer, J.; Lemay, S.; Kouwenhoven, L.; Dekker, C. Spatially resolved scanning tunneling spectroscopy on single-walled carbon nanotubes. *Phys. Rev. B* **2000,** *62* (8), 5238.

61. Bachilo, S. M.; Strano, M. S.; Kittrell, C.; Hauge, R. H.; Smalley, R. E.; Weisman, R. B. Structure-assigned optical spectra of single-walled carbon nanotubes. *Sci.* **2002,** *298* (5602), 2361-2366.

62. Yeo, H.; Seong Lee, J.; Ejaz Khan, M.; al; Wang, X.-X.; Wang, K.; Peng, Y.-G.; Niranjan, M. K. Theoretical investigation of electronic bandgaps of semiconducting single-walled carbon nanotubes using semi-empirical self-consistent tight binding and ab-inito density functional methods. *J. Phys. Comm.* **2020,** *4* (1), 015004.

63. Nazin, G. V.; Wu, S. W.; Ho, W. Tunneling rates in electron transport through double-barrier molecular junctions in a scanning tunneling microscope. *Proc. National Acad. Sci.* **2005,** *102* (25), 8832-8837.

64. Ploigt, H. C.; Brun, C.; Pivetta, M.; Patthey, F.; Schneider, W. D. Local work function changes determined by field emission resonances: NaCl/Ag (100). *Phys. Rev. B - Condens. Matter Mater. Phys.* **2007,** *76* (19), 195404.

65. Tan, X.; Pan, J.; Feng, J.; Zhang, Z.; Liu, M.; Ma, D.; Qiu, X. One-Dimensional Periodic Buckling at a Symmetry-Incompatible Heterointerface of the NaCl(001) Monolayer on Ir(111). *J. Phys. Chem. C* **2023,** *127* (12), 6109-6114.

REFERENCES CITED FOR APPENDIX A

1. Ploigt, H. C.; Brun, C.; Pivetta, M.; Patthey, F.; Schneider, W. D. Local work function changes determined by field emission resonances: NaCl/Ag (100). *Phys. Rev. B: Condens. Matter Mater. Phys.* **2007,** *76* (19), 195404-195404.

2. Pivetta, M.; Patthey, F.; Stengel, M.; Baldereschi, A.; Schneider, W. D. Local work function Moiré pattern on ultrathin ionic films: NaCl on Ag(100). *Phys. Rev. B: Condens. Matter Mater. Phys.* **2005,** *72* (11), 115404-115404.

3. Olsson, F. E.; Persson, M. A density functional study of adsorption of sodium-chloride overlayers on a stepped and a flat copper surface. *Surf. Sci.* **2003,** *540* (2-3), 172-184.

4. Olsson, F. E.; Persson, M.; Repp, J.; Meyer, G. Scanning tunneling microscopy and spectroscopy of NaCl overlayers on the stepped Cu(311) surface: Experimental and theoretical study. *Phys. Rev. B: Condens. Matter Mater. Phys.* **2005,** *71* (7), 075419-075419.

5. Landau, L. D.; Lifshi͡ts, E. M.; Pitaevskiĭ, L. P.; Sykes, J. B.; Bell, J. S. *Quantum mechanics : non-relativistic theory*, 3rd ed. Pergamon Press. **1977**, p 1-673.

6. Chen, C. J. *Introduction to Scanning Tunneling Microscopy, 2nd ed*. Oxford University Press, **2007**, p 1-432.

REFERENCES CITED FOR APPENDIX B

1. Ploigt, H. C.; Brun, C.; Pivetta, M.; Patthey, F.; Schneider, W. D. Local work function changes determined by field emission resonances: NaCl/Ag (100). *Phys. Rev. B* **2007,** *76* (19), 195404-195404.

REFERENCES CITED FOR APPENDIX C

1. McDowell, B. W.; Mills, J. M.; Honda, M.; Nazin, G. V. Structural Bistability in RbI Monolayers on Ag(111). *J. Phys. Chem. Lett.* **2023,** *14*, 3023-3030.

2. Heidorn, S.; Bertram, C.; Koch, J.; Boom, K.; Matthaei, F.; Safiei, A.; Henzl, J.; Morgenstern, K. Influence of substrate surface-induced defects on the interface state between NaCl(100) and Ag(111). *J. Phys. Chem. C* **2013,** *117* (31), 16095-16103.

3. Kolpatzeck, K.; Brendel, L.; Möller, R.; Robles, R.; Lorente, N. Paradoxical effects for a one-dimensional periodic potential embedded in a two-dimensional system. *Phys. Rev. B* **2023,** *107* (15), 155418-155418.

4. Repp, J.; Meyer, G.; Paavilainen, S.; Olsson, F. E.; Persson, M. Scanning tunneling spectroscopy of Cl vacancies in NaCl films: Strong electron-phonon coupling in double-barrier tunneling junctions. *Phys. Rev. Lett.* **2005,** *95* (22), 225503-225503.

5. Abramowitz, M.; Stegun, I. A. *Handbook of Mathematical Functions with Formulas, Graphs, and Mathematical Tables, 9th printing*. Dover: New York, 1972; p 722-722.

6. Zwillinger, D. *Handbook of Differential Equations*. 3rd ed.; Acadamic Press: Boston, 1997; p 125

REFERENCES CITED FOR APPENDIX E

1. Lee, S.; Kim, G.; Kim, H.; Choi, B. Y.; Lee, J.; Jeong, B. W.; Ihm, J.; Kuk, Y.; Kahng, S. J. Paired gap states in a semiconducting carbon nanotube: Deep and shallow levels. *Phys. Rev. Lett.* **2005**, *95* (16), 166402.

2. Berthe, M.; Yoshida, S.; Ebine, Y.; Kanazawa, K.; Okada, A.; Taninaka, A.; Takeuchi, O.; Fukui, N.; Shinohara, H.; Suzuki, S.; et al. Reversible Defect Engineering of Single-Walled Carbon Nanotubes Using Scanning Tunneling Microscopy. *Nano Lett.* **2007**, *7* (12), 3623-3627.

3. Yamada, K.; Sato, H.; Komaguchi, T.; Mera, Y.; Maeda, K. Local opening of a large bandgap in metallic single-walled carbon nanotubes induced by tunnel injection of low-energy electrons. *Appl. Phys. Lett.* **2009**, *94* (25), 253103.

4. Krasheninnikov, A. V. Predicted scanning tunneling microscopy images of carbon nanotubes with atomic vacancies. *Solid State Commun.* **2001**, *118* (7), 361-365.

5. Hanke, F.; Björk, J. Structure and local reactivity of the Au(111) surface reconstruction. *Phys. Rev. B* **2013**, *87*, 235422-235422.